

SUBSURFACE INFORMATION DEDUCED FROM REMOTE SENSING AND RESISTIVITY DATA

*A Thesis submitted
In partial Fulfillment of the Requirements
For the Degree of*
MASTER OF TECHNOLOGY

By
RAED ALI AHMAD



to the
**DEPARTMENT OF CIVIL ENGINEERING
INDIAN INSTITUTE OF TECHNOLOGY, KANPUR
NOVEMBER, 1999**

2 MAR 2000/CE

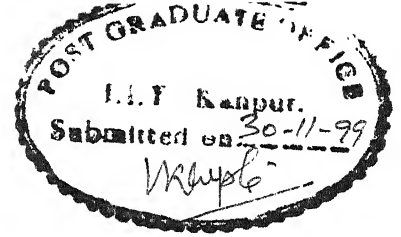
CENTRAL LIBRARY
I. I. T., KANPUR

A 130464

2512



A130464



CERTIFICATE

It is certified that the work contained in this thesis entitled
**“SUBSURFACE INFORMATION DEDUCED FROM
REMOTE SENSING AND RESISTIVITY DATA”** by **RAED
ALI AHMAD** has been carried out under my supervision and that this
work has not been submitted elsewhere for a degree.

RP Singh
29/11/99

Ramesh P. Singh

Professor

Department of Civil Engineering

Indian Institute Of Technology

Kanpur – 208016, INDIA

ACKNOWLEDGEMENTS

The author is deeply indebted, first and foremost, to the thesis supervisor Dr. Ramesh P. Singh for providing his research lab facilities, valuable guidance, cooperation and meticulous scientific attitude.

I am thankful to all my teachers especially to Drs. B. C. Raymahashay and Rajiv Sinha.

My special thanks to my family friends, Ashraf, Kamal, and Jamal, and all my friends in Civil Engineering department including Mishra, Sushmita, Sudipa, Dash, Pavan and Sudipta for their moral support and assistance during my stay on the campus.

I would like to express my sincere regards to my family members for their moral support and care, especially to my dear mother and brothers.

Thanks are also to the Indian Council for Cultural Relationship (ICCR), New Delhi for awarding me scholarship and for financial support to purchase remote sensing data and field expenses.

I.I.T, Kanpur, India
November, 1999

RAED ALI AHMAD

ABSTRACT

The use of remote sensing data for surface mapping is very common and is being carried out on routine basis. The IRS-IC LISS-III false colour composite image of Kanpur area shows a large channel migration pattern through neck cut off along Ganga river. This cut off spreads over an area of about 150 km² showing that the Ganga river has migrated 15 km in the east from the present position during past several years. In order to understand the migration pattern, detailed image processing of data have been carried out to delineate the fractures and faults in the cut off area. Efforts have been made to use different edge operators: Sobel, Laplacian, and High pass filters (HPF). It has been found that only Sobel and High pass filters give good results. Otsu thresholding technique has been applied before and after merging, and binary images have been generated, which contain two pixel value '0' and '255', higher pixels value '255' represent an edge. The thresholding technique has provided the ability for knowing the fault location. To improve the spatial resolution as well as to improve the visual interpretation, and to see the effect of merging on thresholding technique, various merging methods: HPF, IHS (Hue Intensity Saturation), P+Xs, and Price algorithm have been applied. The HPF method found to give better results due to different time for PAN and multi-spectral data. The HPF and Price methods have been used successfully to remove cloud cover on high resolution images. The normalized difference vegetation index (NDVI) image of the area has been generated which shows significant difference across the expected fault. The analysis of soil across and quality of water samples in the area further support the presence of subsurface fault in the area. We have carried out 14 resistivity soundings in the area; the sounding results show drastic change across a profile crossing the large cut off. The integration of remote sensing data, surface and subsurface information deduced from resistivity soundings has been discussed in the Ganga river migration near Kanpur.

CONTENTS

Page No.

LIST OF FIGURES

LIST OF TABLES

LIST of PLATES

CHAPTER-I INTRODUCTION

1.1 General	1
1.2 Objectives of the present thesis	2
1.3 Overview of study site data resource	3
1.4 Software details	4
1.5 Organization of the thesis	4

CHAPTER-II GEOLOGICAL AND GEOPHYSICAL INFORMATION ABOUT THE STUDY AREA

2.1 General	5
2.2 Geology of Ganga plain	5
2.2.1 General information of Ganga Basin	5
2.2.2 Geology and lithology of Ganga plain	6
2.2.3 Geomorphology of the area	9
2.2.3.1 Rocky Surface	10
2.2.3.2 Upland Plain	10
2.2.3.3 Flood Plain	12
2.2.4 General Information about study area (Kanpur-Unnao)	13
2.2.4.1 Introduction	13
2.2.4.2 Subsurface Stratigraphy of Kanpur Area	14
2.2.5 Tectonic frame work of Ganga basin	17
2.3 Geophysical information about the study area	20
2.3.1 Gravity Results	20
2.3.2 Seismic Studies	22
2.3.3 Aeromagnetic survey in the Ganga basin	24

CHAPTER-III DETAIED OF IMAGE PROCESSING AND RESISTIVITY METHOD

3.1 General	26
3.2 Data merging	26
3.2.1 Review of previous research	26
3.2.2 Data merging methods	29
3.2.2.1 Intensity- Hue-Saturation (IHS) method	29
3.2.2.1.2 Steps applied	30
3.2.2.2 High Pass Filter (HPF)	33
3.2.2.2.1 Steps applied	33
3.2.2.3 P+XS Method	35
3.2.2.4 Price algorithm	35
3.2.2.4.1 Steps applied	35
3.3 Edge extraction	38
3.3.1 Introduction	39
3.3.2 Edge detection	39
3.3.2.1 Sobel Operator	40
3.3.2.2 Laplacian Operators	41
3.3.2.3 High pass filter	42
3.3.3 Thresholding	43
3.3.3.1 Otsu Thresholding Technique	43
3.4 Resistivity method	46
3.4.1 General	46
3.4.2 Electrical resistivity method	47
3.4.3 Field Procedure	49
3.4.4 Resistivity Profiling	50
3.4.5 Interpretation	51

CHAPTER-IV RESULTS AND DISCUSSION

4.1 General	54
4.2 Methodology	54
4.2.1 Image processing	54
4.2.2 Resistivity analysis	54
4.3 Digital image processing	57
4.3.1 False Colour Composite (FCC)	57
4.3.2 Geomorphological studies	57
4.3.3 NDVI Normalized Vegetation Index	59
4.3.4 Edge detection	61
4.3.5 Merging Technique	62
4.3.5.1 Results from data merging	70
4.3.6 Results from remote sensing data	72
4.4 Geophysical Data Analysis	80
4.4.1 Resistivity method	80
4.4.1.1 Field work	81
4.4.1.2 Results and discussion	82
4.5 Integration of remote sensing and resistivity data	92

CHAPTER-V CONCLUSION

5.1 General	93
5.2 Results	93
5.3 Future work	94

REFERENCES	95
-------------------	-----------

APPENDIX I

APPENDIX II

APPENDIX III

LIST OF FIGURES

Number	Title	Page No.
2.1	Geomorphological map of Ganga Plain. U.P. province (Khan, 1996).	9
2.2	Subsurface stratigraphy of Alluvium in southern margin of Gangetic Plain (Redrawn after Bajpai, 1989)	14
2.3	Schematic diagram showing evolution of southern margin of Gangetic alluvium (after Bajpai and Singh, 1989)	16
2.4	Sketch Quaternary geological map of Ganga basin showing locations of cross faults in the basement (after Khan, and Kumar, 1996)	18
2.5	Geological cross section along profile X-Y based on borehole data (after Khan, and Kumar, 1996)	19
2.6	Schematic diagram showing successive neotectonic block movement during different periods (after Khan and Kumar, 1996)	19
2.7	Bouguer anomaly map over Ganga basin (after Verrma, 1991)	20
2.8	Profile L ₁ L ₂ L ₃ L ₄ nearly parallel to axis of Ganga basin, showing the major structures and nature of Bouguer anomaly (after Verma, 1991)	22
2.9	Cross section based on seismic and geological data (after Verma,1991)	23
2.10	Tectonics map of India (Eremenko and Negi, 1968)	24
3.1	Double cone model of the IHS color space	31
3.2	Wenner configuration	48
3.4	Schlumberger configuration	48
3.5	Resistivity array	49
3.6	Shows the master curves for interpretation (after Reddy, 1995)	51
3.7	Shows the interpretation procedure (after Reddy, 1995)	53
4.1	Shows the methodology followed in the present study	56
4.2	FCC false colour composite for study area	57

4.3	Stretching FCC.	58
4.4	Geomorphological map produced from a stretching FCC	59
4.5	NDVI produced using Band 3 and Band 4	60
4.6	Classified image based on NDVI values	60
4.7	Subsurface information from remote sensing data	73
4.8	A representative guide to resistivity of various Sediment rocks (after Todd, 1980)	80
4.9	Location of resistivity soundings on FCC image	81
4.10	Resistivity set up in the field	82
4.11	Profile I (S-N): Apparent resistivity variations along Dostinagar, Garha, Kirna, Firouzpur	84
4.12	Profile II Apparent resistivity variations along Dullakhera, Parmani, Diwankhera, Isunyian	84
4.13	Profile III (S-N): Apparent resistivity variations along Utaria, Mahipatikhera, Powa	84
4.14	Profile IV (S-N): Apparent resistivity along Pyarepure, Bhadeona, Mubarkpur	85
4.15	3-dimension Apparent resistivity variations along profile V Firuzpur, Isunyian, Mahaptikhera.	85
4.16	Apparent Resistivity contours in the study area	85
4.17	App. Resi. variations and Layered model estimated at Dostinagar	87
4.18	App. Resi. variations and Layered model estimated at Garah.	87
4.19	App. Resi. variations and Layered model estimated at Dullakhera	87
4.20	App. Resi. variations and Layered model estimated at Payrepur	88
4.21	App. Resi. variations and Layered model estimated at Utaria	88
4.22	App. Res. variations and Layered model estimated at Parmani	88
4.23	App. Resi. variations and Layered model estimated at Powa	89
4.24	App. Resi. variations and Layered model estimated at Kirna	89
4.25	App. Resi. variations and Layered model estimated at Diwankhera	89
4.26	App. Resi. variations and layered model estimated at Bhadeona	90
4.27	App. Resi. variations and layered model estimated at Mubarkpur	90

4.28	App. Resi. variations and Layered model estimated at Muhaptikhera	90
4.29	App. Resi. variations and Layered model estimated at Isunyian	91
4.30	App. Resi. variations and Layered model estimated at Firuzpur	91

LIST OF TABLES

Number	Title	Page No.
1.1	Satellite data products used for the present study (IRS-1C user manual, 1995)	3
2.1	Classification of Quarternary deposits of Gangetic b	
2.2	asin (after Kumar 1996).	8
2.2	Geomorphic succession of Ganga plain, Uttar Pradesh (after Pandey, 1996)	10
2.3	Available seismic information for different formations from available sources (Verma, 1991)	24
4.1	NDVI values for different classes	59
4.2	Otsu threshold values for IR1C- Band 1 and Band 2 using 16 image parts	62
4.3	Correlation coefficients between PAN and Low Resolution images	70
4.4	Average RMS errors of GCP	70
4.5	Mean and Standard deviation values of original and merged IRS-1C data	71
4.6	Number of zero pixel values of merged IRS-1C data	71

LIST OF PLATES

Plate No.	Title	Page No.
4.1	Laplacian edge operator applied on Bands 2 and 3.	63
4.2	Sobel edge operator applied on Bands 2 and 3.	64
4.3	High pass filter and Otsu thresholding applied on Band 2.	65
4.4	Otsu thresholding technique applied on Band 2 and 3 before merging.	66
4.5	Otsu thresholding applied on Bands 2 and 3 after merging Using HPF merging method.	67
4.6	Otsu thresholding applied on Bands 2 and 3 after merging Using Price merging method.	68
4.7	Bands 1 and 2 after merging using HIS merging technique	
4.8	Band 3 and Band 1 after merging using HIS and P+XS methods respectively	75
4.9	Band 2 after merging using P+XS method	76
4.10	Bands 1 and 2 after merging using HPF merging method.	77
4.11	Band 3 and Band 1 after merging using HPF and Price methods respectively	78
4.12	Bands 2 and 3 after merging using Price merging method	79

Chapter I

INTRODUCTION

1.1 GENERAL

Remote sensing has proved as an important tool to provide basic information for the evaluation of natural resources. Remote sensing technology has played a major role in mapping of the Earth's resources using high-resolution data. Presently, digital analysis of remote sensing data has become less expensive and more effective in mapping resources for various purposes. Conventional geological and geophysical surveys require much time and huge expenditure for mapping of inaccessible mountainous regions. Missing of rock outcrops and limited view of geological features, as well as manual methods of data collection and processing are major difficulties in the geological information system (GIS). Using remote sensing data a continuous record of information about ground features is obtained. High resolution data and synoptic nature of the information are useful in the interpretation of geological data. However, the degree of geological information processed from remote sensing data remains far behind that processed through geological and geophysical surveys. This is due to the limitation of present sensors in identifying rock formation and surface features. However, efforts are going on to improve methodologies for the interpretation of remote sensing data. Ground geological and geophysical surveys only confirm the geological features. The integration of geological, geophysical and remote sensing system will help to interpret the geological information. Various geological themes for which, both airborne as well as satellite borne data have been used to map the lineaments, lithological, structural, and geomorphological, mineral resources, and ground water targeting, engineering geological applications, river basin studies, plate tectonics and earthquakes studies, and environmental assessment.

Remote sensing data has been used widely for different purposes in the applications of sciences and engineering. Image processing involves the manipulation and interpretation of digital images with the aid of a computer. It has huge numbers of applications, such as, image transmission and storage for business applications, medical processing, radar, industrial applications, sonar and acoustic image processing. Images acquired by different kinds of satellites with different bands are useful in tracking of earth

resources; geological mapping, such as lithological mapping, earthquake and volcanic monitoring; agricultural crops, urban growth, and weather; flood and fire control; and many other environmental applications.

Recently, there has been a remarkable increase in the number of available satellite and airborne sensors. Each sensor has its mission and applications. For many applications the combined information from multiple sensors provides more comprehensive information by collecting a wide diversity of sensed wavelengths, spatial resolutions, and look angles. This led to develop a new technique called image merging.

The merging of multi-sensor and multi-resolution data is becoming a widely used procedure because of the complementary nature (different spatial and spectral resolution) of the various data sets. After image merging, we have high spectral resolution data set with high spatial resolution. Several merging techniques have been developed in the past to merge multi-sensor and multi-resolution data. Ideally, the method for merging data sets with high spatial and spectral resolution should not distort the spectral characteristics of the high spectral resolution data. Distorting the spectral characteristics of the data is not good for calibration purposes between original merged images. The main aim of data merging is to improve the information content of the images for visual interpretation and also improve the spatial resolution.

1.2 OBJECTIVES OF THE PRESENT THESIS:

- i) To study the effect of thresholding technique on edge extraction.
- ii) To map the surface features using remote sensing data.
- iii) To map the surface and subsurface structure using remote sensing data.
- iv) To study the resistivity variations in the area.
- v) To find a remarkable explanation for the migration pattern of Ganga river in Bithoor area.

The broad objective of the present research is to know the subsurface structure by using remote sensing data, and to find the effect of merging and thresholding techniques on edge extraction. Finally, to integrate remote sensing data with the resistivity variations obtained from conventional resistivity method for the same area.

1.3 OVERVIEW OF STUDY AREA AND DATA RESOURCES

The work presented in the present thesis has been conducted in agricultural area of Bithoor-Unnao Kanpur, Uttar Pradesh. The study area of Bithoor is located between North latitudes $26^{\circ} 30' 30''$ - $26^{\circ} 45' 30''$ and East longitudes $80^{\circ} 15' 30''$ - $80^{\circ} 30' 30''$. The Kanpur region has a flat topography with large part of agricultural area. Ganga river shows migration pattern through cut-off, which has paramount importance in understanding the tectonics, and subsurface dynamics, and migration pattern of Ganga river. The prominent meander cut-off spread over an area of about 150 km^2 along the Ganga river in the Kanpur region. The subsurface morphology of the basin and tectonics must have played an important role in the sedimentation pattern of the region.

Details of the satellite data products used in the present study are given in the Table '1.1. These data have been acquired from National Remote Sensing Agency (NRSA), Hyderabad. For reference, map products have also been used. Topographic maps have been obtained from Survey of India (SOI). Various images and maps used for the study are listed below:

1. Topographic map no. 63 B/ 6 on a scale 1: 50,000 to know various details of the area.
2. IRS-1C LISS-III multi-spectral satellite data acquired on February 26th, 1997.
3. IRS-1C LISS-III panchromatic satellite data acquired on December 16th, 1996.
4. OYO Resistivity meter for carrying resistivity fieldwork.
5. GPS has been used in the field to determined longitudinal and latitudinal coordinates.

Table 1.1 Satellite data products used for the present study

(from IRS-1C user manual, 1995)

Satellite	Band	Resolution (m)	Size (pixels)	Wavelength (μm)	Spectral region	Path-Row
IRS-1C LISS-III	Band 1	23.75	1057x987	0.52-0.59	Green	99 - 53
	Band 2	23.75	1057x987	0.62-0.68	Red	
	Band 3	23.75	1057x987	0.77-0.86	Near infrared	
	PAN	5.8	4228x3968	0.50-0.75		

1.4 SOFTWARE DETAILS

Programming in C language has been developed for different merging methods and for thresholding techniques and for different edge operators to extract edges from images. Standard package “IDRISI for windows” which is an integrated package for image processing and GIS have also been used. This package was used for the registration of images, and for on screen digitization of the reference map. Resixp package is used for the interpretation of resistivity data, which was collected through fieldwork.

1.5 ORGANIZATION OF THE THESIS

The thesis has been organized in five chapters. The present chapter provides a brief discussion on need of remote sensing data (data merging and thresholding technique) and geophysical data for determining the subsurface information, followed by details of study area and data resources. Chapter II deals with the geological and geophysical information of the study area. Chapter III summarizes the earlier research work and theory of image processing and electrical resistivity method. This Chapter also presents in detail the theoretical background of data merging and edge extraction with the emphasis to various techniques implemented in the present thesis. Chapter IV presents various experiments and results and shows the correlation of both remote sensing and geophysical data. Finally, Chapter V presents conclusions of the present study.

Chapter II

Geological and Geophysical Information About the Study Area

2.1 GENERAL

Extensive geological and geophysical surveys have been carried out in Ganga basin since the last century. The Oil and Natural Gas Commission particularly intensified the investigations during the last three decades for hydrocarbon exploration. These surveys have brought out a clear picture of the tectonic framework. Oldham (1883) and Meddlemiss (1890) conducted the systematic geological surveys in the Himalayan foothills in the last century. Wadia (1928), Auden (1934), and several other geologists of the Geological Survey of India have mapped the Tertiary sediments of foothills region. With the formation of Oil and Natural Gas Commission in 1956, efforts were intensified to carry out detailed geological mapping of the entire Tertiary belt. The important compilations have been made by Sahni and Mathur (1964), Karunakaram and Rao (1976), Rao (1974), Raiverman et al. (1976) highlighting the contribution of the ONGC. This area has also been covered by geophysical surveys (Das et al. 1976), Balakrishnan and Chaudhury, (1976). The structure and stratigraphy of the alluvium covered Indo-Gangatic plain were subjects of speculation for a long period by many authors like Suess (1904), Burrard (1915), Oldham (1917), Wadia (1975), and Krishnan (1964). During the last three decades the geophysical surveys were carried out by the ONGC have brought out a clear picture of basement configuration of the area. Agroes (1957) has carried out aeromagnetic surveys over the Ganga valley. Systematic geophysical surveys have been carried out by ONGC (Chudhury, 1975, Ramachandra Rao, 1973, Balakrishnan and Chudhury, 1976, Aditya et al., 1976). This chapter briefly discusses the geological and geophysical background of the Ganga basin.

2.2 GEOLOGY OF THE GANGA PLAIN

2.2.1 General Information of Ganga Basin

Ganga plain of Uttar Pradesh, forming a part of the largest alluvial plain in the world, the Indus-Ganga-Brahmaputra plain, lies between the Peninsular Shield in the

south and Himalaya in the north. It covers an area of about 2.23 lakh sq. Km. in U.P. Many theories have been put forward regarding the origin of this vast depression often referred to as "Indo-Gangetic Trough". (Suess, 1893, Burrard, 1915, 1932, Oldham, 1917, 1923, Wadia, 1938, 1966). However, it is now widely accepted that the Foreland basin (Le Fort, 1975) comprising Ganga plain, was formed due to continent-continent collision of Indian plate with Asian plate resulting in underthrusting of the Indian plate, a phenomenon still in progress. The Ganga plain in U.P. lies between Yamuna in the west and 60 m topographic contour in the east. In the north, the Himalaya demarcates it. The Peninsular Shield marks the southern boundary. It comprises Upper Ganga plain, Bundelkhand and Vindhya-Baghelkhand regions (Singh, 1971). It is the oldest Quaternary platform formed by the paleo-drainage system; relicts and trails are still seen over it as left over features. The drainage network of the area comprises three major snow fed Himalayan rivers namely Ganga, Yamuna and Ghaghara. The Ganga river being the principal trunk channel, is the recipient of all water lines in the region. The most conspicuous feature of the drainage configuration is the regional parallelism between courses of the rivers. This seemingly featureless plain lacks topographic prominence and the river bluffs, levees, and dead arms of the river channels and the river channel break the monotony of the physical landscape. The Trans-Yamuna area exhibits a distinct topography represented by deep valleys separated by sharp spurs and buttresses due to ravine landscape topography along rivers and streams. This feature is not very uncommon with other streams of the rest of the area but hardly comparable in magnitude to this terrain. The sub-montane belt at the foothills of Siwalik along Himalaya is also very conspicuous, represented by high gradient piedmont zone, the Bhabhar and the adjoining relatively gently sloping Tarai belt. Bhabhar is a zone of unassorted sediments where fans and talus and disappearance of torrents traversing the southern scarp of the Siwalik are the common features, whereas, Tarai represents the zone of seepage. Bhabhar and Tarai also form source region of several streams like Gomati, Sukhata, Deoha etc. The rest of the area is a flat alluvial plain without any marked relief variations. The general slope of the rest of the plain is in south-easterly direction.

2.2.2 Geology and Lithology of Ganga Plain

The Ganga plain of U.P. comprises a thick pile of post Siwalik Quaternary alluvial sediments, overlying a northerly sloping basement (Sastri et al. 1971, 1973) comprising rocks of Bundelkhand Gneissic Complex, Delhi Group, Vindhyan Group and

Siwalik Group. The Peninsular Shield to the south exposes rocks of Bundelkhand Gneissic Complex, Delhi and Vindhyan Groups, whereas to the north of the plains are exposed rocks of Siwalik Group. The Quaternary alluvium of Ganga plain has been classified into Older alluvium comprising Banda alluvium and Varanasi alluvium, and Newer alluvium consisting of Fan alluvium, Terrace alluvium and Recent alluvium (Bhartiya, 1996).

Banda alluvium, comprising of numerous types of clays and red quartzo-feldspathic sands with translucent quartz, feldspar, chalcedony, chert, agate, jasper, fragments of basic rocks etc. The next younger Varanasi alluvium, composed of oxidised silty clay and micaceous grey and brown sand, derived from Himalaya after “post Siwalik Epeirogeny” in Middle Pleistocene, the sedimentation continued up to Late Pleistocene. The Siwalik and a part of Banda alluvium which have been deposited prior to post Siwalik Epeirogeny form basement of Varanasi alluvium.

Newer alluvium overlying Banda/Varanasi alluvium is represented by Fan alluvium near the foothill of Himalaya (Siwalik). The river valleys comprise with Terrace alluvium consisting of grey micaceous, laminated sand and thin beds of silty clay, and Recent alluvium comprising channel/bar deposits within the present bank limits of the respective rivers. Lacustrine deposits at places occurring over Banda/Varanasi alluvium also represent Newer alluvium. These Quaternary deposits have been classified broadly into three litho-stratigraphic units (Table 2-1) representing different cycle of sedimentation in basins of varying dimension and magnitude.

Table 2.1: Classification of Quaternary deposits of Gangetic basin (after Kumar 1996).

Lithounit		Distribution/Lithology
NEWER ALLUVIUM	Channel alluvium	Active channel deposits of light grey, fine to medium grained micaceous sand and pebbles-cobbles (Himalayan provenance) and red Quartz-feldspathic medium to coarse grained sand (Peninsular provenance) along with drapes of silt and clays.
	Terrace alluvium	Older Flood plain deposits (Terraces) composed of grey fine-grained micaceous sand with silt beds in Himalayan river.
	Alluvial Fan Deposits.	Occur on the hill front and composed of sediments ranging from cobbles-pebbles to fine sand and silt.
OLDER ALLUVIUM	Disconformity Varanasi alluvium (VA)	Polycyclic sequence of clay, silt and micaceous sand of Himalayan provenance with <i>Kankar</i> and ferruginous concretions
	Unconformity Banda alluvium (BA)	(b) Chitrakoot Formation medium to coarse quartz feldspathic sand and silt clay of Peninsular provenance with minor <i>kankar</i> . (a) Variegated Clays
PRE QUARTER- NARY	Unconformity Vindhyan Supergroup/ Aravalli Group	Bundelkhand Gneissic Complex in south and (Marwar Supergroup) Lower and Middle Siwalik groups in north

The stratigraphic information obtained from deep wells in Ganga basin can be summarised as follows (Raju and Datta, 1960):

1. The metamorphic basement is probably Aravalli schists and phyllites in the Badaun area. The nature of the basement may differ from one tectonic zone to another as could be visualised from the extension of peninsular Precambrian structural trends into Ganga basin, partly reflected in the aeromagnetic and seismic surveys.

2. Overlying the basement, two major stages of sedimentation can be recognised. The lower stage is a typical platform association of the limestones-orthoquartzite-shale probably ranging from late Proterozoic to Palaeozoic. This association with well-defined folding probably extends as far north as the foothills zone showing a regional increase in the thickness. A regional unconformity representing a long period of hiatus in sedimentation (representing Late Palaeozoic, the entire Mesozoic and Paleogene) intervenes between these older sediments and continental Neogene sands and silts (Siwalik) representing the upper stage of sedimentation. This is particularly impressive all along the southern part of Ganga basin, whereas to the north, nearer the Himalayan foothill, the great thickness of sediments is more than 6 km. The neogene in Ganga basin represents gently dipping monoclinical strata towards the foothills without much structural deformation.
3. The southern limit of Siwalik deposition progressively shifted southward with time along the southern margin of Ganga basin, the youngest Siwaliks or even alluvium rest directly over the Vindhyan or metamorphic basement.

2.2.3 Geomorphology of the Area

The area has been broadly classified into three major geomorphic units e.g., Rocky surface, Upland plain and Flood plain (Figure 2.1). The further subdivision of these geomorphic units along with their elevations, landform elements and aerial distribution are given in Table 2.2.

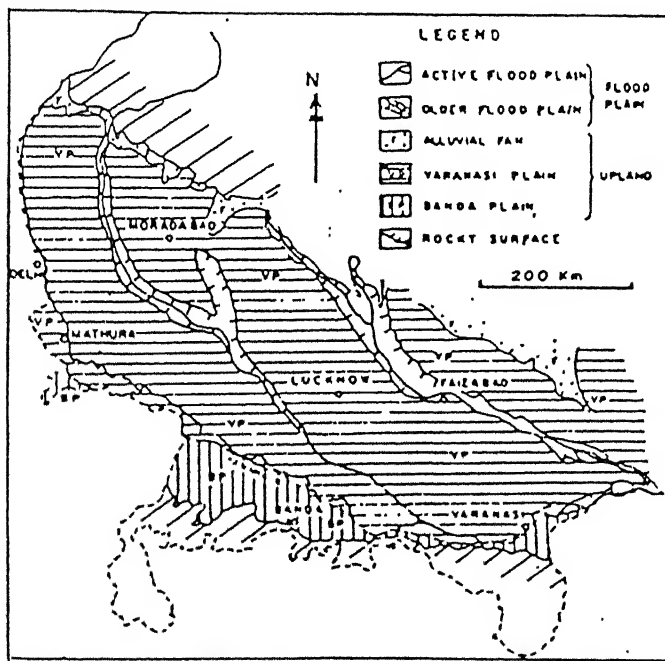


Figure 2.1 Geomorphological map of Ganga plain in U.P. (after Khan, 1996).

2.2.3.1 Rocky Surface

Bundelkhand Gneissic complex surface, Delhi surface and Vindhyan surface forming rocky surface of the south and constituting northern margin of the Peninsular Shield represent the oldest geomorphic unit of the area. Bundelkhand Gneissic complex surface, represent the subdued relief of the ancient most massif, comprises a few hummocks and inselbergs of granite generally 10 m to 80 m high above ground level and at times intruded by longitudinal wall like ridges of quartz reefs and dolerite dykes (Bisaria, 1996). Slopes of these ridges as well as the surrounding areas near foothill are regolith and colluvial materials and are mostly barren due to the absence or very little development of soil profile.

2.2.3.2 Upland Plain

It has been further classified into two sub-divisions e.g., Banda plain and Varanasi plain which represent oldest platform of Quaternary alluvium.

Table 2.2: Geomorphic succession of Ganga plain, Uttar Pradesh (after Pandey, 1996).

Geomorphic units		Elevation above msl in meters	Landform Elements	Distribution
Flood Plain	Active Flood Plain	40 - 300	Point bars, channel bars, lateral bars	Restricted within active channel domain of both Peninsular and Extra Peninsular rivers.
	Other Flood Plain	52-253	Terraces, oxbow lakes, abandoned channels	Confined to terraced valley of present day rivers.
	Alluvial Fan	220-400	Radial drainage, abandoned channels	Near Himalayan foothill in patches.

	Varanasi Plain	60-370	Almost flat surface, tals, palaeo-channels oxbow lakes, sand ridges	South-easterly sloping plain formed by palaeo-Ganga drainage system occupying most of the terrain north of Ganga Yamuna from Ghaziabad to Ballia
Upland Plain				
	Banda Plain	90-160	Undulating surface.	Northerly sloping plain constituted by proto-drainage of peninsular rivers mainly confined to trans-Yamuna area between Agra and Mirzapur.
	Siwalik Structural Hills		Sharp crested hills with steep obsequent and gentle dip slope	From Saharanpur to Tanakpur all along the Himalayan foothills.
	Vindhyan Surface		Plateau and flat topped isolated hillocks.	Near Agra and Between Karvi and Mirzapur.
Rocky Surface				
	Delhi Surface		Ridges	Between Delhi and Mathura
	BGC Surface		Low lying dome shaped hillocks	Between Jhansi and Karvi

Banda Plain: It is an elongated tract covering parts of Bundelkhand and Baghelkhand tracks, the northern boundary of which is defined by Yamuna-Ganga axis and southern boundary by the Peninsular Shield. It mainly exhibits flat to moderately undulating topography with relief variations at micro level. Ravenous badlands stretching over 2 to

3 km wide zones are developed on either sides of the main streams of this plain. The drainage pattern is coarse dendritic to sub-dendritic with a general north-easterly slope.

Varanasi Plain: The vast alluvial terrain sprawling mainly north of Yamuna-Ganga axis up to foothill of Himalaya as well as narrow linear tracts lying marginally to the south of Yamuna-Ganga axis is termed as Varanasi plain. It represents flat to mildly undulating surface with a general south-easterly slope. Topographically the sub-mountain belt along foothill of Himalaya in the northern part of this plain representing Bhabhar and Tarai belt is a significant zone. Bhabhar belt, a piedmont, is a zone of unassorted sediments with fans and talus is a common feature. The Tarai belt represents a zone of seepage with shallow water table. The Bhabhar and Tarai belt also form the source region of several streams like Gomati, Sukhata and Deoha. The Bhabhar belt is a high gradient plain with slope varying from about 10 m/km in the northern part to about 0.40 m/km in the southern part around Tarai Belt. Further, south-eastward the slope of the Varanasi plain goes on decrease which becomes 0.1 m/km in the east. Ganga, Yamuna, Ghaghara and Ramganga are the major rivers draining the area which originate from the Himalaya while Chambal originating from Peninsular shield also forms a part of its drainage basin. The drainage pattern is coarse dendritic to sub-dendritic. Badland topography is observed along the either sides to main streams of the area. This surface comprises scores of fluvial signatures of paleo-drainage system in the form of tals, oxbow lakes, palaeo-channels, and paleo-levees, meander cutoff.

Alluvial Fan: It forms part of the alluvial fan occurring at the foothills of Himalaya. It represents a piedmont zone formed due to coalescence of a number of fans. It mainly comprises coarser gravels, up to boulder size near its apex and sediments become finer (of sand-silt size) in the distal part. It shows steep slope and undulating topography near hill base but gentle slope and mildly undulating topography away from the hill base.

2.2.3.3 Flood Plain

The flood plain of present day rivers like Ganga, Yamuna, Ghaghara, Ramganga and Gomati comprises young geomorphic landforms, which include older flood plain and active flood plain of these rivers.

Older Flood Plain: It represents terraced valley zones of the present day rivers and comprises both erosional and depositional terraces. Most of the rivers originating either from Himalaya or Peninsular shield, as well as alluvial upland have two terraces, one

being erosional and the other depositional except Ghaghara where both the terraces are depositional. Erosional terrace also known as terrace of destruction (Fairbridge, 1968) is the older terrace among the two terraces and represent erosional bench of either Banda alluvium or Varanasi alluvium. This terrace occurring at relatively higher level is generally free from floods. It has moderately undulating topography and comprises abandoned channels, meander scrolls etc. Depositional terrace which represents, the lower level terrace, is occasionally affected by periodic floods. This terrace is made up of the sediments deposited by the streams to which it belongs and hence it is called terrace of construction. It exhibits mildly to moderately undulating topography with landform elements like abandoned channels, meander scrolls, cutoff meanders, crevasse splays, levees, and backswamps. In many rivers at places it has also developed a lower level sub-terrace component bearing resemblance in almost all features and characters with the mother terrace.

Active Flood Plain: This youngest geomorphic unit is restricted in the active zone of channel migration within the present bank lines of all the rivers. The least elevated surface represents active aggradational phase of the present day rivers comprising active landform elements like point bars, channel bars and lateral bars, a few of which are stabilised too.

2.2.4 General Information about Study Area (Kanpur-Unnao)

2.2.4.1 Introduction

The Kanpur-Unnao region is a part of the central alluvial plain with its characteristic landforms. The area under study is located to the left side of Ganga river between Kanpur and Unnao district. Kanpur, the eighth largest metropolis of India, is situated on the right bank of the Ganga river. It is the largest industrial town of the state of Uttar Pradesh. Unnao is situated on the left side of the Ganga river. The climate of the area is humid sub-tropical type. It is divided into three seasons: cold, hot, and monsoon. The highest temperature is about 42° C and the lowest is less than 10° C. The area receives annually $1 \times 10^6 \text{ m}^3$ of water/km² (Ansari, 1998). For the greater part of the year, high temperature prevails over the area and a large amount of water is lost by evaporation.

2.2.4.2 Subsurface Stratigraphy of Kanpur Area

Bajpai (1989) has given the subsurface stratigraphy of the Marginal Gangatic plain of Uttar Pradesh using lithological information from borehole data of the Central Ground Water Board (CGWB) and other Groundwater Organisations. Figure 2.2 represents a transverse (N-S) section from Kabrai in Hamirpur District to Unnao. This section shows basement at shallow depth (<100 m) up to Ghatampur in Kanpur District, it deepens suddenly near Panki (Kanpur District) and northwards, producing a highly variable alluvial thickness.

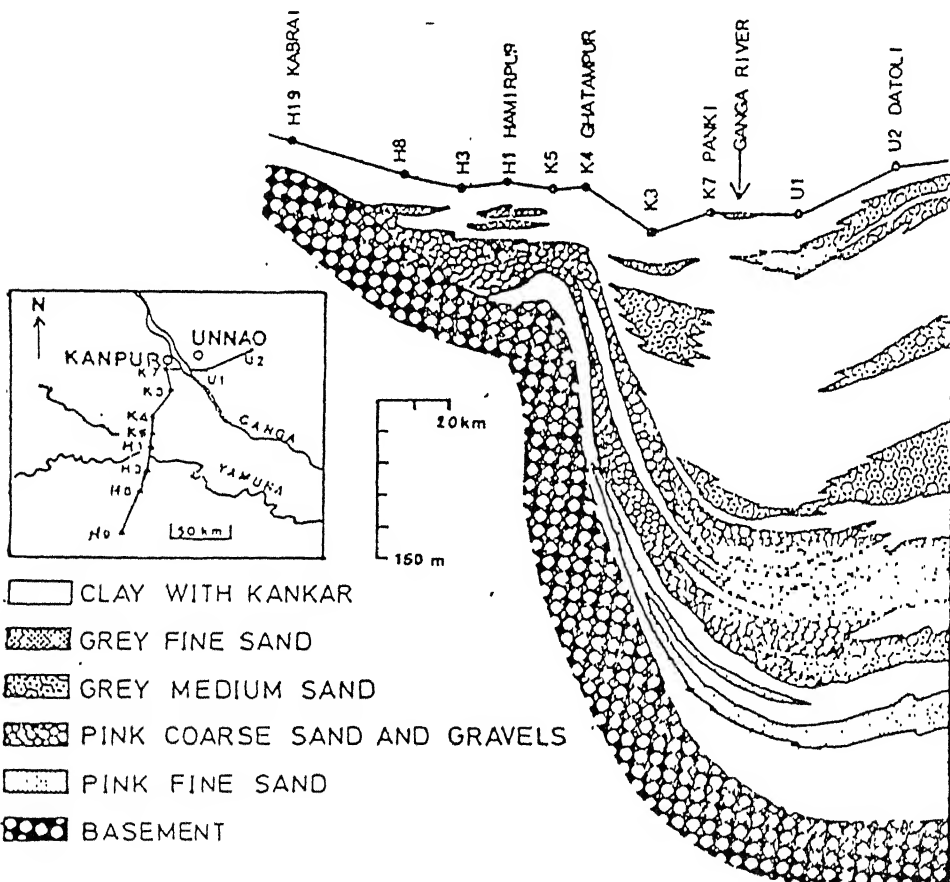


Figure 2.2 Subsurface stratigraphy of alluvium in southern margin of Gangatic plain (redrawn after Bajpai et al, 1989).

An important aspect of this subsurface stratigraphy is that in the northern part there is an important sandy (aquifer) zone between 270-370 m depth, which is made up of pink

colour arkosic coarse sand and gravel (characteristic of all rivers coming from south). Below this zone are few horizons of fine-grained arkosic sands. These sandy horizons occurring in depths of less than 270 m are, however, of micaceous grey-sand type having Himalayan source. Between 270 to 300 m of depth sands show mixed sources. In the southern part, just above the shallow basement, a thick sequence of coarse-grained pink-coloured arkosic sand is followed on top by deposits of clay with kankar and fine-grained micaceous sand of Himalayan source. This subsurface stratigraphy demonstrates the following salient points:

Initially, the rivers from Peninsular India were bringing fine arkosic sand and depositing on the slowly subsiding basement north of the present-day Ganga river. During this period the southern margin of the Gangetic plain was just south of Kanpur, and Ganga river was non-existent (Stage 1).

A rejuvenation in relief, possibly due to thrust-fold loading in the Himalayan region caused an uplift of the Bundelkhand region (a peripheral upward) and rivers started bringing coarse-grained arkosic sand from the south (stage 2). The concurrent rejuvenation of relief in the Himalaya caused increased sediment supply from the Himalayan source and a southward shift in the depocentre. In Kanpur region, inter mixing of sediments from two distinct sources took place (stages 2 and 3) (Bajpai et al, 1989). Simultaneous activation of an E-W lineament caused gravity faulting and active subsidence of the area near Panki (Kanpur) in comparison to the area further south. Increased subsidence near Kanpur caused development of thick sand bodies (stage 4). Subsequently, the Himalayan source drainage and sediments, overlapped the southern source sediments, causing a southward shift in the southern drainage. The continued higher subsidence rate in the region north of the present-day Ganga river further enhanced the difference in the thickness of alluvium from south to north. For a long time Kanpur was an area where a major southern drainage met a major northern drainage, a situation analogous to Allahabad today.

Figure 2.3 depicts the evolution of stratigraphy in Kanpur region sketched above. Though, no absolute dating is available, (Bajpai et al, 1989) proposed that the phase of coarse sand-gravel deposition near Kanpur corresponds to the Middle Pleistocene uplift in the Himalaya, when supposedly uplift of few thousand metres took place.

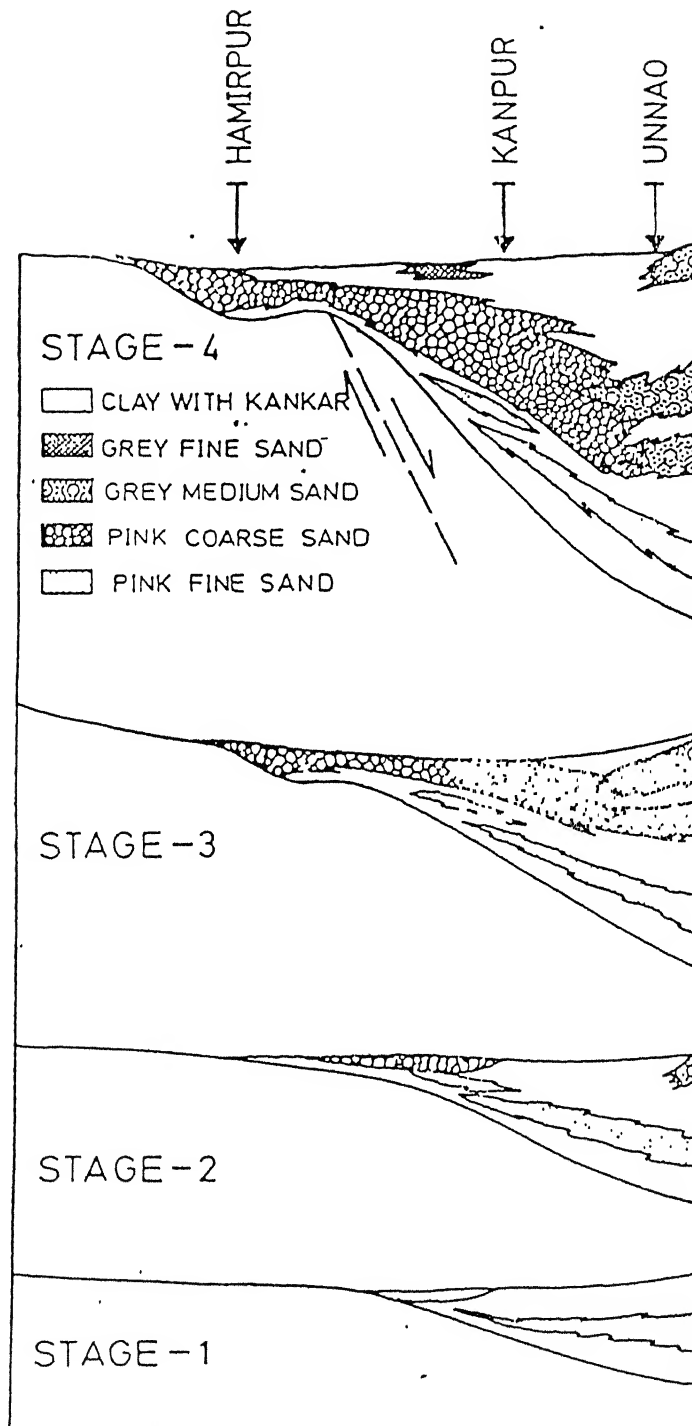


Figure 2.3 Schematic diagram showing evolution of southern margin of Gangatic alluvium (after Bajpai et al, 1989).

2.2.5 Tectonic Frame work of Ganga Basin

A total of 15 boreholes touching the basement floor have been taken into consideration along section profile X-Y (Figure 2.5). The earlier studies have revealed that there are atleast ten NE-SW trending cross faults of significance which have not only affected the Neogene-Quaternary sediments but moved down to their basement floor (Figure 2.4) and thus have controlled the configuration of the basin. The studies have also shown that the entire stretch of the southern part of the Gangetic plain of U.P. between the Aravalli range in the west and the concealed Monghyr-Saharsa ridge in east remained a positive land-mass till beginning of Late Pliocene (Figure 2.6). The faults 1, 4, 7 and 10 are the oldest, possibly developed after Vindhyan sedimentation but prior to Banda alluvium sedimentation. Due to these faults, the Vindhyan sediments are preserved in two grabens separated by a horst of Bundelkhund Gneissic Complex bounded on either sides by faults 4 and 7. The strong tectonic movements during Late Pliocene, the fault-10 marking the eastern limit with Monghyr-Saharsa ridge, was reactivated, and a new fault-2 developed in western part, along which the entire area lying between the two, down faulted to give rise to a basin for the deposition of Banda alluvium (Figure 2.6). The sedimentation in this basin continued till early Middle Pleistocene, when the entire area has been uplifted with reactivation of existing faults and development of new faults (5, 6, 8 and 9). The entire Faizabad ridge acted as a graben but sub-divided into two grabens and a horst structure. Vindhyan graben east of Faizabad ridge bounded by faults 7 and 10, acted as a horst with a development of small graben limited on either side by faults 8 and 9. The area west of Faizabad ridge has been relatively uplifted.

The studies also pointed to pivotal nature of faults due to which the northern part of the Gangetic plain relatively subsided as compared to upliftment along southern margin of the basin. This has lead to the development of a new basin Indo-Gangetic basin for the deposition of the Varanasi alluvium commencing from Middle Pleistocene. This new basin laterally extended covering the entire Monghyr-Saharsa ridge in east and part of the Aravalli range in the west.

The epiorogenic movements during Late Pleistocene times again changed the general scenario of this great alluvial basin. The Varanasi alluvium sedimentation culminated and was subjected to peneplanation, giving rise to Indo-Gangetic plain. During Holocene period, the Faizabad ridge further subsided with upliftment of sub-block limited in fault 5 and 6. All the pre-existing faults except 9 have been reactivated and a new fault-3 developed in the western part of the basin. The area to the west of

ridge uplifted in step like manner, along faults 1, 2, 3 and 4. The area to the east of Faizabad ridge lying between faults 7 and 8 has been uplifted, while that lying between faults 8 and 10 subsided giving rise to a large graben with upliftment of Monghyer-Sahrassa ridge. Fault-9 remained dormant during this period.

The step like movement along faults 1 to 4 probably resulted in maximum upliftment of Aravalli range and development of south-easterly slope to the Gangetic plain controlling the flow trend of the rivers (Ghosh and Singh, 1988). The development of wide flood plain with Holocene Terrace alluvium in the Ganga river upstream of the fault-5 may be related to this step type of faulting where the western part of each block relatively subsided as compared to eastern one. The wide flood plain in the Ganga river down stream of fault-8 could be related to large graben developed west of monghyr-Sahrassa ridge.

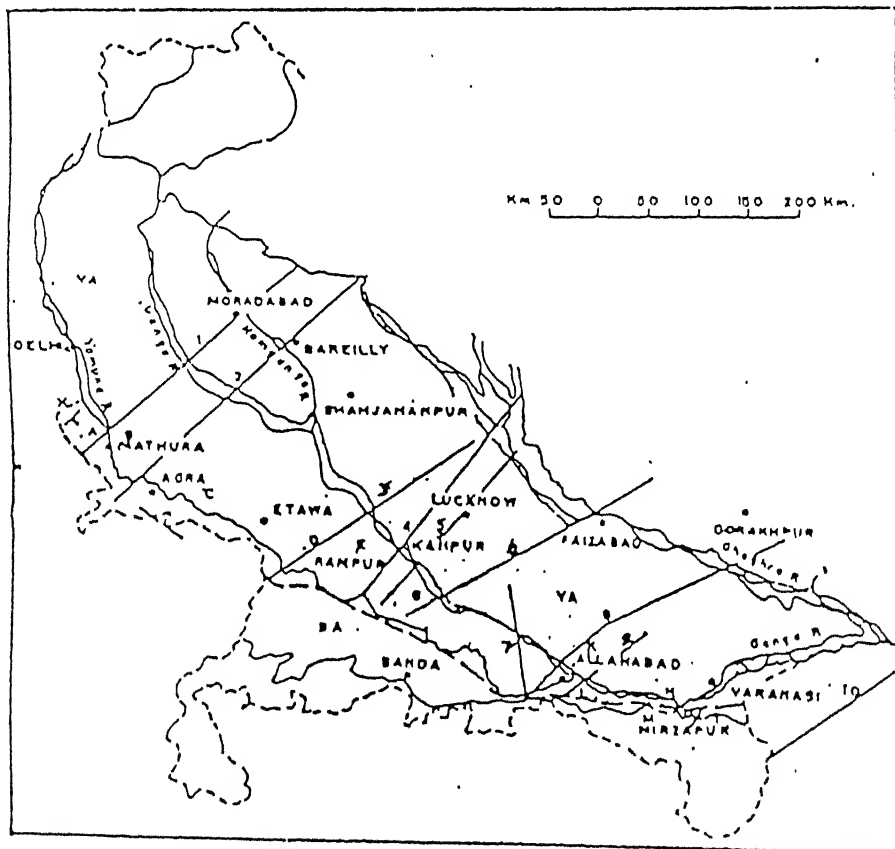


Figure 2.4 Sketch Quaternary geological map of Ganga basin showing locations of cross faults in the basement (after Khan et al, 1996).

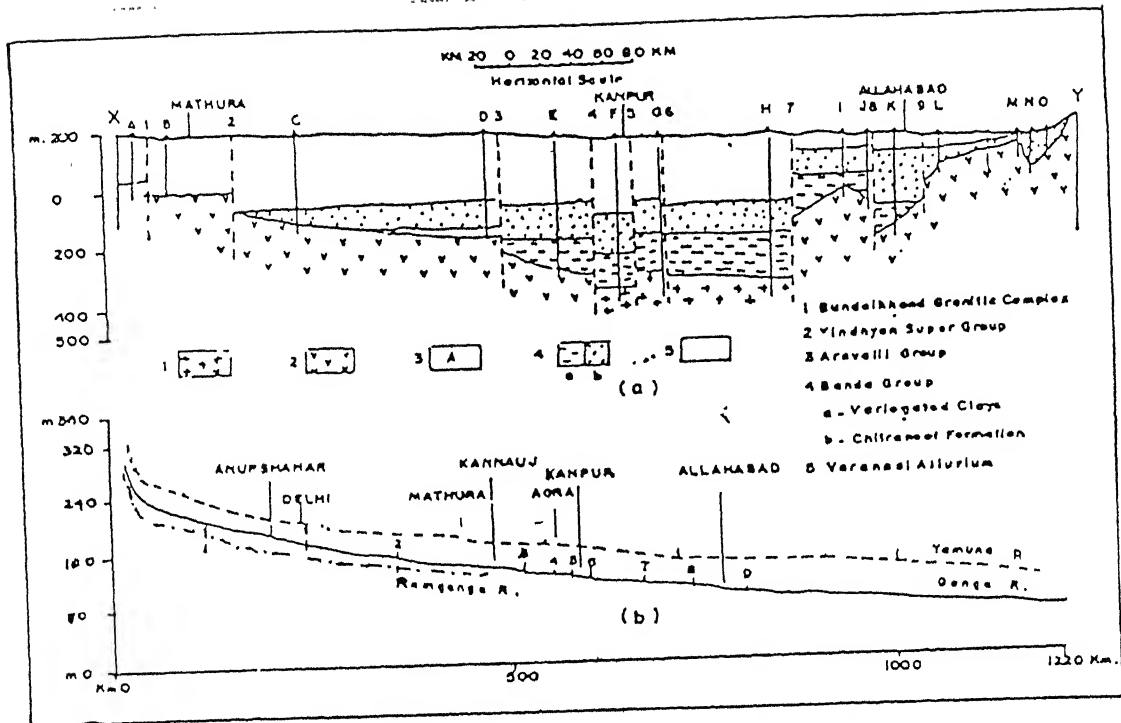


Figure 2.5 Geological cross section along profile X-Y based on borehole data (after Khan et al, 1996).

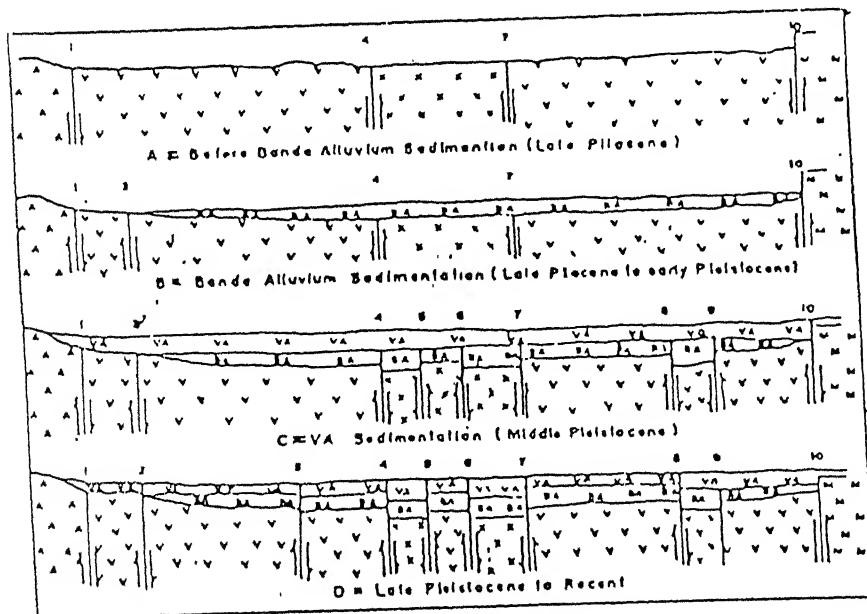


Figure 2.6 Schematic diagram showing successive neotectonic block movement during different periods (after Khan et al, 1996).

2.3 GEOPHYSICAL INFORMATION ABOUT THE AREA

The Indo-Gangatic basin is filled mostly with Late Tertiary and Quaternary sediments. A gradual thickening of the sedimentary layer from the Peninsular shield toward the Himalayan foothills was inferred by Oldham (1917) on the basis of gravity data. Recent, aeromagnetic surveys, geophysical ground surveys and borehole data have indicated substantial variations in the thickness of the sedimentary overburden and uneven basement topography. Seismic surveys have been particularly useful in confirming the existence of buried ridges and basement upwards.

2.3.1 Gravity Results

A composite Bouguer anomaly map of Punjab and Ganga basins (Figure 2.7) has been prepared by using several sources (Choudhury, 1975 Balakrishna and Choudhury 1979, Raiverman et al. 1983). Generally, the values are fairly reliable over the Gangetic plains. The contour interval is 10 m Gal. A few interesting observations from the gravity anomaly map are given below.

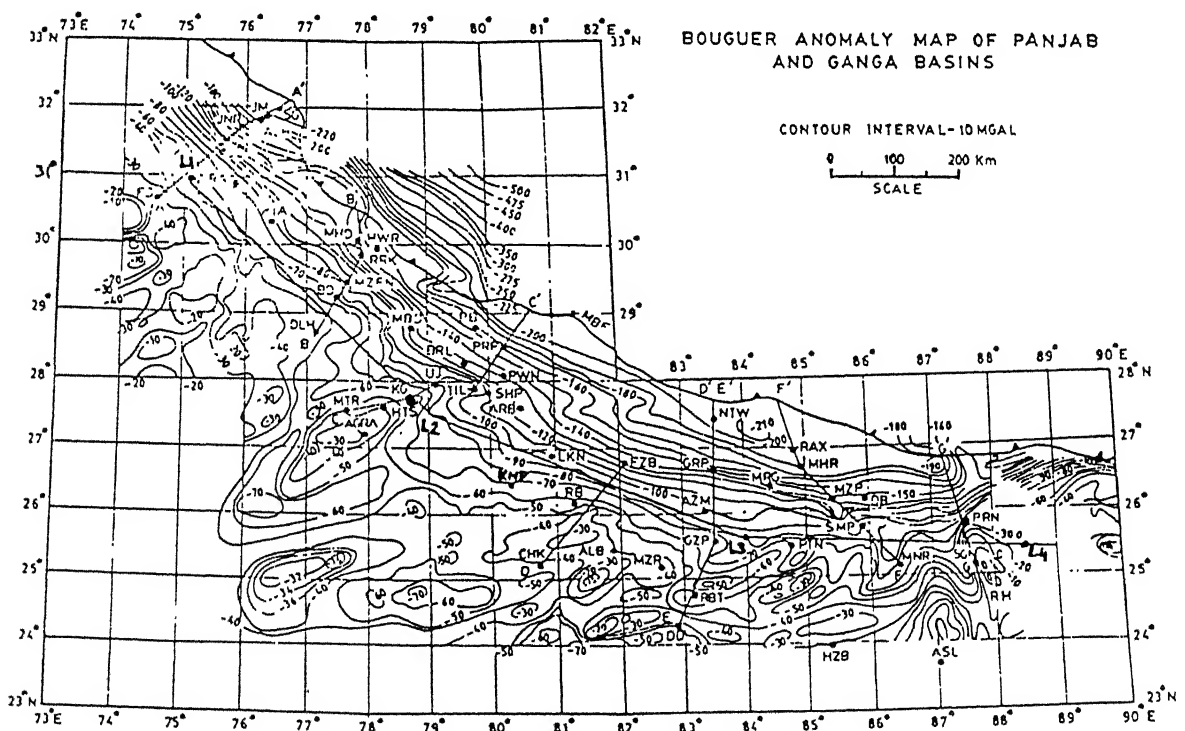


Figure 2.7 Bouguer anomaly map over Ganga basin (after Verma, 1991)

- Gravity contours have a WNW-ESE trend over the Punjab plains which becomes generally east-west over the Ganga basin.
- Bouguer anomaly of the order of -50 m Gal has been found over the edge of the Peninsular shield and becomes increasingly negative towards the Himalayan foothills. Near the main boundary fault (MBF) in Punjab basin, the values are nearly -250 mGal, while over the Gandak depression the minimum value is nearly -210 mGal. The gravity anomaly values become increasingly negative over the Lower Himalays, reaching -450 mGal over the Higher Himalayan region (Verma, 1991).
- Gravity contours show large variations from Delhi towards Moradabad and Mathura towards Tihar, suggesting the presence of a ridge type structure underneath the alluvium or Upper Tertiary sediments.
- Gravity field does not show up as a prominent high over the Faizabad ridge.
- Gravity field is much disturbed over Monghyr-Saharsa ridge, particularly in the area east of Patna. A part of this disturbance could be due to density variations within the crystalline basement.
- A prominent gravity high is located over the Rajmahal hills.

Profile $L_1 L_2 L_3 L_4$ has been drawn nearly parallel to the axis of the Ganga basin, from the west to east. The basement depth (Karunakaran and Ranga Rao, 1979) and Bouguer anomaly have been shown along the profile as shown in Figure 2.8. This Figure shows that the basement depth is nearly 500-700 m below the surface in the area between Zira and Ujhani. Close to the Moradabad fault (F_1), the basement drops down from 750 to about 1000 m. Farther east, near Agra-Tilhar fault (F_2), the basement shows a sharp change from 1000 m to 2500 m. The Agra-Tilhar fault appears to be a major fault, which has controlled the pattern of sedimentation in the western part of Ganga basin. The fault trends NE-SW from Agra towards Ujhani. Thereafter, it trends almost E-W towards Tilhar and beyond. The down-thrown block in this part is towards the south. East of this fault, the basement rises to nearly 1500 m along the fault (F_3) and goes down to nearly 2500 m over the western U.P. shelf. The gravity field shows a major low (-100 mGal value) over the western U.P. basin. East of the Lucknow fault (F_4), the basement rises from 2500 m to about 800 m underneath the Faizabad ridge. The gravity field over the ridge shows no significant variations. East of Faizabad ridge the basement drops down to about 2000 m over the eastern U.P. shelf. The profile passes eastward over Patna fault

before entering the Monghyer-Saharsa ridge (MSR). The Bouguer anomaly, at a level of about -80 to -90 mGal over the eastern U.P. shelf, rises to about -20 mGal over the MSR.

The major difference between the Faizabad ridge and the Ganga basin to its east and west lies in the thickness of the Upper Tertiary sediments. The Vindhyan as well as the Upper Tertiary sediments appear to be fairly thick underneath the western as well as eastern U.P. shelves, compared to the area over the Faizabad ridge. The Vindhyan sediments, consisting mostly of quartzites, compact sandstones and phyllites (at places limestones), are of fairly high density (2.55 to 2.60 g/cm³) and do not contribute much to the gravity anomaly. The Siwalik sediments, being of low density (2.1 to 2.3 g/cm³), play a dominant role in controlling the gravity field. Although the gravity field over the Punjab and Ganga basins is influenced a great deal by the thickness of the Upper Tertiary sediments, this is by no means the only factor. The crustal thickening appears to contribute appreciably to the gravity field.

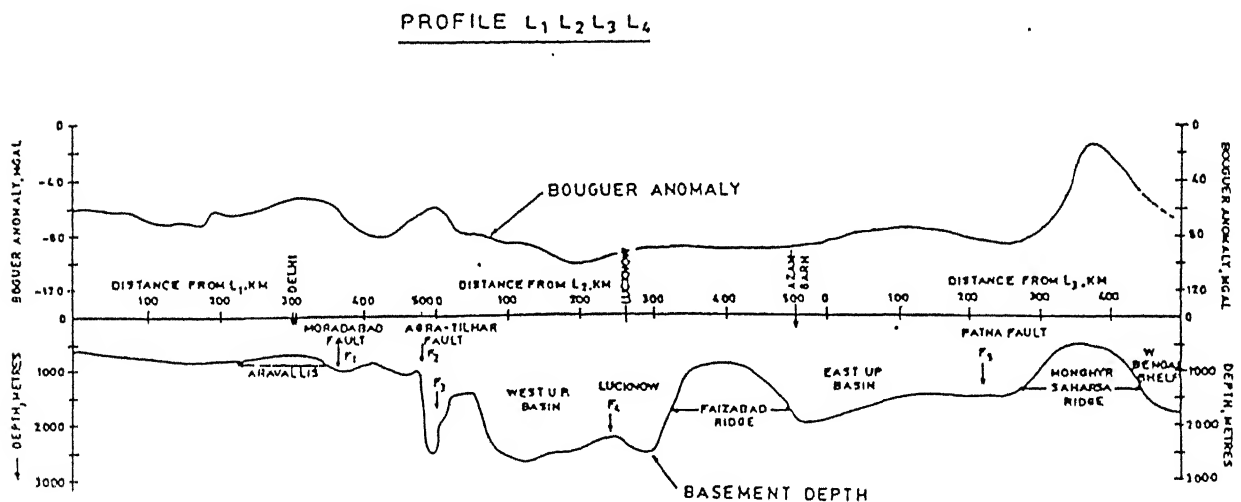


Figure 2.8 Profile L₁L₂L₃L₄ nearly parallel to axis of Ganga basin, showing the major structures and nature of Bouguer anomaly.

2.3.2 Seismic Studies

Three regional seismic profiles have been carried out by Oil and Natural Gas Commission in the Ganga basin north of the exposed Vindhyan. These profiles are (i) Pilibhit-Hathras profile, (ii) Pilibhit-Bisalpur-Lucknow-Raebareli profile, and (iii) Nautanwa-Gorakhpur-Ghazipur profile. The seismic sections along these profiles have been extrapolated to the exposed Vindhyan outcrops towards south and south-west based

on geological investigations. The depth sections along the three profiles are shown in Figure 2.9 (Rao 1973, and Karunakaran and Ranga Rao, 1979). In this section, the top of the Vindhyan formations below the Siwalik has been demarcated as an unconformity surface. It was not possible to demarcate the boundary between the Lower and Upper Vindhyan very clearly and, therefore, the two have been taken to represent together the total thickness of the Vindhyan sediments both in the outcrop area covered by geological studies and in the Ganga Valley covered by seismic studies. Similarly, it has not been possible to demarcate clearly the boundaries between the Lower, Middle and Upper Siwalik and hence the three profiles have been taken to represent together the total thickness of the Siwalik sediments. On the basis of these three profiles, four maps have been prepared (a) Basement contour map of the Vindhyan basin, (b) Isopach contour map of the Vindhyan formations, (c) Contour map showing top of the Vindhyan, and (d) thickness of the Siwalik. Most of the geological sections, prepared by the ONGC, are based on the available seismic information. The seismic wave velocities obtained for different formations are given in Table 2.3. The velocity values have been converted into density using the well-known velocity versus density relationship obtained by Ludwig, and Nafe (Verma, 1991).

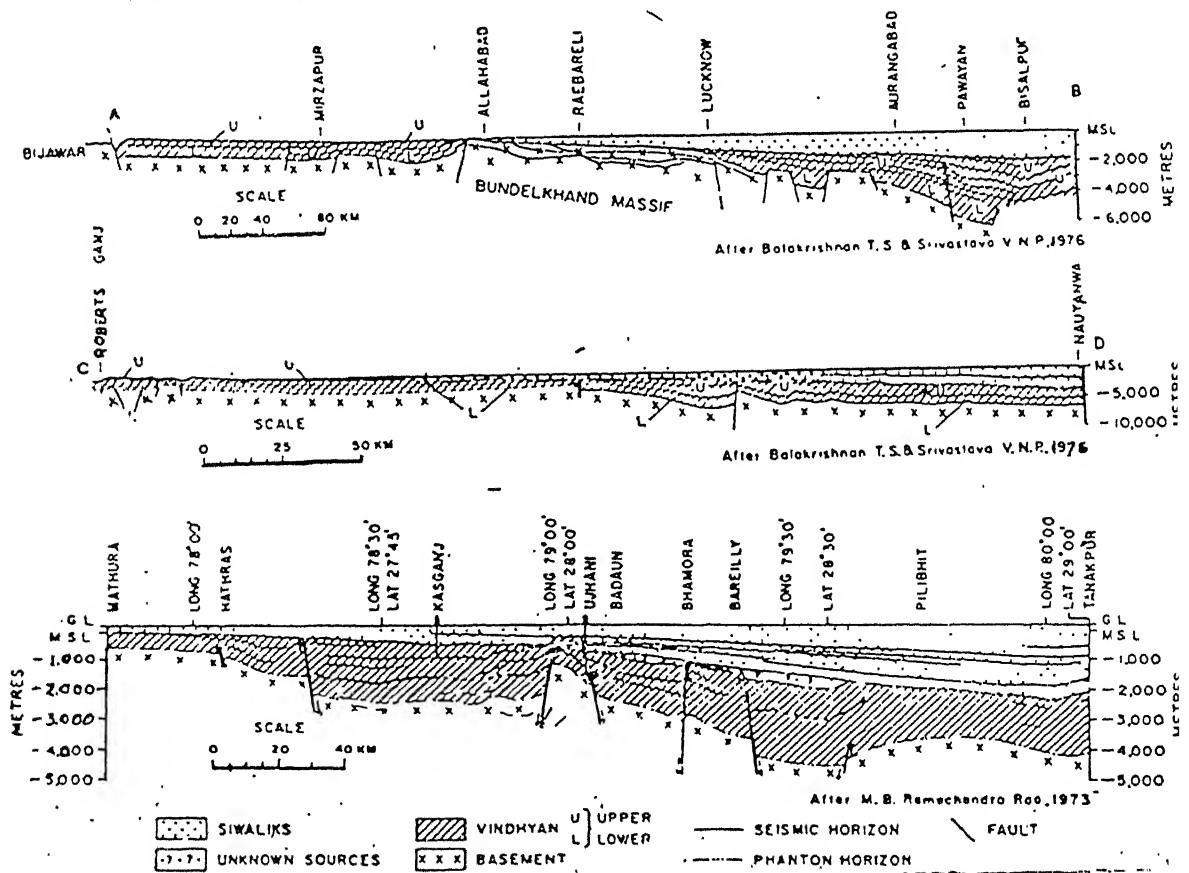


Figure 2.9 Cross section based on seismic and geological data (after Verma, 1991)

Table 2.3: Available seismic information for different formations
from available sources (Verma, 1991).

Sl. No.	Formation	Location	Depth (km)	Velocity (m/sec.)	Density (g/cm ³)
1.	Upper Siwaliks	Adampur-Hoshiarpur	1.0	2400-2600	2.07-2.14
2.	Middle Siwaliks	Adampur-Hoshiarpur	2.0 to 2.2	3000-3500	2.2-2.3
3.	Lower Siwaliks	Hoshiarpur	2.0-3.0	4500	2.45
4.	Lower Siwaliks	Janauri	3.0	4500	2.45
5.	Lower Siwaliks	Janauri-Gagret-Dhamsala	-	4500-4800	2.45-2.50
6.	Lower Dhamsala	Janauri	5.0	5400	2.6
7.	Vindhya	Muzaffarpur	2.8	5200	2.5-2.6
8.	Basement	Janauri	5.0	6000	2.7
9.	Basement	Janauri-Balh area	5.0	6100	2.72

2.3.3 Aeromagnetic Survey in the Ganga Basin

The aeromagnetic survey has been carried out over an area of more than 220,000 sq km of Ganga-Brahmaputra plains, and the depth to the basement has been estimated at different places distributed throughout the Ganga valley (Agocs, 1957). These results have been reviewed by Srivastava (1970). On the basis of qualitative and quantitative studies of aeromagnetic data the Ganga basin has been subdivided into several tectonic units separated by basement high (Figure 2.10). (Eremenko and Negi, 1968). These tectonics units are:

- A shallow basin extending NW of Moradabad having a minimum depth of about 5000 m of the basement.
- A deep basin stretching from Moradabad to Lucknow (upto longitude of 82°). This maximum depth to the basement in this basin is around 6000 m. This basin is separated from unit (i) above by a basement fault trending NE-SW through Moradabad. The basement dips in the NE direction.
- Basement uplift trending NE-SW in the Faizabad area may be the subsurface extension of the Bundelkhand massif.
- A deep basin stretching from NE of Faizabad up to Motihari.
- A basin of intermediate depth east of Darbhanga and extending upto Purnea.

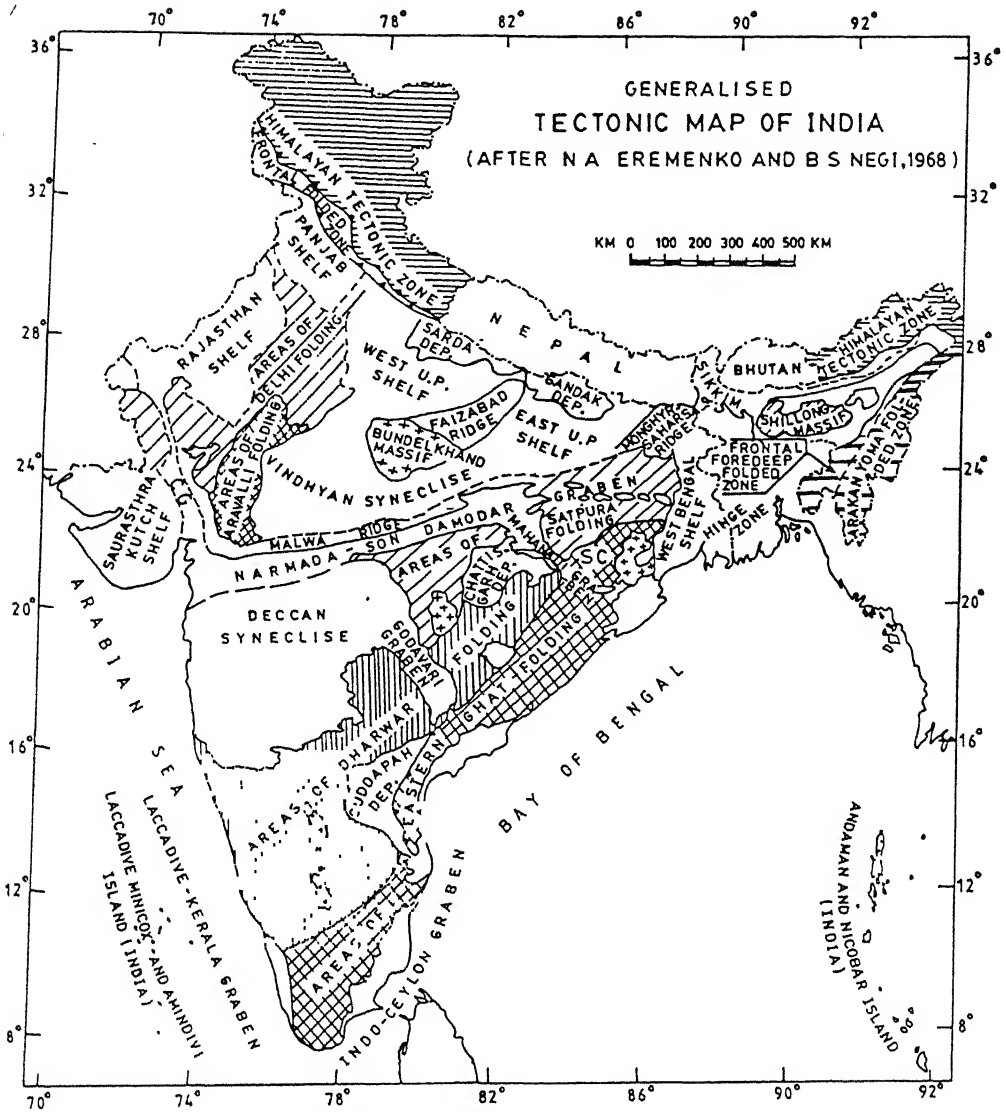


Figure 2.10 Tectonics map of India (Eremenko and Negi, 1968).

Chapter III

DETAILS OF IMAGE PROCESSING AND RESISTIVITY METHOD

3.1 GENERAL

This Chapter presents details of image processing and theory of data merging and brief discussion about edge extraction operators, which have been used in the present work. A brief discussion is provided on the resistivity method, which has been used to determine the subsurface resistivity variations. The present study involves following three major steps to achieve the objectives of the work:

- Data merging technique
- Edge detection
- Resistivity Survey

3.2 DATA MERGING

The necessity of other sensors data for better resolution has attracted many scientists to develop data merging techniques. In this section data merging techniques are reviewed.

3.2.1 Review of previous research

Haydn et al. (1982) have used the first time the intensity hue saturation (IHS) procedure. They merged Landsat multi-spectral scanner (MSS) data with the return beam vidicon (RBV) data and Landsat MSS with heat capacity mapping mission (HCMM) data. The IHS method has also been used by Welch and Ehlers (1987) to merge thematic mapper (TM) and panchromatic (PAN) data of an urban area. They have concluded that the SPOT PAN data could be successfully used to enhance the interpretation of the Landsat TM infrared bands. Thormodsgard and Fequay (1987) have used this method to merge spot multi-spectral and PAN data. Carper (1990) has suggested IHS method to merge SPOT, PAN and XS data. In this method, the intensity component was replaced by weighted average of PAN and XS3 ($[2*Pan+XS3]/3$) to improve the correlation between PAN and the intensity component. The study was conducted on three test sites. The first

site contained both upland and lowland forest types and non-forested wetlands. The second test area consists of urban city and surrounding agricultural and forest areas. The third scene contained mainly bare fields with young corn crops. Carper (1990) has evaluated his results by computing the correlation coefficients between original images and the images after data merging. He has concluded that IHS method is more suitable for areas covered by vegetation as the spectral values are better retained, whereas, the IHS method was quite useful for urban resource inventories. Jutz and Chorowicz (1993) have merged SPOT, PAN and Landsat TM data using IHS approach for detailed geological mapping. Harris and Murray (1990) have used IHS transform to merge radar imagery with other remotely sensed data.

The high pass filter (HPF) method has been used by Chavez (1986) to merge TM data with digitised Panchromatic photograph collected as part of the national high altitude program data. The results were used to generate image products at scales up to 1:24,000. Chavez and Bowell (1988) have also used HPF to merge Landsat TM data with SPOT PAN data of agricultural, urban and geologic sites. They have compared the spectral information content of Landsat TM and SPOT data statistically using the correlation matrix and the principal component analysis, as well as qualitatively through visual comparisons. They have concluded that the SPOT XS (multi-spectral) data for the most part duplicated the spectral information contained in the Landsat TM data, while the Landsat TM data have spectral information not contained in the SPOT XS data.

Chavez et al. (1991) have performed a comparative study of IHS, PCA and HPF methods to merge Landsat, TM, SPOT and PAN data of an agricultural environment with a few small urban areas and a portion of the salt area. The results of the three methods have been compared in three ways: statistical, visual and graphic. Chavez et al. (1991) have concluded that the spectral characteristics of the data have been distorted in ascending order as follows: HPF, PCA and IHS. Pellemans et al. (1993) have used radiometric method to merge SPOT, PAN and XS images of an agricultural area and compared this method with IHS, statistical and spherical co-ordinate methods. They have concluded that the radiometric method preserved the absolute pixel values (radiometric values) while the statistical method gives comparable results. The other two, IHS and spherical methods, provided more contrast in images which can be useful for the visual analysis. Munechika et al. (1993) have proposed a ratio method and have compared the method for merging Landsat, TM, SPOT and PAN data. They have computed the RMS

(root mean square) errors between the original and merged Landsat TM data and carried out a land cover classification, which recorded a 6% increase in the accuracy.

Yocky (1996), Garguet-Duport et al. (1996), and Ranchin (1993) have used the multi-resolution analysis and wavelet transforms to introduce the spatial information into the spectral bands. Garguet-Duport et al. (1996) have compared this method with IHS and P+XS methods to merge SPOT, PAN and XS data for an application in landscape ecology. The study area consists of urban space, wetlands, and farmed zones with various yields and mining ponds. To interpret the performance of the method three criteria have been considered: geometrical improvement, preservation of the spectral characteristics and thematic analysis. It has been found that the wavelet method least distorted the spectral characteristics hence this method is well suited for the study of the vegetation. The visual comparison has indicated that the wavelet method generated results with good spatial resolution similar to IHS method or P+XS method. Yocky (1996) has used standard, additive and selective multi-resolution wavelet decomposition mergers to combine Landsat, TM, SPOT and PAN data and has compared these methods with IHS method. The comparison results have shown that the wavelet mergers provided greater flexibility and capability of preserving spectral values whereas, the IHS method found to change significantly.

Vrabel (1996) has merged multi-spectral and panchromatic data from M-7 airborne sensor. Study was conducted on areas of different combinations like residential and industrial, water treatment plant, storage tanks, agricultural, storage tanks, rail and desert roads, weapons test area and buildings. He has concentrated mainly on three points: validity of concept of effective GSD (ground sample distance), relative utility of band sharpening by different factors and comparison of IHS, HPF, P+XS and sparkle merging methods for various combinations dependent on the bands and the resolutions used. He has concluded that sparkle and P+XS methods give the best results in all the combinations tested. Wald et al. (1997) have used ARSIS, P+XS and duplication methods to merge SPOT, PAN and XS images of an urban area. They have proposed both, a formal approach and some criteria, to provide quantitative assessment of the merged images. Terrettaz (1998) has compared seven merging techniques: HIS, Carper (variant of IHS), HPF, P+XS, radiometric, Price and ARSIS (Ranchin, 1993) to merge SPOT, PAN and XS data in the context of an urban and sub-urban area. They have carried out detailed statistical and visual comparisons. It has been concluded that ARSIS and Price method (Susmitha, 1999) retain the spectral values but the visual improvement

is not very good. The Carper (1990), radiometric and P+XS methods have also preserved the spectral values and achieved some degree of visual improvement but less than that of IHS and HPF methods. The IHS and HPF methods offer well-contrasted colour compositions that are very advantageous for the visual analysis.

Following data merging techniques have been developed recently and details are given in recent literature.

1. High pass filter (HPF)
2. Price algorithm
3. Intensity hue saturation (IHS)
4. P+XS
5. Principal component analysis (PCA)
6. Radiometric integration
7. Statistical method
8. Spherical method
9. Wavelet transform

In the present study, four methods HPF, IHS, P+XS and Price have been used. The details of data merging techniques are given in the following sections.

3.2.2 Data Merging Methods

Data merging is combining of two data sets that are complimentary in nature. This is performed after the images get registered geometrically. This section explains in detail some of the available data merging techniques such as IHS, PCA, HPF, Price algorithm, radiometric, spherical and statistical techniques. The following description provides theoretical details of these methods.

3.2.2.1 Intensity- Hue-Saturation (IHS) method

The IHS method consists of transformation of low spatial resolution data set from the RGB to the IHS co-ordinate system and then the intensity component is replaced by the high-resolution data before carrying out the inverse transformation of the IHS to the RGB space. The use of this method rests upon the assumption that there is a close correlation between the high spatial resolution band and the intensity component. This assumption is valid if the high- and low-resolution bands cover in part at least the same

spectral area. There are two models for representing colours: RGB and IHS models. The RGB co-ordinate system can be represented as a cube with red, green, and blue axes defining the X, Y and Z axes, respectively. The IHS model is hue-intensity-saturation model. The IHS co-ordinate system can be represented as a hexacone, where intensity represents total brightness and is represented by distance above the apex of the hexacone. Hue is the dominant wavelength of the colour and is represented by angular position around the top of the hexacone (0-360 degrees) and saturation is the purity of the colour (i.e. the presence of white light in the image) and is represented by distance from the central, vertical axis of the hexacone.

The advantages of IHS co-ordinate system over RGB system are summarised as follows:

- The ability to vary each IHS component independently, without affecting the others. For example, a contrast stretch can be applied to the intensity component of an image, and the hue and saturation of the pixels in the enhanced image will not be changed.
- The information aspects of an image are presented using readily identifiable and quantifiable colour attributes that can be distinctly perceived.
- In IHS system, numerical variations in the image data can be uniformly represented in easily perceived range of colours.
- The IHS approach may also be used to display spatially registered data of varying spatial resolution. For example, high-resolution data from one source may be displayed as the intensity component, and low-resolution data from another source may be displayed as the hue and saturation components. This advantage is the basis for using IHS transform as a merging technique.

3.2.2.1.1 Steps Applied

1. Transformation of three bands of the lower spatial resolution data set (slave images) from RGB to IHS co-ordinate system, the following important points should be kept in mind:
 - RGB values are converted to 0-1 before conversion to IHS coordinate.
 - IHS hue co-ordinate is rescaled from 0-360 degrees to 0-255 and saturation and intensity coordinates are converted from 0-1 to 0-255 before display.

The Transformation from RGB to IHS system is carried out as described below:

Since hue, saturation, and intensity are three properties used to describe colour, it seems logical that there be a corresponding colour model, IHS. When using the IHS colour space, one does not require knowing what percentage of blue or green to produce a colour. One simply adjusts the hue to get the colour one wishes. To change a deep red to pink, the saturation is adjusted. To make it darker or lighter, the intensity has to be altered to IHS. Many applications use the IHS colour model. Machine vision uses IHS colour space in identifying the colour of different objects. Image processing applications-such as histogram operations, intensity transformations, and convolutions-operate on only an image intensity. These operations are performed much easier on an image in the IHS colour space. IHS is modelled with cylindrical coordinates. IHS, which uses the double cone model, looks like an inverted cone below another cone (Figure 3.1).

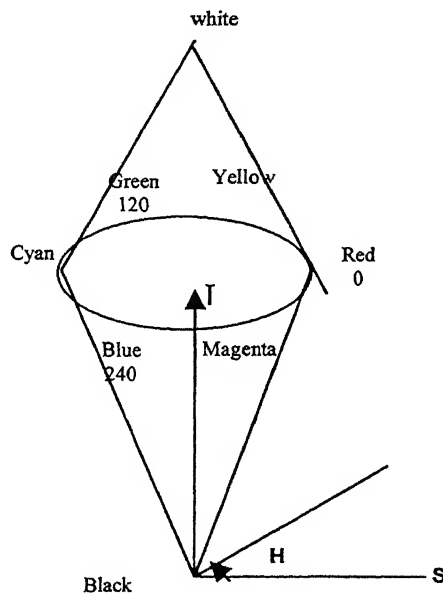


Figure 3.1 Double cone model of the IHS colour space

The hue is represented as the angle θ varying from 0° to 360° . The saturation corresponds to the radius, varying from 0 to 1. The intensity varies along the axis with 0 being black and 1 being white. When $S=0$, the colour is a grey of intensity I . When $S=1$, the colour is on the boundary of top cone base. The greater the saturation, the farther the colour is from white/grey/black (depending on the intensity). By adjusting hue the colour is varying from red at 0° , through green at 120° , blue at 240° , and back to red at 360° . When $I=0$, the colour is black and therefore H is undefined, when $S=0$, the colour is grey scale and H is undefined in this case also. By adjusting I , a colour can be made darker or

lighter. By maintaining $S=1$ and adjusting I , shades of that colour are created. The following formulas show how to convert from RGB space to IHS (Crane, 1997):

$$I = \frac{1}{3}(R + G + B) \quad (3.1)$$

$$S = 1 - \frac{3}{(R + G + B)}[\min(R, G, B)] \quad (3.2)$$

$$H = \cos^{-1} \left[\frac{\frac{1}{2}[(R - G) - (R - B)]}{\sqrt{(R - G)^2 + (R - B)(G - B)}} \right] \quad (3.3)$$

If B is greater than G , then $H=360^\circ-H$.

2. In some cases contrast stretch is applied to high spatial resolution image so that it has approximately the same variance and mean as the intensity component image.
3. Intensity component image is replaced by high spatial resolution image (master image).
4. To convert from IHS to RGB, the process depends on which colour sector H lies in.
For the RG sector ($0^\circ \leq H \leq 120^\circ$):

$$b = \frac{1}{3}(1 - S) \quad (3.4)$$

$$r = \frac{1}{3} \left[1 + \frac{S \cos(H)}{\cos(60^\circ - H)} \right] \quad (3.5)$$

$$g = 1 - (r + b) \quad (3.6)$$

For the GB sector ($120^\circ \leq H \leq 240^\circ$):

$$H = H - 120^\circ \quad (3.7)$$

$$g = \frac{1}{3} \left[1 + \frac{S \cos(H)}{\cos(60^\circ - H)} \right] \quad (3.8)$$

$$r = \frac{1}{3}(1-S) \quad (3.9)$$

$$b = 1-(r+g) \quad (3.10)$$

For the BR sector ($240^\circ \leq H \leq 360^\circ$):

$$H = H - 240^\circ \quad (3.11)$$

$$b = \frac{1}{3} \left[1 + \frac{S \cos(H)}{\cos(60^\circ - H)} \right] \quad (3.12)$$

$$g = \frac{1}{3}(1-S) \quad (3.13)$$

$$r = 1-(g+b) \quad (3.14)$$

The values r , g , and b are normalised values of R , G , and B , which are given below:

$$R = 3/r \quad G = 3/g \quad 100B = 3/b$$

Before display, R , G , B values are rescaled from 0-1 to 0-255. The algorithm has the limitation that only three bands can be merged at any one time.

3.2.2.2 High Pass Filter (HPF)

This HPF method merges the spatial information of the higher spatial resolution data set with spectral information of the higher spectral resolution data set. The high pass filter extracts the high frequency information from the image. The HPF method merges the spatial information of the higher spatial resolution data set with spectral information of the higher spectral resolution data set. In this method high pass filter is applied to the high spatial resolution data and the result is added pixel by pixel to the lower spatial resolution but higher spectral resolution data set. This allows the higher resolution image to be added equally to each of the lower resolution images using the simple pixel addition method without distorting the spectral balance.

3.2.2.2.1 Steps Applied

1. High pass filter is applied on high spatial resolution satellite data.
2. High pass filter can be applied directly on image to get high frequency information. Alternatively, one can first apply low pass filter such as mean filter and subtract this low frequency image from original image to get high frequency image. Procedure to extract high frequency information is explained below:

a) If $n \times m$ be the size of the window of mean filter and $N \times M$ be the size of the image.

- b) The window is placed in the top left corner of the image to be filtered and the average value of the elements in the input image that are covered by the window are calculated. This value is placed in the output image at the point corresponding to location of the central element of the window.
- c) In other words, the window can be thought of as a matrix with all elements equal to 1, the output from the convolution of the window and the image is the sum of the products of the corresponding window and the image elements divided by the number of elements in the window.
- d) If W_{ij} , G_{ij} , O_{ij} represent elements in the mean filter, pixel values in the input image and pixel values in the output image respectively. Then

$$O_{ij} = \frac{\left\{ \sum_{p=-b}^b \sum_{q=-c}^c G_{p+i, q+j} W_{r+p, s+q} \right\}}{mn} \quad (3.15)$$

where

$$b = (n - 1)/2$$

$$c = (m - 1)/2$$

n = number of rows in filter matrix

m = number of columns in filter matrix

r = central row in filter matrix ($b+1$)

s = central column in filter matrix ($c+1$)

i, j = image pixel underlying element (r, s) of the filter matrix

e) The size of the output image O is $(N - 2b) \times (M - 2c)$.

f) Finally, the high frequency image is given by

$$H_{ij} = G_{ij} - O_{ij}. \quad (3.16)$$

3. Now add HPF results pixel by pixel to the lower spatial resolution but higher spectral resolution data set.
4. Finally, we may get images with pixel values greater than 255 or less than 0. Pixel with grey value greater than 255 are assigned to 255 and pixels with grey value less than 0 are assigned to 0.

3.2.2.3 P+XS Method

This method is based on the assumption that band P (Panchromatic) is the sum of the bands XS1 and XS2. In P+XS method, the resultant merged XS images are given by equations (3.36) to (3.37):

$$PXS1 = \frac{2P \cdot XS1}{XS1 + XS2} \quad (3.17)$$

$$PXS2 = \frac{2P \cdot XS2}{XS1 + XS2} \quad (3.18)$$

$$PXS3 = XS3 \quad (3.19)$$

3.2.2.4 Price algorithm

The objective of this merging method is to generate hybrid high-resolution multi-spectral images that attempt to preserve the radiometric characteristics of the original multi-spectral data. In the Price method (Price, 1987), each new band is the result of the combination of the original spectral band and an estimation of this band in terms of the high-resolution band. For the spectral bands closely correlated with the high resolution image, the estimation is obtained by linear regression, whereas, for weakly correlated bands a look-up-table is prepared to obtain the high resolution estimate. The principle behind the wavelet transform method is as follows:

To pass from one level of resolution to a lower level, an image is decomposed into a context image, which represents the approximation of the image at high level resolution, and three detailed images representing the differences, in the horizontal, vertical and diagonal directions between the two levels. These three detailed images correspond to the spatial information of the high-resolution level. They are represented by the wavelet coefficients. If one knows this context image and the detailed images at a level of resolution, then one can reconstruct the high level image. For example, when IRS-1C PAN and LISS-III images are merged, the wavelet transforms are used to extract the spatial structures between 6 and 24 meters in size from PAN and to introduce them into the LISS-III image. The LISS-III wavelet coefficients for resolution between 6 and 24 meters are determined by models, which take into account the PAN wavelet coefficients and those of LISS-III at the other resolution levels.

3.2.2.4.1 Steps Applied

Based on correlation between low-resolution and high-resolution data Price (1987) has proposed a two stage merger method.

Stage 1:

In this stage those low-resolution slave images are enhanced that are strongly correlated with the high-resolution master image and the procedure for this is as follows (Susmitha, 1999).

1. All pixels in the high-resolution master image that fall within a defined superpixel (area comprised by one pixel of slave image) are averaged and a new image (M_{avg}) is formed at the same resolution as the low-resolution slave image.
2. The relation between pixel values of the slave images and master image can be described as linear.

$$S_i = a_i \cdot M_{ave} + b_i \quad (3.20)$$

where

S_i Pixel value of the superpixel in the i th slave image.

M_{ave} Average pixel value in the corresponding superpixel in the high resolution master iamge.

a_i, b_i Least-squares regression coefficients.

3. After solving for a_i and b_i , a high resolution estimate of slave image can be formed as

$$S_i^1 = a_i \cdot M_{hr} + b_i \quad (3.21)$$

where M_{hr} is the high resolution master image.

4. High-resolution hybrid slave image is found out as

$$Hybrid_i = \frac{S_i \cdot S_i^1}{S_{avg,i}^1} \quad (3.22)$$

where

$Hybrid_i$ Pixel value in the i th high resolution hybrid slave image

S_i^1 High-resolution estimate of the i th slave image.

$S_{avg,i}^1$ Average of the pixel values in the S_i^1 image in the corresponding S_i superpixel.

5. Finally, merged images are these hybrid images.

For an illustration, let m be the resolution of slave images and $n = m/2$ be the resolution of the master image where,

- (a) is slave image with resolution m
- (b) master image with resolution n
- (c) averaged master image with resolution m
- (d) high resolution estimate (S_i^1) of the slave image with resolution n
- (e) averaged image of high resolution estimate ($S_{avg,i}^1$) with resolution m
- (p) merged hybrid image (hybrid_i) with resolution n

$a, b, c, d, e, p, q, r, s, x, y_1, y_2, y_3, y_4, z$ represent pixel values.

$$e = \frac{a + b + c + d}{4} \text{ and } z = \frac{p + q + r + s}{4},$$

$$p = a_1(a) + b_1$$

Similarly for q, r , and s ; where a_1 and b_1 are regression coefficients,

$$y_1 = \frac{x}{z}(p), y_2 = \frac{x}{z}(q), y_3 = \frac{x}{z}(r), y_4 = \frac{x}{z}(s)$$

Stage 2:

In this stage the weakly correlated slave images are enhanced. Here, relationship between the low-resolution slave images and the high-resolution master image can not be considered linear. In this stage a look-up-table is computed. This stage involves the following steps (Shaban, 1999).

1. All pixels in the high resolution master image that fall within a defined super pixel are averaged and a new image (M_{avg}) is formed at the same resolution as the low resolution slave image.
2. To prepare a look-up-table, mean values of the pixel values in the weakly correlated slave images that fall in the same locations as the individual values in the averaged master image are computed.
3. Referring to the high-resolution master image and look-up-table, place the mean values of the pixel values in the weakly correlated slave image as pixel values in high

resolution estimate of the i th slave image i.e., S_i^1 image in the same locations as the individual values in the high-resolution master image.

4. Hybrid image of i th slave image is found out as

$$Hybrid_i = \frac{S_i \cdot S_i^1}{S_{avg,i}^1} \quad (3.23)$$

where

$Hybrid_i$ Pixel value in the i th high resolution hybrid slave image

S_i^1 High-resolution estimate of the i th slave image.

$S_{avg,i}^1$ Average of the pixel values in the S_i^1 image in the corresponding S_i super pixel.

5. Finally, the merged images are these hybrid images.

(a) slave image with resolution m

(b) master image with resolution n

(c) averaged master image with resolution m

(d) look-up-table to determine high resolution estimate

(e) high resolution estimate (S_i^1) of slave image with resolution n

(f) averaged image of high resolution estimate ($S_{avg,i}^1$) with resolution m

(g) merged hybrid image (hybrid i) with resolution n

where, y_1, y_2, y_3, y_4 are calculated in the same manner as that of stage 1 such that

$$y_1 = \frac{8}{5}(6), y_2 = \frac{x}{z}(4), y_3 = \frac{x}{z}(4), y_4 = \frac{x}{z}(6).$$

3.3 EXTRACTION OF EDGES

One of the objectives of the present work is to emphasise the edges which are related to lithological contrast from an image using different operators and to understand the effect of data merging on extraction of edges especially on thresholding technique. So, it is necessary to have a brief idea on edge extraction procedure. The present section explains a brief idea about the edge operators, which has been used in this study.

3.3.1 Introduction

The edges of an image hold much of the information in that image. The edges tell where objects are, their shape and size and something about their texture. An edge is where the intensity of an image moves from a low value to a high value or vice versa. Information obtained from the images can be divided into two types, low frequency information and high frequency information. The slowly varying background pattern can be considered as low frequency information and the rapidly varying details can be treated as high frequency information. The filters that extract low frequency informations are called as low-pass filters and those extract high frequency informations are called high-pass filters. The high-pass filtered image can be used alone, particularly in the study of location and geographical distribution of edges. An edge is a discontinuity or sharp change in the greyscale value at a particular pixel point and it may have some interpretation in terms of geological structure or relief. An edge in the digital image occurs at the boundary between two pixels when the respective grey level values of these adjacent pixels are significantly different. Edges are generally found because of changes in some physical and surface properties such as change in soil characteristics illumination, geometry (orientation, depth) and reflectance. An edge can be either physical or an intensity edge. A physical edge is one, which is actually present as a surface discontinuity whereas, an intensity edge is one, which is detected as sharp change in adjacent intensity values in an image. Some intensity edges (like shadow caused by a strip of trees) do not correspond to an existing physical edge in nature.

3.3.2 Edge detection

The different approaches for spatial edge detectors can be categorised into linear, non-linear or best-fit methods (Peli and Malah, 1982). Linear methods involve edge detection based on differencing, such as first order derivatives evaluated in two directions (Rosenfeld and Kak, 1982) or in four directions (Pratt, 1977). Second order derivative operators like Laplacian and Laplacian of Gaussian (LOG) (Argyle, 1971; Macleod, 1972) also come under linear approach. The non-linear approaches include Roberts and Sobel operators (Hall, 1979) or mask matching approaches such as Prewitt and Kirsch operators (Rosenfeld and Kak, 1982). The best fit methods involve fitting a simple function to the data and then using either the local gradient or deviations from it (Rosenfeld and Kak, 1982; Nalwa and Binford, 1986) or defining the edge as an intersection between different functions (Burns et al., 1986). These wide ranges of

approaches have been summarised by Davis (1975), Rosenfeld and Kak (1982), Pratt (1977), and Hall (1979). Apart from these, morphological operators are also available for the edge detection. Morphological operators are transformations of signals based on the theory of mathematical morphology (Cappellini et al., 1990; Haralick et al., 1987). Four morphological operations are erosion, dilation, opening and closing (Cappellini et al., 1990). Levialdi (1983) has classified the edge operators based on their originating approach as: local, regional, global, heuristic, dynamic and relaxation. The following is the list of the various commonly used edge operators:

- Linear operators
 - First order derivative
 - Second order derivative
 - Laplacian
 - Laplacian of Gaussian
- Non-linear operators
 - Roberts
 - Sobel
 - Prewitt
 - Frei-Chen
 - Kirsch
- Morphological operators

3.3.2.1 Sobel Operator

The Sobel edge detection masks look for edges in both the horizontal and vertical directions and then combine this information into a single metric. The masks are as follows:

ROW MASK

$$\begin{bmatrix} -1 & -2 & -1 \\ 0 & 0 & 0 \\ 1 & 2 & 1 \end{bmatrix}$$

COLUMN MASK

$$\begin{bmatrix} -1 & 0 & 1 \\ -2 & 0 & 2 \\ -1 & 0 & 1 \end{bmatrix}$$

These masks are convolved with the image. At each pixel location we now have two numbers: s_1 , corresponding to the result from the row mask, and s_2 , from the column

mask. We use these numbers to compute two matrices, the edge magnitude and the edge direction, which are defined as follows (Richards, 1993):

EDGE MAGNITUDE

$$\sqrt{s_1^2 + s_2^2} \quad (3.24)$$

EDGE DIRECTION

$$\tan^{-1} \left[\frac{s_1}{s_2} \right] \quad (3.25)$$

The edge direction is perpendicular to the edge itself because the direction specified is the direction of the gradient, along which the grey levels are changing.

3.3.2.2 Laplacian Operators

The Laplacian operators described here are similar to the one used for pre-processing as described in section 2.2.3. The three Laplacian masks that follow represent different approximations of the Laplacian operator. Unlike compass masks, the Laplacian masks are rotationally symmetric, which means edges at all orientations contribute to the result. They are applied by selecting one mask and convolving it with the image. The sign of the result (positive or negative) from two adjacent pixel locations provides directional information, and tells us which side of the edge is brighter.

LAPLACIAN MASKS

$$\begin{bmatrix} 0 & -1 & 0 \\ -1 & 4 & -1 \\ 0 & -1 & 0 \end{bmatrix} \quad \begin{bmatrix} 1 & -2 & 1 \\ -2 & 4 & -2 \\ 1 & -2 & 1 \end{bmatrix} \quad \begin{bmatrix} -1 & -1 & -1 \\ -1 & 8 & -1 \\ -1 & -1 & -1 \end{bmatrix}$$

These masks differ from the Laplacian type previously described in that the center coefficients have been decreased by one. With these masks we are trying to find edges and are not interested in the image itself. An easy way to picture the difference is to consider the effect each mask would have when applied to an area of constant value. The preceding convolution masks would return a value of zero. If we increase the center coefficients by one, each would return the original grey level. Therefore, if we are only interested in edge information that is in the original image, the coefficients should sum to a number greater than zero. The larger this sum, the less the processed image is changed

from the original image. Consider an extreme example in which the center coefficient is very large compared with the other coefficients in the mask. The resulting pixel value will depend most heavily upon the current value, with only minimal contribution from the surrounding pixel values.

3.3.2.3 High pass filter

Sharpening an image is based on the high pass filter. A high pass filter will remove the low frequency components (like the image's mean) and show only the details of the high frequency features. A common high pass filter mask is

$$\begin{array}{ccc} -\frac{1}{9} & -\frac{1}{9} & -\frac{1}{9} \\ -\frac{1}{9} & \frac{8}{9} & -\frac{1}{9} \\ -\frac{1}{9} & -\frac{1}{9} & -\frac{1}{9} \end{array}$$

Another method of high pass filtering is to subtract a low pass filtered image from its original. This is known as unsharp masking. Another method for sharpening is high-boost filtering. A high-boost filtered image may be computed by increasing the intensity of the original and subtracting a low pass image. The equation is

$$\text{High-Boost} = \alpha \text{ Original} - \text{Lowpass}$$

when $\alpha=1$, the result is a high pass filter. When $\alpha > 1$, a fraction of the original is added back to the high pass result. This has the effect of restoring some of the low frequency components. The mask is:

$$\begin{array}{ccc} -\frac{1}{9} & -\frac{1}{9} & -\frac{1}{9} \\ -\frac{1}{9} & \frac{w}{9} & -\frac{1}{9} \\ -\frac{1}{9} & -\frac{1}{9} & -\frac{1}{9} \end{array} \quad \text{where } w = 9\alpha - 1$$

Since high-pass filters enhance fine details in an image, they tend to amplify the noise in an image. This is seen in the output of high pass-based filters.

3.3.3 Thresholding

The final edge map is generated after thresholding the resultant image obtained by applying some edge operator. Thresholding refers to assigning all the pixel values below a certain level to '0' and all the grey level values above the certain level to '255' and that certain level is called as threshold value. Therefore, after thresholding a binary image is generated which contains only two pixel values '0' and '255'. Pixels with grey value 255 indicate an edge pixel. Thresholding will screen out all the unwanted variations in the edge image. Selection of a proper threshold value is a critical part. If we select a very high threshold value then it may cause the removal of most of the edges in the image. On the other side, if a low value is selected as threshold value, many spurious and unwanted edges will also be included in the final edge map. Therefore, an automated threshold selection is desirable than selecting a threshold value arbitrarily.

Considerable literature is available for the selection of automatic Threshold values (Otsu, 1979). Majority of threshold detection methods use image histogram to optimise a certain criterion function. For a bimodal histogram, the threshold value may be taken at its valley bottom. In many cases, a single global threshold value may not give good results over the entire image. In order to overcome this problem, the image is divided into several parts and in each part threshold selection technique is applied. The final threshold value is nothing but the mode of the threshold values of all parts of the image.

3.3.3.1 Otsu Thresholding Technique

Image thresholding is typically used with edge detectors to emphasize the edges. This emphasizes the strong edges and de-emphasizes the weak edges. Thresholding can use one or two levels. Images can use one threshold value to set those above the threshold to the maximum pixel value and those below the threshold to 0. An upper and lower threshold can also be used to alter pixel values. Values below the lowest threshold are set to 0. Those between the thresholds are left alone. Those above the upper threshold are set to 255. Thresholding technique is one that divides the image into two classes- background and objects. A survey on variety of thresholding techniques including both global and local thresholding was conducted by Sahoo et al. (1988). This section briefly explains a technique proposed by Otsu (1979) that has been used for the present work.

Let N be the set total number of pixels, (x, y) be the spatial coordinates of the image, and $G = \{0, 1, \dots, L-1\}$ be a set of positive integers representing grey levels. Then an image

can be defined as a mapping function $f: N \times N \rightarrow G$. The grey level value of a pixel with coordinates (x, y) is denoted as $f(x, y)$. Let $t \in G$ be a threshold value and $B = \{b_0, b_1\}$ be a pair of binary grey levels and $b_0, b_1 \in G$. The result of thresholding an image function at grey level t is a binary image function $f_1: N \times N \rightarrow B$, such that

$$f_1(x, y) = \begin{cases} b_0 & \text{if } f(x, y) < t \\ b_1 & \text{if } f(x, y) \geq t \end{cases} \quad (3.26)$$

In general, a thresholding method is one that determines the value t^* of t based on a certain criteria. If t^* is determined solely from the grey level of each pixel, then the thresholding method is point-dependent. If t^* is determined from the local property (for example, local grey level distribution) in the neighbourhood of each pixel, then the thresholding technique is one that divides a given image into subimages and determines a threshold for each of these subimages. The Otsu thresholding method is described below (Otsu, 1979)

Let the number of pixels with grey level i be n_i . Then the total number of pixels in the given image is

$$N = \sum_{i=0}^{L-1} n_i \quad (3.27)$$

The probability of occurrence of grey level i is defined as

$$p_i = \frac{n_i}{N} \quad (3.28)$$

$$\text{where } p_i \geq 0 \text{ and } \sum_{i=0}^{L-1} p_i = 1$$

One has to divide the number of pixels of an image into two classes C_0 and C_1 (background and objects) by a threshold at grey level t such that $C_0 = \{0, 1, 2, \dots, t\}$ and $C_1 = \{t+1, t+2, \dots, L-1\}$. Let σ_W^2 , σ_B^2 , and σ_T^2 be the within class variance, between-class variance, and total variance, respectively. An optimal threshold can be obtained by maximising one of the following conditions with respect to t :

$$\lambda = \frac{\sigma_B^2}{\sigma_W^2}, \quad (3.28a)$$

$$\eta = \frac{\sigma_B^2}{\sigma_T^2}, \quad (3.28b)$$

$$\kappa = \frac{\sigma_T^2}{\sigma_W^2} \quad (3.28c)$$

where,

$$\sigma_W^2 = \omega_0 \sigma_0^2 + \omega_1 \sigma_1^2 \quad (3.29)$$

$$\begin{aligned} \sigma_B^2 &= \omega_0 (\mu_0 - \mu_T)^2 + \omega_1 (\mu_1 - \mu_T)^2 \\ &= \omega_0 \omega_1 (\mu_1 - \mu_0)^2 \end{aligned} \quad (3.30)$$

$$\sigma_T^2 = \sum_{i=0}^{L-1} (i - \mu_T)^2 p_i \quad (3.31)$$

$$\sigma_0^2 = \sum_{i=0}^t (i - \mu_0)^2 \frac{p_i}{\omega_0} \quad (3.32)$$

$$\sigma_1^2 = \sum_{i=t+1}^{L-1} (i - \mu_1)^2 \frac{p_i}{\omega_1} \quad (3.33)$$

$$\omega_0 = \sum_{i=0}^t p_i \quad (3.34)$$

$$\omega_1 = \sum_{i=t+1}^{L-1} p_i = 1 - \omega_0 \quad (3.35)$$

$$\mu_0 = \frac{\sum_{i=0}^t i p_i}{\omega_0} \quad (3.36)$$

$$\mu_1 = \frac{\sum_{i=t+1}^{L-1} ip_i}{\omega_1} \quad (3.37)$$

$$\mu_T = \sum_{i=0}^{L-1} ip_i \quad (3.38)$$

It can be noticed from Equations (3.70), (3.71) and (3.72) that σ_W^2 and σ_B^2 are functions of threshold level t , but are independent of t . It is also noticed that σ_W^2 based on second order statistics (class variance) and σ_B^2 is based on first order statistics (class means). Therefore, η is the simplest measure with respect to t and hence chosen as the criterion to evaluate optimal threshold at level t . Thus, optimal threshold t^* is given below:

$$t^* = \max_{t \in G} \eta \quad (3.39)$$

3.4 RESISTIVITY METHOD

3.4.1 General

Of all the geophysical surveys, the electrical-resistivity method is employed for determining the electrical resistivity of the formation and also has found maximum applications in civil engineering problems. Electrical surveys are extensively used in civil engineering for determination the depth of bedrock, weathered zone thickness, groundwater occurrences etc. Electrical-resistivity surveys are easy to operate in the field with low expenditure. Electrical prospecting makes use of a variety of techniques, which include electrical resistivity, electromagnetic, induced polarization, telluric currents and magnetotelluric methods. The electrical-resistivity method is extensively used for groundwater, explorations.

3.2.4 ELECTRICAL RESISTIVITY METHOD:

Resistivity is defined as the resistance between opposite faces of a unit cube of the material. If a material of resistance 'R' has a cross-sectional area A and length L, the resistivity can be expressed as

$$\rho = \frac{RA}{L} \text{ expressed in ohm-m} \quad (3.40)$$

The electrical resistivity of the geological formation depends mostly on porosity, salinity and water content. All the rocks and soils transmit current due to the water content in void spaces. The resistivity of geological formation can be represented by the relation.

$$\rho_f = \rho_w / F_s F_s \quad (3.41)$$

where ρ_f = resistivity of the formation

ρ_w = resistivity of the water content in the formation ;

F_s = Formation factor depending on porosity

R_s = Resistivity depending on degree of saturation

Hence the measurement of resistivity will be given as an indication of the presence of water and its salinity. In an electrical-resistivity survey, a known current I is sent into the ground through a pair of current electrodes C_1 and C_2 and the potential difference (V) created in the medium between a pair of potential electrodes P_1 and P_2 is measured. Hence, the resistivity of the formation based on Ohm's law is stated by

$$\rho = K \frac{V}{I} \quad (3.42)$$

where K is termed geometric factor of the electrode arrangement

$$K = \frac{2\pi}{\frac{1}{C_1 P_1} - \frac{1}{P_1 C_2} - \frac{1}{C_1 P_2} - \frac{1}{C_2 P_2}} \quad (3.43)$$

$C_1 P_1$, $P_1 C_2$, $C_1 P_2$ and $C_2 P_2$ are distances between the designated electrodes; ρ is the resistivity of the formation. However, the latter depends on the nature of the formation. If the formation is isotropic and homogeneous, the resistivity of the formation is measured. If the formation is anisotropic, apparent resistivity is measured. The apparent resistivity value depends on several variables, such as electrode spacings, geometry of the electrode array, true resistivity and geological factors. The effective depth of current

penetration increases with an increase in electrode spacings. Various types of electrode configuration may be employed but Wenner and Schlumberger configurations are used more extensively for geotechnical and groundwater investigations.

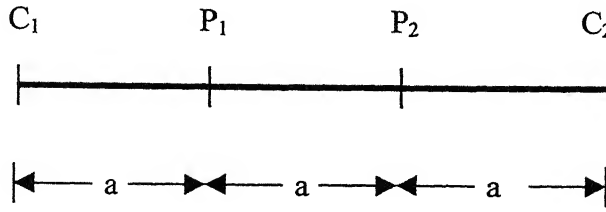


Figure 3.2 Wenner configuration

(a) Wenner Configuration:

The potential electrodes P₁ and P₂ are placed in a line with current electrodes C₁ and C₂. All are placed equi-distant from each other and disposed symmetrically with respect to a central point of investigation. A Wenner configuration is shown in Figure 3.2.

$$\rho_a = 2\pi a \frac{\Delta V}{I} \quad (3.44)$$

where “a” is the distance between the adjacent electrodes, “I” is the applied current and “V” is the voltage difference between the potential electrodes.

(b) Schlumberger Configuration:

In this configuration all the four electrodes are placed in a line but the distance between the current electrodes C₁, C₂ is maintained equal to or more than five times the distance between the potential electrodes. A Schlumberger configuration is shown in Figure 3.4.

The apparent resistivity is calculated by:

$$\rho_a = 2\pi \frac{(L^2 - a^2) \Delta V}{4a I} \quad (3.45)$$

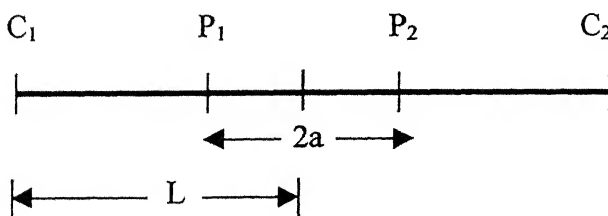


Figure 3.4 Schlumberger configuration

The depth of investigation in an isotropic and homogeneous formation is equal to half the distance between current electrodes.

3.4.3 Field Procedure

The resistivity surveys conducted in the field are mainly of two types: D.C. resistivity meter and A.C. resistivity meter. D.C. resistivity meter uses an external power supply, which can be increased to about 500 V and are capable of sending up to 2 amperes. A.C. Instruments use a low-frequency alternating current source.

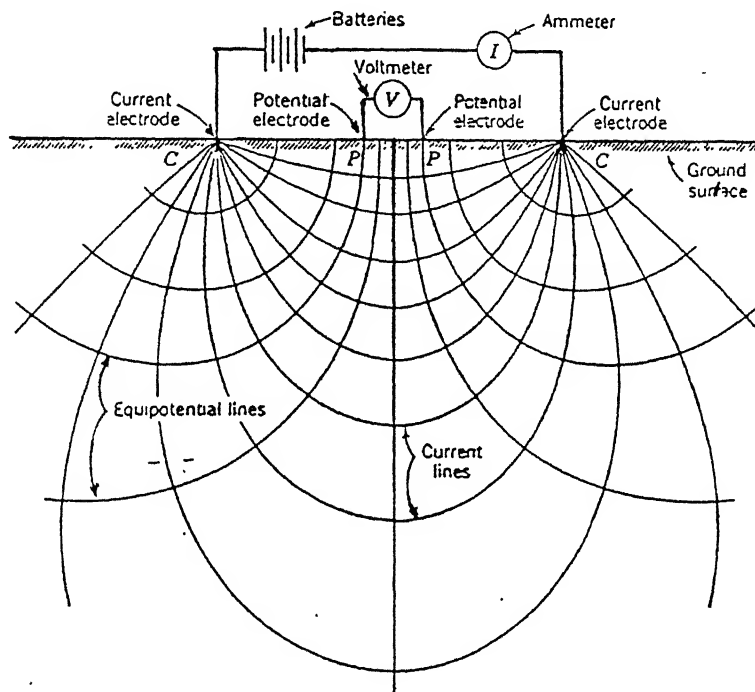


Figure 3.5 Resistivity array

Resistivity is measured by using four electrodes set in the ground. Current is applied to the ground through two of these electrodes and the resultant potential drop across the other two potential electrodes is noted as shown in Figure 3.5. Non-polarising copper sulphate porous pots are employed as potential electrodes to avoid various potentials developing between electrodes and electrolytes in the earth. A number of observations can be made by changing electrodes. The apparent resistivity is calculated from the known value of current (I) and the potential difference and the electrode spacings. The Wenner and Schlumberger methods are applied in the field. Field data is plotted on log-log graph sheet and the resultant field curve used for the interpretation.

3.4.4 Resistivity Profiling

There are two types of resistivity surveys, namely, profiling or lateral traversing and vertical electrical sounding (VES) or depth investigation. In a profiling survey, horizontal anomalies are delineated whereas in soundings vertical anomalies of the formation are investigated.

(a) Resistivity profiling

In this survey, electrode spacings are fixed; apparent resistivity values are determined at specified stations by shifting the whole electrode array along a particular profile or in a grid pattern. By measuring the apparent resistivity along the same profile with different electrode spacings and lateral as well as vertical changes in apparent resistivity can be obtained.

Resistivity data collected during profiling is plotted against the corresponding stations along the profiles to depict an apparent-resistivity variations. If the readings are taken in grid pattern with one electrode spacings, the data may be utilised to prepare a contour map of apparent resistivity for the particular electrode spacings (Reddy, 1995)

(b) Vertical electrical sounding

In this method, keeping the place of observation constant, a set of apparent resistivity values are obtained successively for different electrode spacings. The value of apparent resistivity is plotted as a function of electrode spacings on log-log paper. The field curves may be grouped into two layers, three layers and four layers. The three-layer curves are represented as A, H, K and Q types. In A type $\rho_1 < \rho_2 < \rho_3$, H type $\rho_1 > \rho_2 < \rho_3$, K type $\rho_1 < \rho_2 > \rho_3$, and Q type $\rho_1 > \rho_2 > \rho_3$. These curves are shown in (Figure 3.6).

3.4.5 Interpretation

The interpretation of resistivity data is carried out mainly in two stages. In the first stage the data is interpreted in terms of physical parameters, depth and resistivity. In the second stage interpreted results are correlated with geological knowledge to confirm the subsurface features. The popular method among interpretation techniques is curve matching. In this method the field curve is drawn on the same scale as the master curves to match with the master curves. In this study the interpretation has been carried out by

using Resix standard resistivity package, which is based on the above idea. According to Reddy (1995), interpretation of three-layer curves is done as follows:

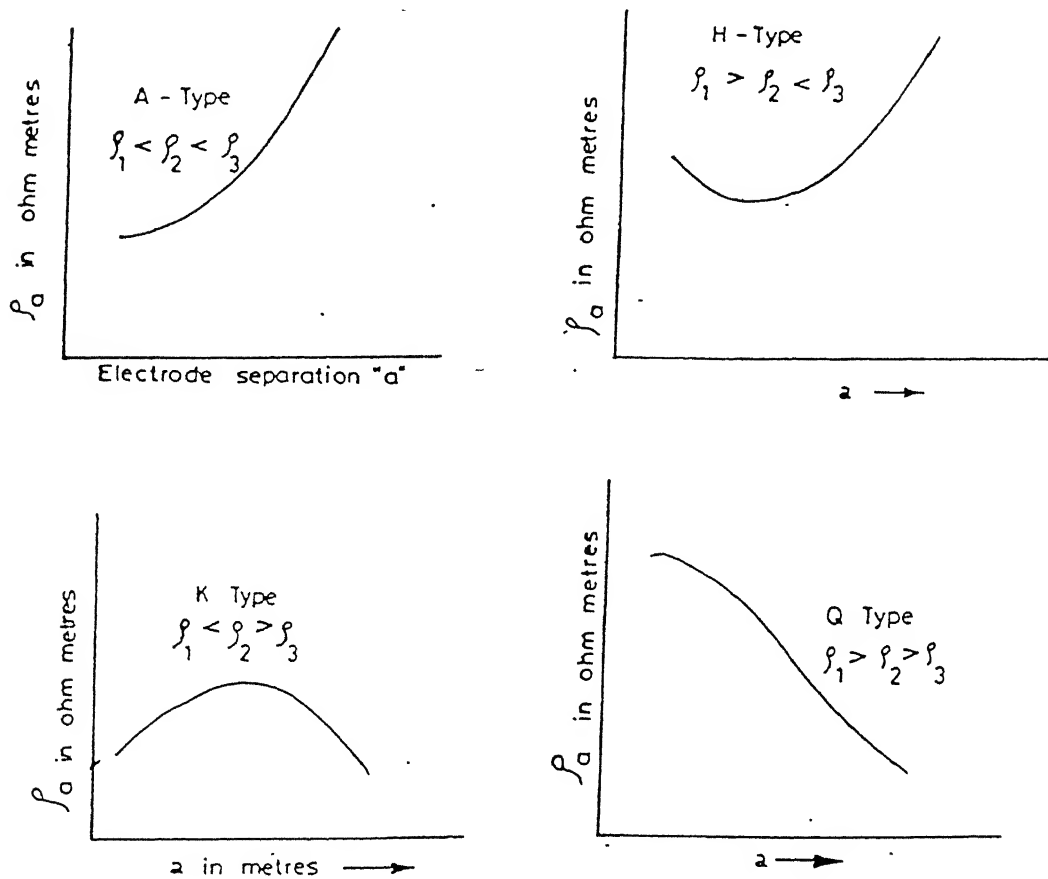


Figure 3.6 showing the master curves for interpretation (after Reddy, 1995)

1. Select the three-layer master curve sheet(s), which exhibits the same general shape as the field curve (A, K, H or Q). The master curves of each type are grouped into families having different resistivity ratio combinations ($\rho_1:\rho_2:\rho_3$). The family of curves contains one curve for each h_2/h_1 ratio.
2. Select the three-layer master curve sheet(s), which exhibits the same general shape as the field curve (A, K, H or Q). The master curves of each type are grouped into families having different resistivity ratio combinations ($\rho_1:\rho_2:\rho_3$). The family of curves contains one curve for each h_2/h_1 ratio.

3. Superimpose the transparent paper containing the field curve on the master curve sheet and by moving the sheets one with respect to the other (keeping areas parallel) to obtain a close match with one of the master curves. If an exact match is not obtained, interpolation between curves is made.
4. Trace on the transparent paper the cross of the master curve together with the two resistivity marks ρ_1 , ρ_3 and also the number which identifies the particular master curve (thickness ratio number).
5. The thickness of the first layer will be equal to the cross abscissa on the field curve. The thickness of the second layer will be equal to the thickness ratio number multiplied by the thickness of the first layer: depth to the top of the third layer will be equal to the sum of the thickness (first layer and second layer).
6. The resistivity of the first layer will be equal to the cross coordinate on the field graph. The resistivity of the second layer will be equal to the coordinate to read on the field graph corresponding to the position of the ρ_2 resistivity mark. Similarly, the resistivity of the third layer corresponds to the ρ_3 resistivity mark. The interpretation procedure is shown in Figure 3.7. A perfect match is rarely obtained; interpolation between master curves gives satisfactory result. After comparing the field curves with standard curves formation parameters (thickness, resistivity, and number of layer) are obtained. Vertical electrical soundings are used for groundwater investigation and bedrock delineation. However, these surveys are also used for mineral exploration and toxic waste studies.

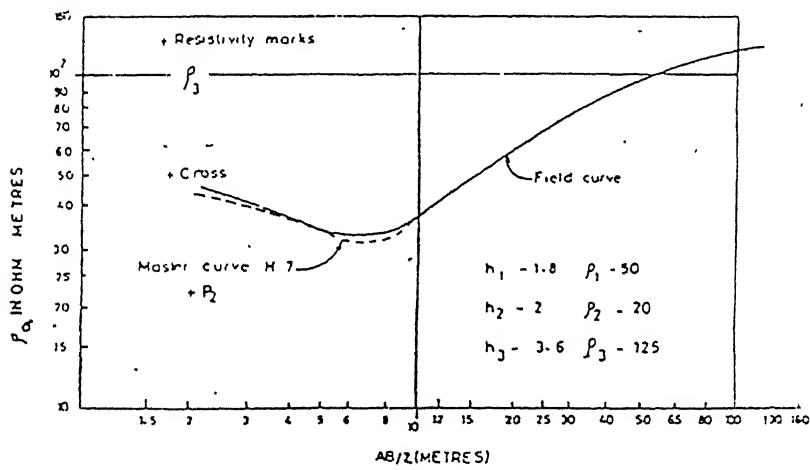
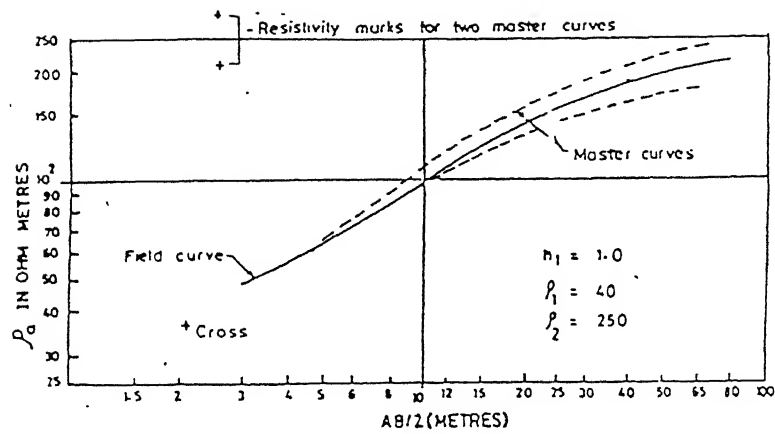


Figure 3.7 the interpretation procedure (after Reddy, 1995)

Chapter IV

RESULTS AND DISCUSSION

4.1 GENERAL

This chapter discusses the analysis of remote sensing data and resistivity data with special reference to deduce subsurface features. The remote sensing and resistivity data show very good correlation in studying the subsurface features. Efforts have been made to IRS-1C LISS-III to improve to the visual interpretation and to understand the effect of data merging on thresholding technique for geological applications.

4.2 METHODOLOGY

For the mapping of surface features, we have used remote sensing data and for subsurface mapping resistivity soundings have been carried out. The approach followed in the present study is shown in Figure 4.1:

4.2.1 Image processing:

The following steps have been carried out through this study:

1. Generating false colour composite (FCC) using blue, green, and red bands.
2. Generating Normalized Vegetation Index (NDVI), and reclassification of image based on NDVI values.
3. Extraction of geomorphological features from stretching FCC.
4. Applying edge detection operators (Sobel, Laplacian, High pass, and Otsu thresholding technique) on green and red bands.
5. Registering of multi-spectral images to Pan characteristics using Idrisi package.
6. Merging of the registered images using the HPF and Price algorithm, IHS, and P+XS methods.
7. Final image showing fault location.

4.2.2 Resistivity soundings: Resistivity soundings at 14 locations have been carried out. Following steps have been followed to deduce subsurface resistivity information:

1. We have calculated the apparent resistivity using $\rho = K \frac{V}{I}$; while:

$$K = \frac{2\pi}{1/CP_1 - 1/PC_2 - 1/CP_2 - 1/C_2P_2}$$

Where C and P are positions of current and potential electrodes, respectively as discussed in Chapter III.

2. Analysis of resistivity data using Resix package.

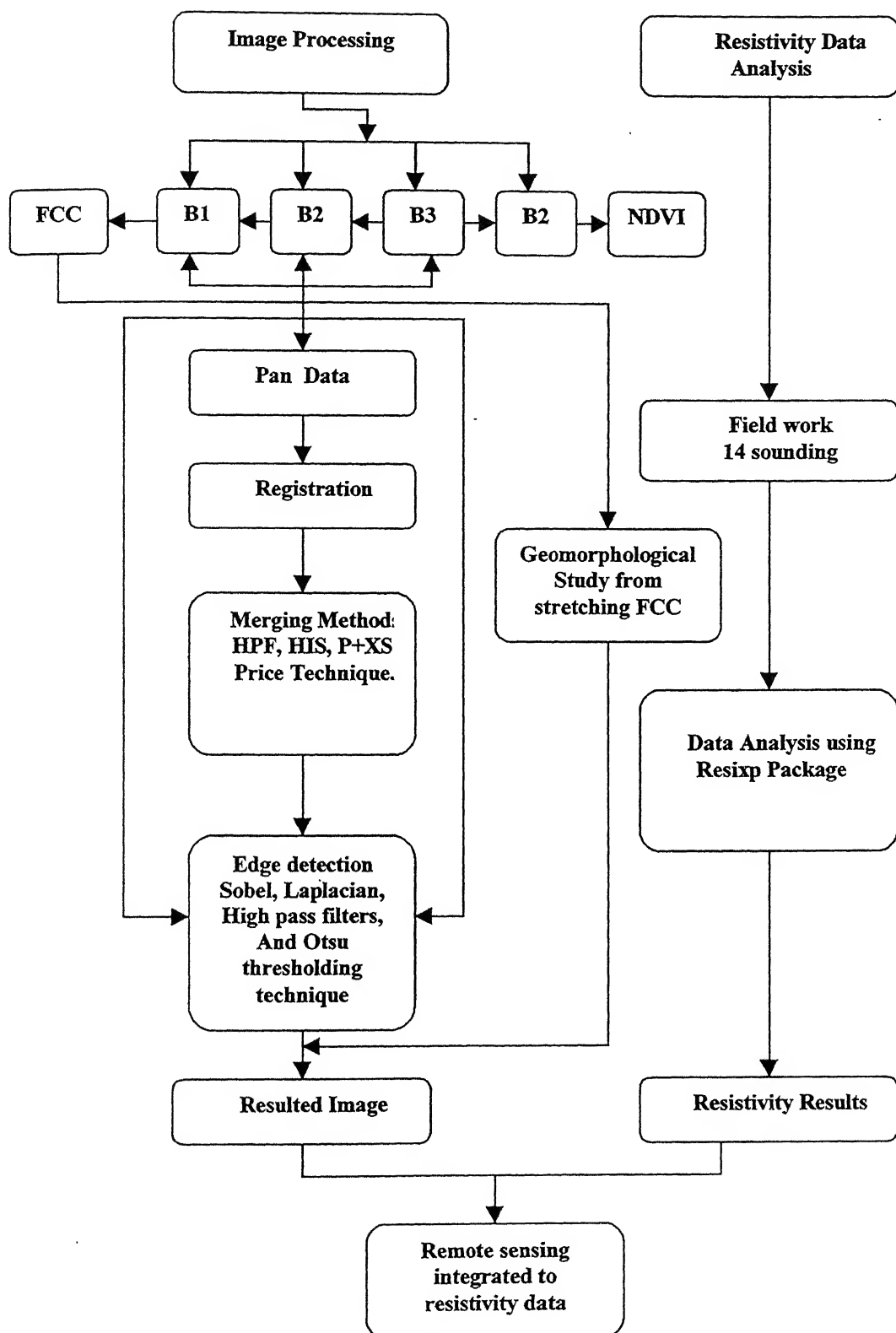


Figure 4.1 shows the methodology followed in present study

4.3 Digital image processing:

Detailed processing of digital remote sensing data have been carried out to deduce surface features.

4.3.1 False Colour Composite (FCC):

Using multi-spectral bands from IRS-1C LISS-III, NIR, green, and red bands, the FCC image has been generated (Figure 4.2). IRS-1C LISS-III false colour composite image shows a channel migration pattern through neck cut-off spread over an area about 150 Km² along the Ganga river in the (Bithoor) Kanpur region. FCC shows different areas representing agriculture, urban areas, and geomorphological features like prominent meander cut-off, Ox-bow lake, and successive of paleo-channels.



Figure 4.2 FCC false colour composite of the study area

4.3.2 Geomorphological studies:

From stretching of FCC (Figure 4.3), we have generated geomorphological map (Figure 4.4) of the study area. Geomorphological studies have been carried out, which indicate that the Ganga river has reached its present location through 6 steps, in the first step the Ganga river was flowing at the eastern side of the Unnao city. Then started its migration in western direction to flow at west of Unnao, this has happened in second

step. In the third stage the northern main channel has shifted to the left and has created a loop channel. In the fourth step, the Ganga river has migrated towards eastern direction may be due to subsurface movement and started its westward movement which lead to meander cut-off in the fifth step. At the last step, river changes its main channel to present course. Inside meander cut-off, the image clearly show the presence of two distinct geomorphic zones, in the western zone older formation of flood plain characterised by modified or overlapping paleo-channels. The eastern part characterised by development of meander scars, sloughs, and lakes. In this zone younger deposition is found compared to the western part. It is clearly seen from the image that the geomorphological features like paleo-channels show discontinuity and change their direction. The change in direction of these paleo-channels reflects the upward and horizontal movements of the subsurface.

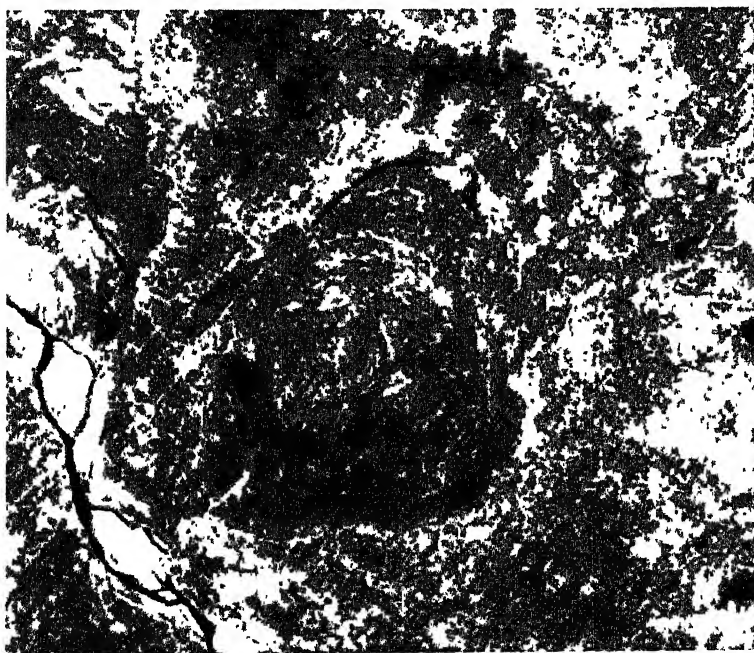


Figure 4.3 stretching FCC.

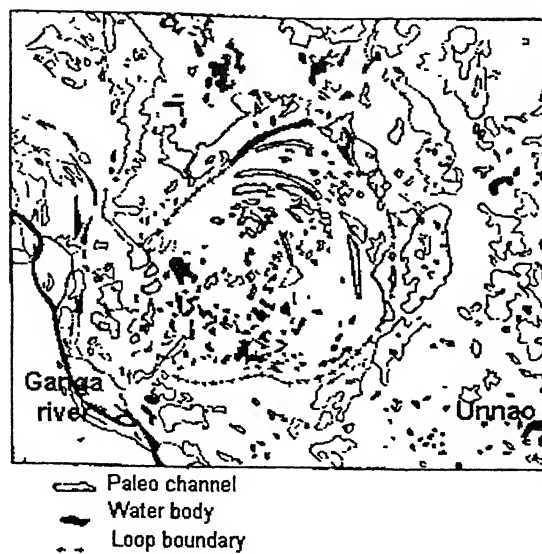


Figure 4.4 Geomorphological map produced from FCC.

4.3.3 NDVI Normalized Vegetation Index:

Using NIR and Red bands, we have computed NDVI using the following formula:

$$NDVI = \frac{\text{Band4(NIR)} - \text{Band3(Red)}}{\text{Band3} + \text{Band4}}$$

NDVI image is shown in Figure 4.5. This NDVI image is further classified in seven classes representing water body, very poor, poor, moderately, high, very high vegetated areas, and tree with 2 meter height. Classified image is shown in (Figure 4.6).

Table 4.1 NDVI values for different classes

	NDVI Values range	Vegetation condition
Class I	-0.362 - 0	Water
Class II	0 - 0.196	Very poor
Class III	0.196 - 0.296	Poor
Class IV	0.296 - 0.396	Moderately
Class V	0.396 - 0.496	High
Class VI	0.496 - 0.596	Very high
Class VII	0.596 - 0.696	Tree with 2 meter height

The normalised difference vegetation index (NDVI) values show that the study area can be classified in two distinct vegetated zones: western zone is highly vegetated than the eastern part, which shows negative values for NDVI due the presence of water, and poorly vegetated. The highly vegetated areas are related to paleo-channels.

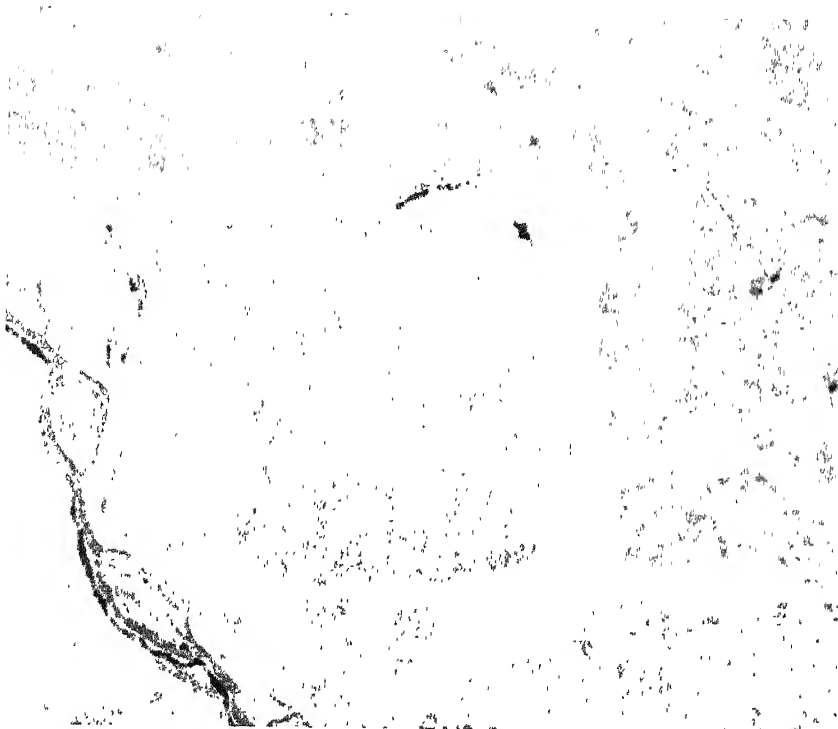


Figure 4.5 NDVI produced using Band 3 and Band 4

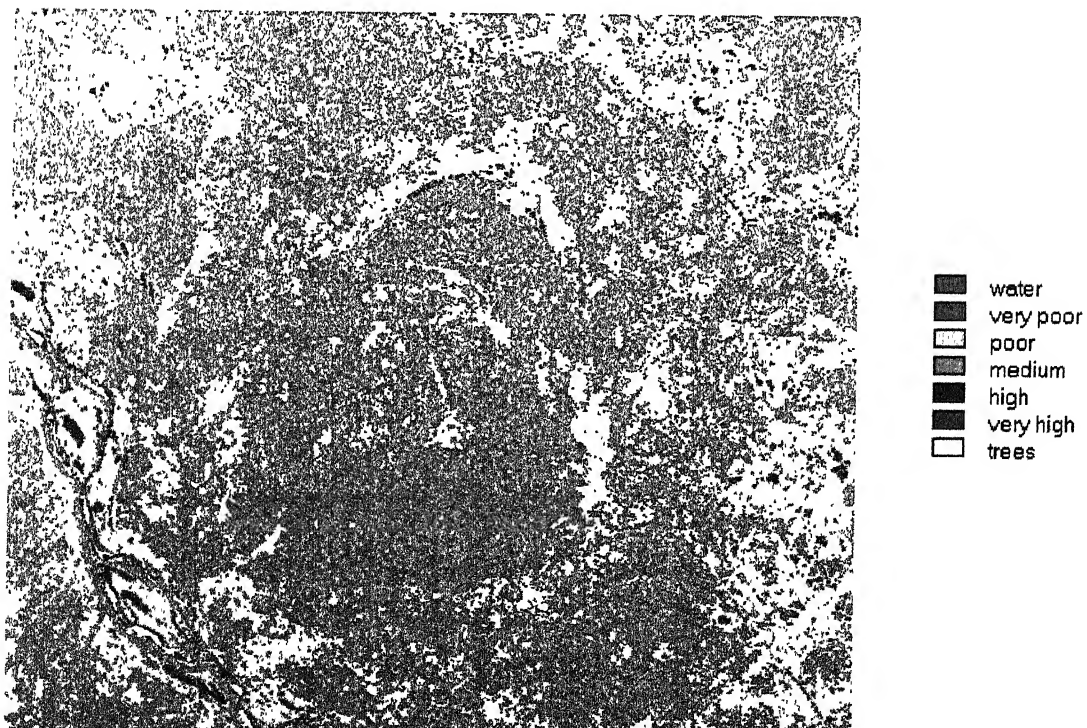


Figure 4.6 Classified image based on NDVI values

4.3.4 Edge detection:

One of the main objectives of the present work is to know the effect of merging on edge detection. To compare the results, edge extraction procedure involves two major steps on both the original and merged data. Band 2, which is found to suited more to extract geological features compared to Band 3, which shows more number of linear features. Band 2 is used for extracting edges of lithological contrast in both cases before merging and after merging. These images are shown in Plates 4.1 to 4.6 for IRS-1C Bands 2 and 3. For the extraction of the edges following steps have been followed:

(a) Edge detection

1. Use of Laplacian, second order derivative operator on Band 2 image to compare with Sobel operator image. The output images are shown in Plate 4.1 which shows that Laplacian operator is unable to give good details in studying edges which are related to lithological contrast as given by Sobel operator.
2. The Sobel non-linear operator, which is considered as one of the best available operators, has been used to extract the edges from the image. The output images have been generated (Plate 4.2) using absolute gradient values.
3. Use of High passes filter to remove the low frequency components. The high frequency features are shown in Plate 4.3.

(b) Thresholding

The Otsu technique has been used to find the optimal threshold value. The image is divided into 16 different equal parts. Otsu technique is applied to Bands 2 and 3 before merging and after merging. The global threshold value obtained as the mode of threshold values for all parts in the image. Finally, the global threshold values one for each band in two cases have been obtained. Using this threshold value the image has been converted into binary form by assigning the pixels value less than the threshold value to '0' and pixels with grey value greater than the threshold value to '255'. Otsu thresholding technique has been applied on Bands 1 and 2 before and after applying merging techniques using only HPF, and Price methods. Otsu thresholding technique has given the ability to map the fault locations and to recognize the high and low land areas. Different values of thresholding might be useful in numerous geological applications. Table 4.2 shows the optimal thresholding values for the two cases.

Table 4.2 Otsu threshold value for IRS-1C Band 1 and
Band 2 using 16 image parts

Multi-spectral bands	Before merging	After merging	
	Thresholding values	HPF	Price
		Thresholding values	Thresholding values
Band 2	37	16	18
Band 3	48	18	26

From the optimal threshold values, it is clearly seen that merging technique has filtered the noise due to which more details have appeared in the output images. It has been found that the use of Otsu thresholding method to a merged data has not given better results compared to the original data. Applying Otsu technique on Band 2 we have found better geological features and clear image with more information about the area compared to those of Band 3 (Plates 4.3 to 4.6).

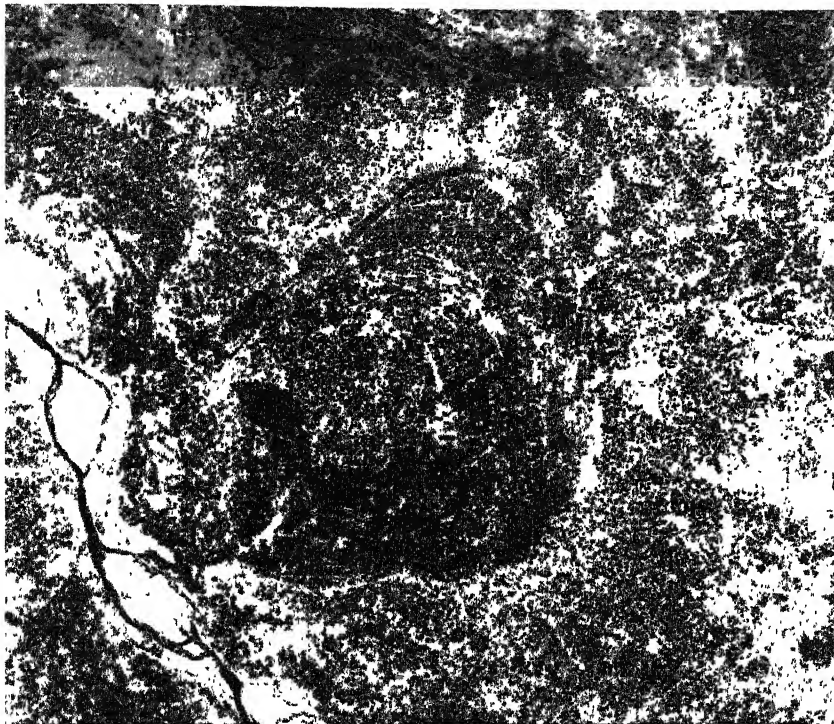
4.3.5 Merging Technique

After registration, IRS-1C LISS-III multi-spectral images to the PAN data, different merging algorithms *i.e.* IHS, P+XS, HPF and Price have been applied. The main aim of the merging techniques is to introduce the spatial information of the high spatial resolution PAN image to the low spatial resolution images and IRS-1C LISS-III data without distorting the spectral characteristics of the higher spectral resolution bands and IRS-1C LISS-II data. In the present study, the merging of IRS-1C LISS-III with PAN data has been carried out.

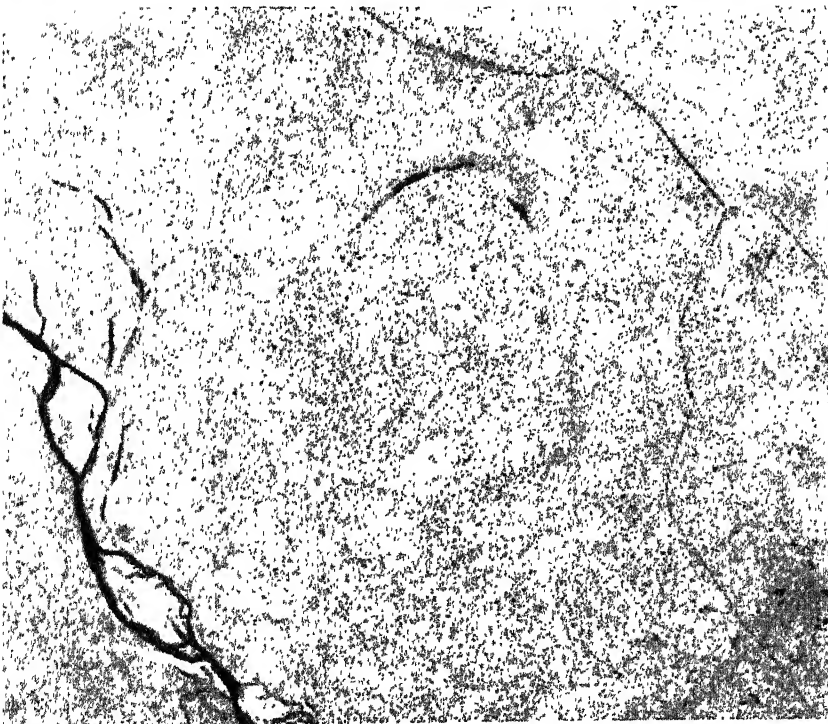
The following discussions briefly explain different input and output data used in various merging algorithms.

(a) IHS

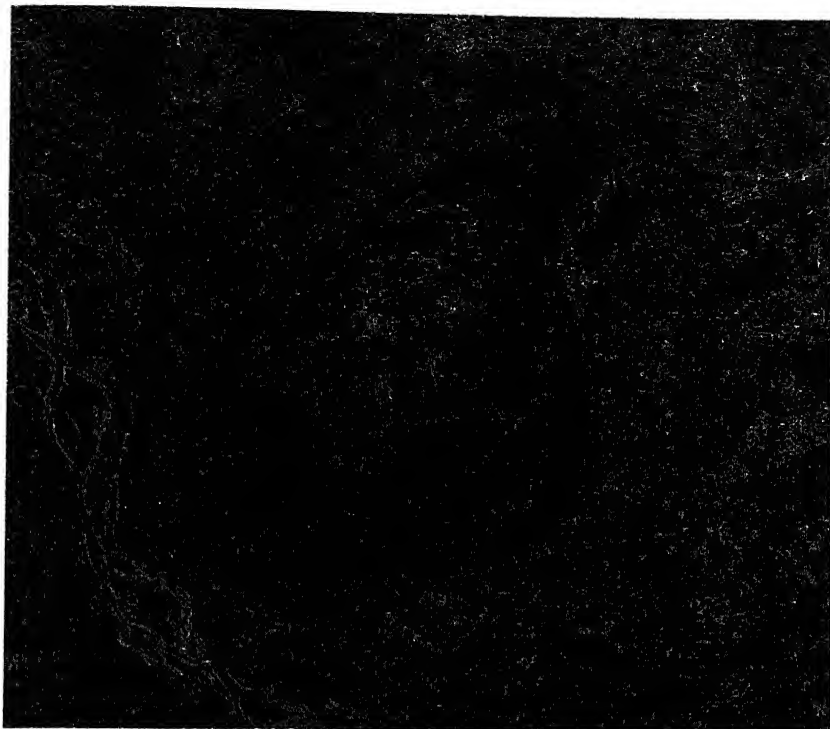
In this algorithm, only three images can be merged at a time. The registered multi-spectral Bands 1 to 3 are merged with PAN data. The registered low-resolution images are transformed from RGB space to IHS space. Before taking inverse transform, the intensity component is replaced with the PAN data. The main assumption for replacing the intensity component with the high-resolution data is that the two images are approximately equal to each other spectrally. The merged images are shown in Plates 4.7 and 4.8.



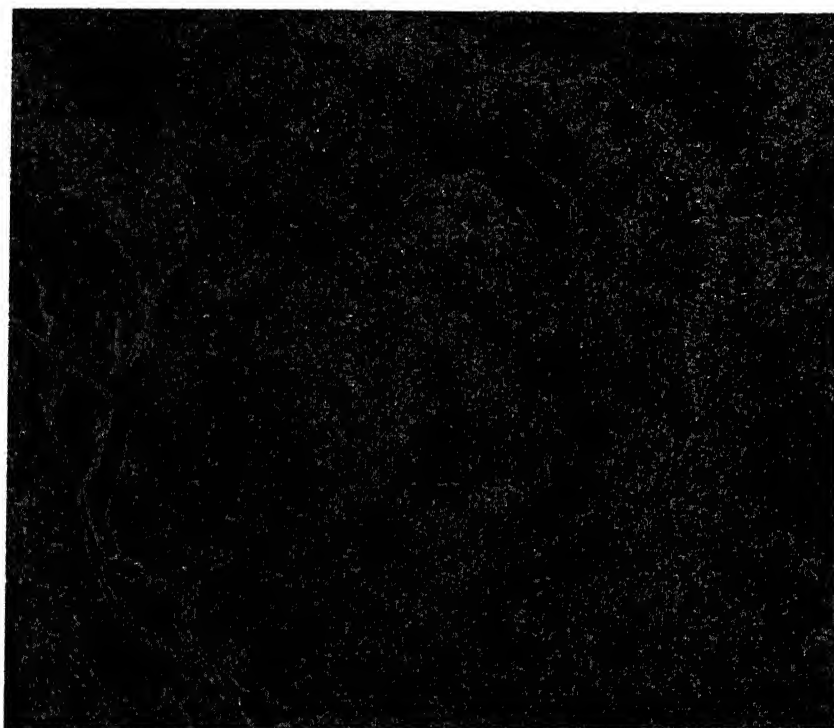
Laplacian edge operator applied on Band 2



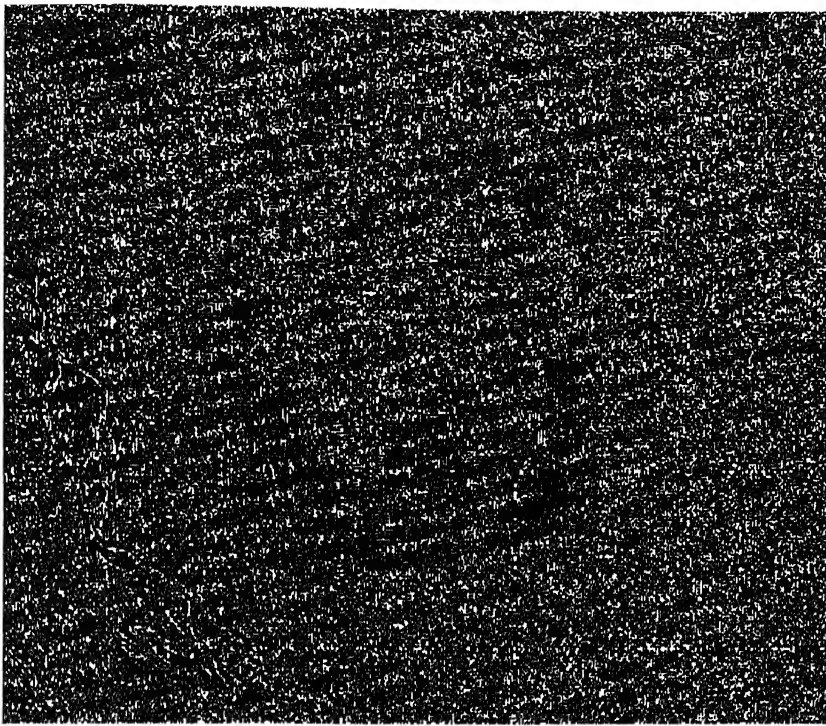
Laplacian edge operator applied on Band 3



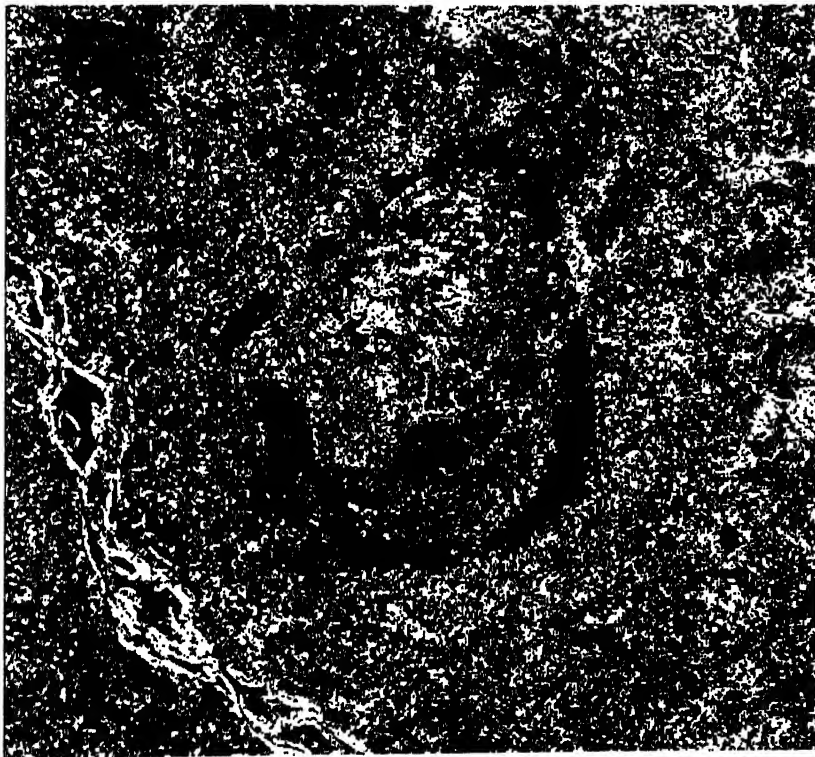
Sobel edge operator applied on Band 2



Sobel edge operator applied on Band 3



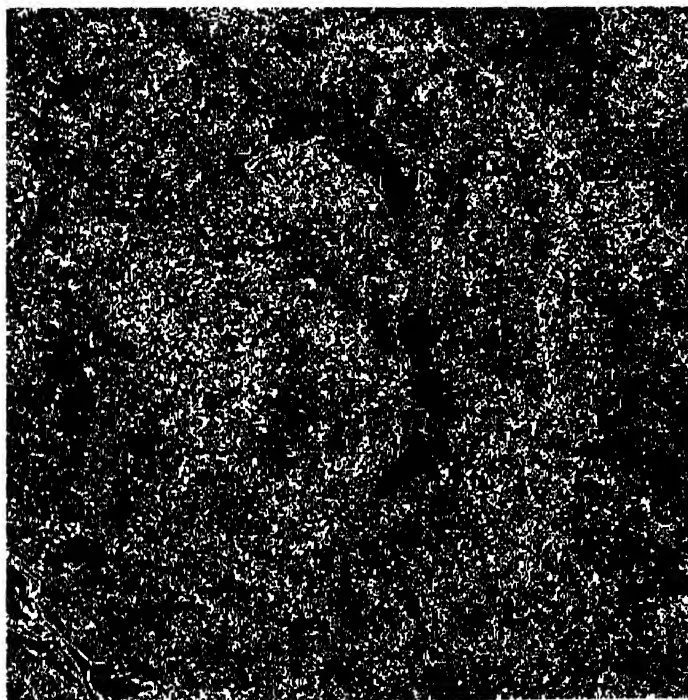
High pass filter applied on Band 2



Otsu thresholding applied on Band 2 before merging
using optimal value equal to 40



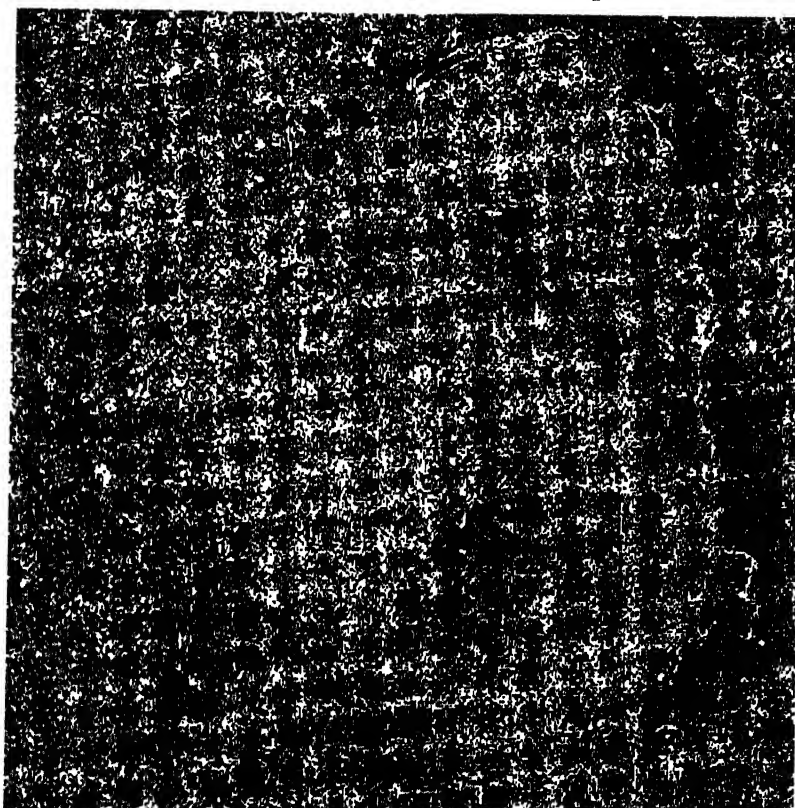
Otsu thresholding applied on Band 2 before merging
using optimal value equal to 37



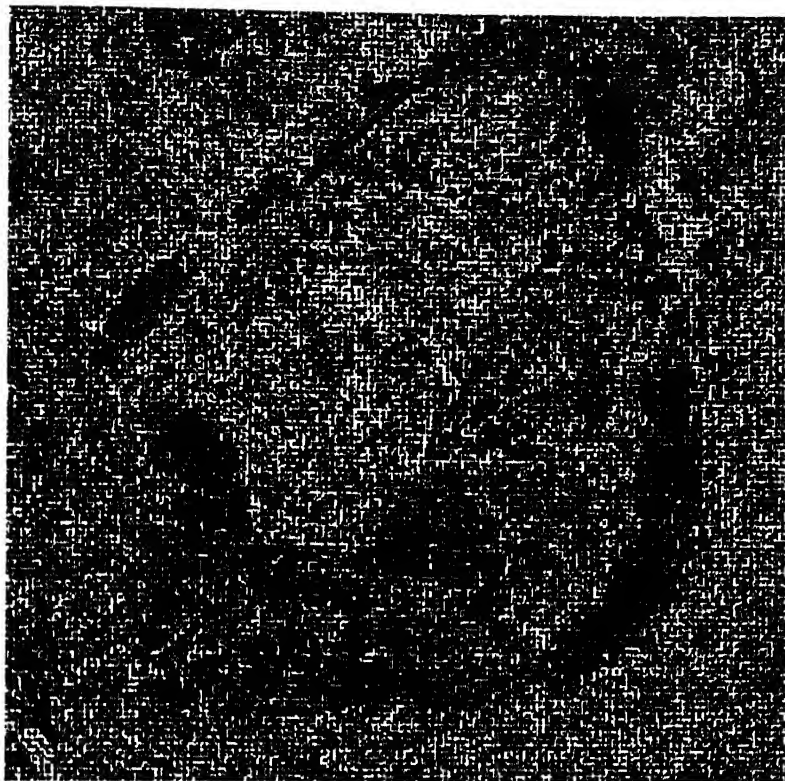
Otsu thresholding applied on Band 3 before merging
using optimal value equal to 48



Otsu thresholding applied on merged Band 2 using HPF
merging method using optimal value equal to 16



Otsu thresholding applied on Band 3 using HPF technique
and optimal value equal to 18



Otsu thresholding applied on merged Band 2 using
Price method and optimal value equal to 18



Otsu thresholding applied on merged Band 3 using
Price method and optimal value equal to 26

(b) *P+XS*

In this method two images of Band 1 and Band 2 have been merged. Band 3 is same as before merging. This method is based on the assumption that Band P (Panchromatic) is the sum of the Bands 1 and 2. First multi-spectral images of Band 1 and Band 2 have been registered to Pan band. The output images are shown in Plates 4.8 and 4.9. Using equations 3.17 to 3.18 the resultant merged images have been generated.

(b) *HPF*

HPF (high pass filter) is applied to high spatial resolution data, and mean filter is applied on low resolution data and the results are added pixel by pixel. The size of the mean filter applied on the PAN data is approximately equal to the ratio of resolution of different satellite data used for merging. Hence, mean filters of size 3 x 3 is applied, respectively on PAN data and the resultant image is subtracted from the original image to extract the high frequency image. This is added pixel by pixel to each low-resolution slave image. The merged images are shown in Plates 4.10 and 4.11.

(d) *Price*

This method uses the original slave images and registered or without registered images. The Price algorithm is based on the correlation between high-resolution and low-resolution images. The correlation is determined between these images, PAN data is either averaged or registered to multi-spectral bands. The correlation values are given in Table 4.3. As there is a difference in the date of acquisition of the PAN, and multi-spectral images of IRS-1C LISS-III, experiments have been carried out using only PAN image registered to multi-spectral images using only nearest neighbour resampling techniques. There are two steps for merging with the Price algorithm based on the correlation coefficients. In step-1, the highly correlated slave images are used for merging. The step-2 is applied for weakly correlated slave images.

The first step of Price algorithm is used to merge Bands 1 and 2. The second is used to merge Band 3. In Table 4.3 the correlation coefficients values for Bands 1 and 2 are small because of different dates for Pan and multi-spectral images, while in Band 3 it is normal. Table 4.3 also shows that the use of registered Pan image gives better correlation coefficients values compared to the use of averaged Pan image. The merged images are shown in Plates 4.11 and 4.12.

Table 4.3 Correlation coefficients between PAN and Low Resolution images

<i>Low resolution images</i>	PAN_{avg}	$PAN_{reg} (NN)$
<i>Band 1</i>	0.1196	0.1886
<i>Band 2</i>	0.1286	0.1973
<i>Band 3</i>	0.0434	0.1263

PAN_{avg} - averaged PAN data

PAN_{reg} - registered PAN data

4.3.5.1 Results from Data Merging

Using four methods (HPF, Price, IHS, and P+XS) the visual comparison have been made between original and merged data. Using the above mentioned methods give the following important points:

- 1 All methods are found to improve the resolution as well as features present in the image.
- 2 Visually HPF and Price techniques have given better results compared to other methods.
- 3 Only HPF and price method have removed cloud cover from output merged images.

The root mean square errors (RMS) are the measure of the accuracy of the Ground Control Points (GCP) selected for registering the images. The RMS error is expressed in the input image units in the form of number of pixels which should be less than 3 pixels. The results obtained from the experimental studies are presented in Table 4.4. No significant effect of RMS values to merging results are seen from Table 4.4 because it is obtained equally for different merging methods and with considering different bands, except for Price method.

Table 4.4 Average RMS errors of GCP

<i>Bands</i>	<i>RMS errors used for HPF, IHS and P+XS</i>	<i>RMS used for Price</i>
<i>Band 1</i>	0.592	0.45
<i>Band 2</i>	0.592	0.45
<i>Band 3</i>	0.592	0.45

Statistical and numerical comparisons have been made to evaluate the effect of different data merging techniques on distortion of the spectral characteristics of higher spectral resolution data. The mean and standard deviations have been calculated before and after merging for different merging technique as well as for different bands. The mean and standard deviations values are given in Table 4.5.

Table 4.5 Mean and Standard deviation values of original and merged IRS-1C data.

<i>Band</i>	<i>Estimates</i>	<i>Original Data</i>	<i>Merging methods</i>			
			<i>Nearest neighbour</i>			
			<i>HPF</i>	<i>Price</i>	<i>IHS</i>	<i>P+XS</i>
<i>Band 1</i>	<i>Mean</i>	104.386	100.94	103.7	136.34	158.6
	<i>S.D.</i>	13.173	9.787	11.22	27.9	15.05
<i>Band 2</i>	<i>Mean</i>	67.856	65.82	87	132.4	109.05
	<i>S.D.</i>	13.672	10.894	9.482	29.11	20.87
<i>Band 3</i>	<i>Mean</i>	92.660	94.95	96.12	149.8	-
	<i>S.D.</i>	11.593	10.667	9.898	23.98	-

An absolute difference image between the merged and the original image is computed. The mean and standard deviation of the difference image indicates the distortions due to merging. Higher the value of these factors, more the distortions due to merging technique used. The number of zero pixels present in these (difference) images are also determined. Higher the number of zero pixels, lesser the distortion in the spectral values. The number of zero pixels has been calculated from difference images between original and merged data. Table 4.6 shows how the merged data differ from the original data numerically.

Table 4.6 Number of zero pixel values of merged IRS-1C data.

<i>Band</i>	<i>Merging methods</i>			
	<i>Nearest neighbor</i>			
	<i>HPF</i>	<i>Price</i>	<i>HIS</i>	<i>P+XS</i>
<i>No. of '0' pixels value % for Band 1</i>	40%	10%	2%	0%
<i>No. of '0' pixels value % for Band 2</i>	41%	6%	0%	Less than 1%
<i>No. of '0' pixels value % for Band 3</i>	38%	8%	Less than 1%	-

From Mean, Standard deviation, and Number of '0' pixel values, it has been found that the HPF method gives the best results with less distortion to spectral

characteristics. The number of '0' pixels obtained for different bands is around 40%, while from Price technique it is found around 9% only, this may be related because of the use of different date for Pan, and multi-spectral Bands. Generally, the other methods IHS, and P+XS methods give number of '0' pixels less than 1%. The mean and standard deviation values of the merged data from the HPF and Price algorithm are numerically very close to that of the original data. The mean and standard deviation values of data resulting from the IHS and P+XS methods are much deviated from the original values. Based on the numerical closeness of the mean and standard deviation values of the merged data to that of the original data, different merging techniques can be arranged in the descending order of preference as HPF, Price, IHS and P+XS.

Following points have been adopted while applying merging methods:

1. Both HPF and Price algorithm have given very good results but it is better to use HPF method if there is difference in time for data acquisition between Panchromatic and multi-spectral bands.
2. For regional geological investigation it is not necessary to use merging technique but for study the features from a specific region one must use merging techniques.
3. Use of Price and HPF methods remove the cloud cover from the merged data.
4. Use of merging techniques reduce the noise and give more details of an image which are shown from optimal Otsu thresholding values.
5. The applied merging techniques have not given any improvement for geological edge extraction the reason is related to scale and its effect on pixels from merged data.

4.3.6 Results from remote sensing data:

From the detailed remote sensing data analysis following results have been obtained.

1. The geomorphological features show the inside of meander cut-off image clearly showing the presence of two distinct geomorphic zones: the western zone is covered by older flood plain characterised by modified or overlapping paleo-channels. The presence of two distinguished areas may be related to major tectonic events.

2. The vegetation index (NDVI) shows two different areas, western zone with highly vegetation compared to other parts, which show negative values for NDVI due the presence of water, and poor vegetation.
3. Sobel edge operator also shows two distinct zones: western part with more edges compared to that of eastern part.
4. Otsu thresholding technique is found to show clearly the presence of lineaments representing faults in the area and also gives information about the presence of low land area in the eastern part and uplifted area in the western part.
5. Band 2 image clearly shows edge enhancement compared to Band 3 image, and also even after applying merging techniques. The edge operators on original data found to give better results compared to merged data.
6. Merging technique helps to understand the remaining edge of the channel migration due to presence of road not related to the presence of fault.
7. For studying subsurface structure, it might be useful to study topography variations through generating Digital Elevation Model (DEM) and draped image. In the present study due to unavailability of complete topography data it was not possible to use this approach and its relationship with subsurface structure.
8. The subsurface and surface features from remote sensing data are shown in Figure 4.7.

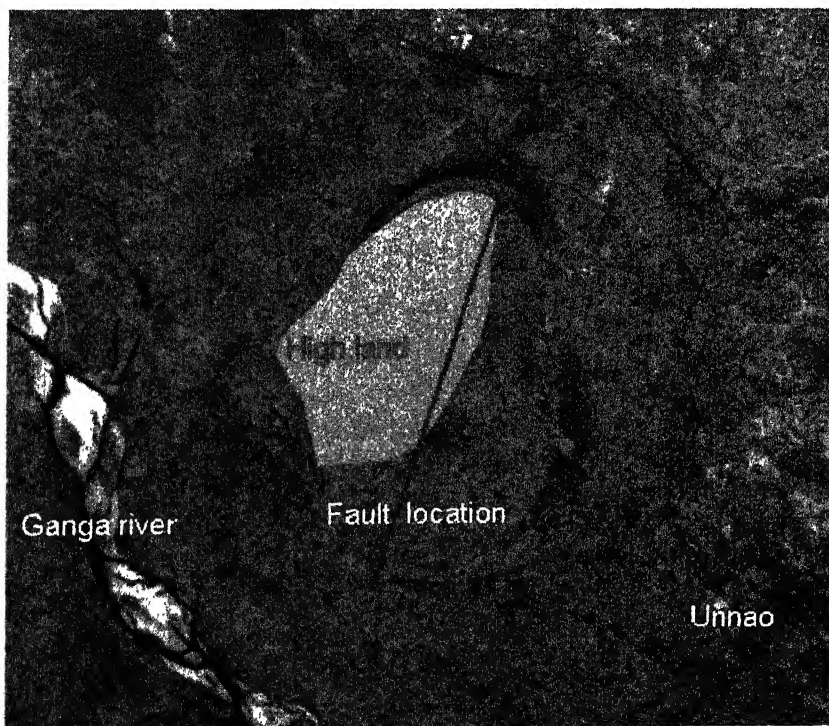
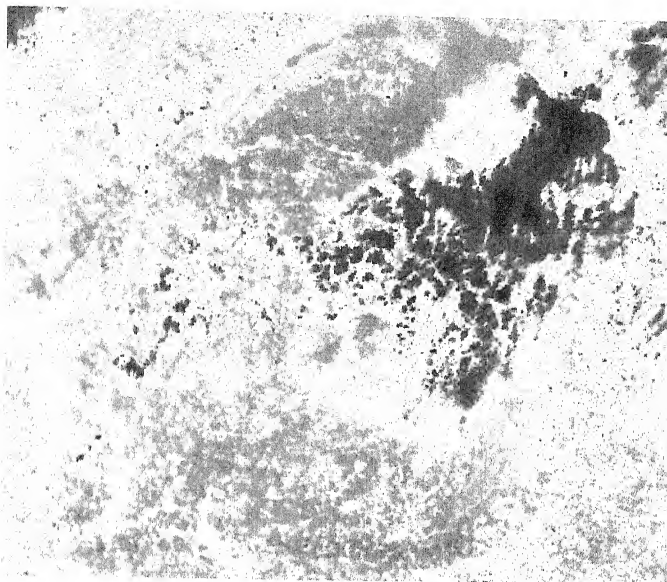
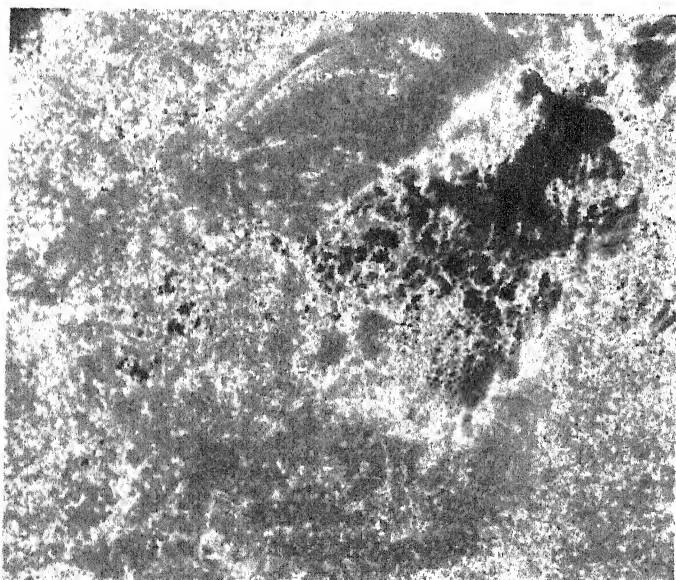


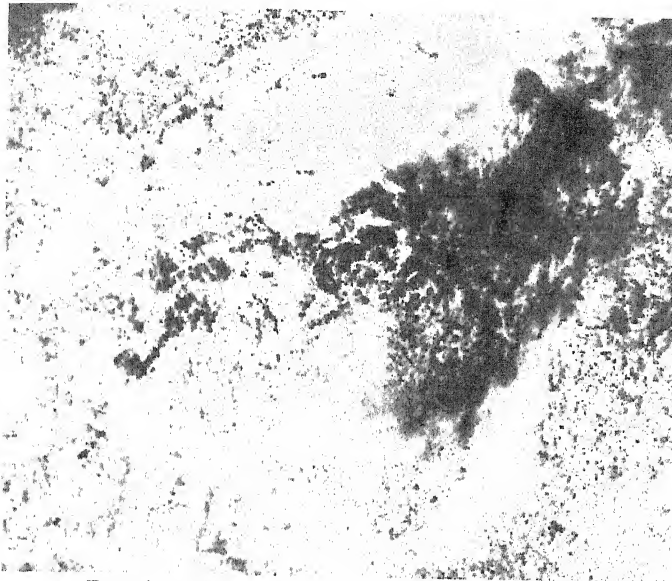
Figure 4.7 subsurface information from remote sensing data



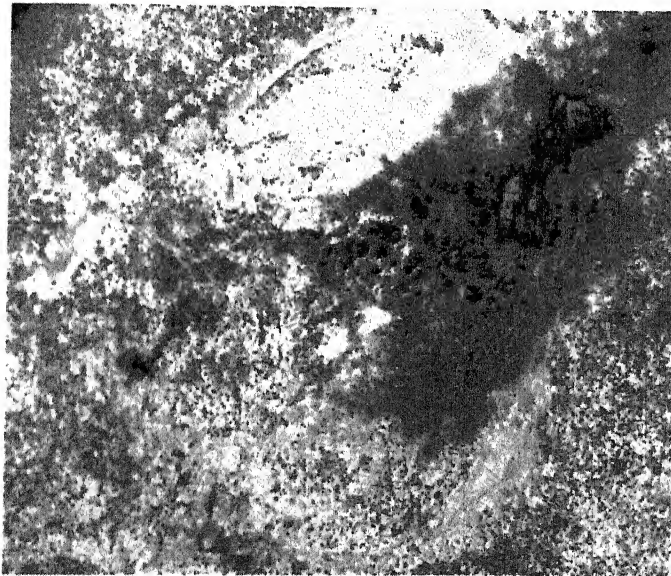
Band 1 after merging using Intensity -Hue
Saturation (IHS) method



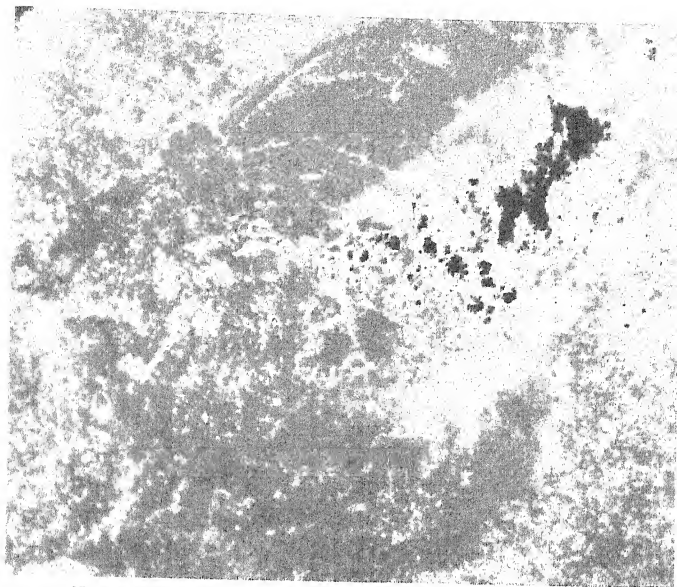
Band 2 after merging using (IHS) method



Band 3 after merging using (IHS) method

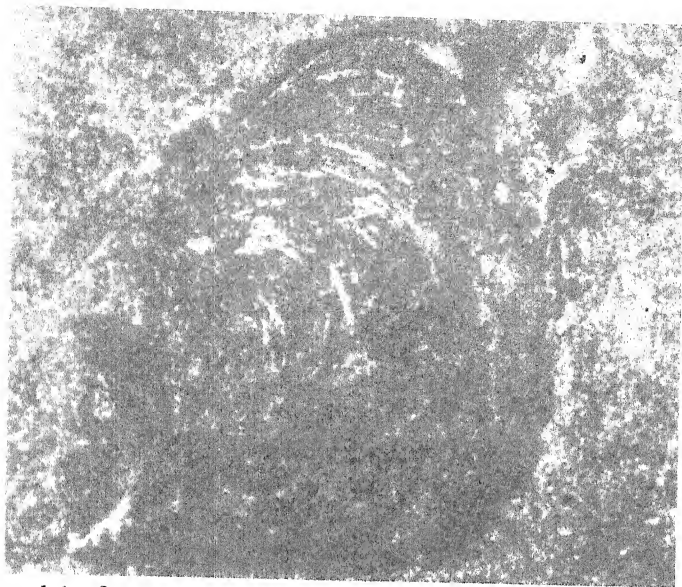


Band 1 after merging using P+XS method

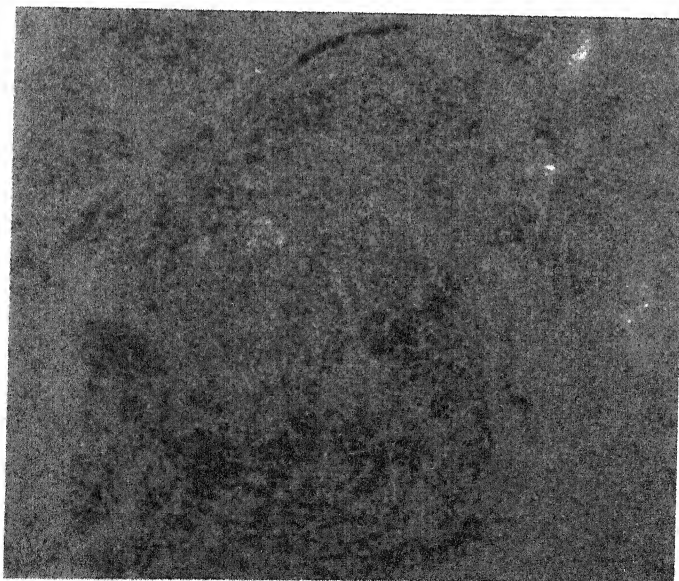


Band 2 after merging using P+XS method

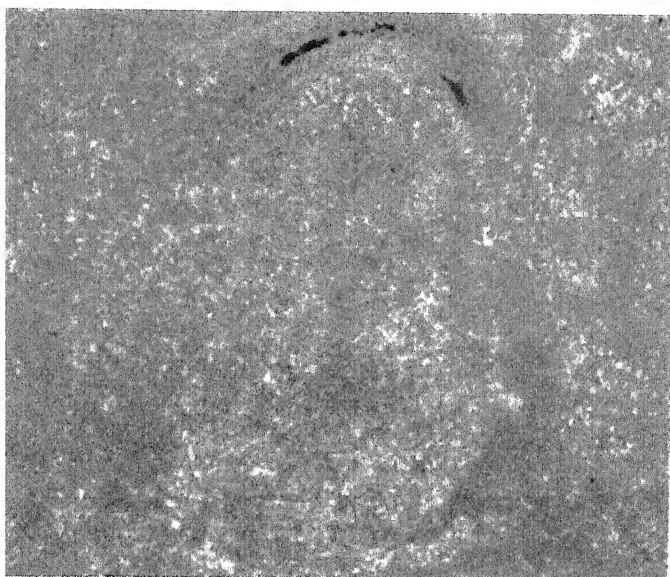
Plate 4.9



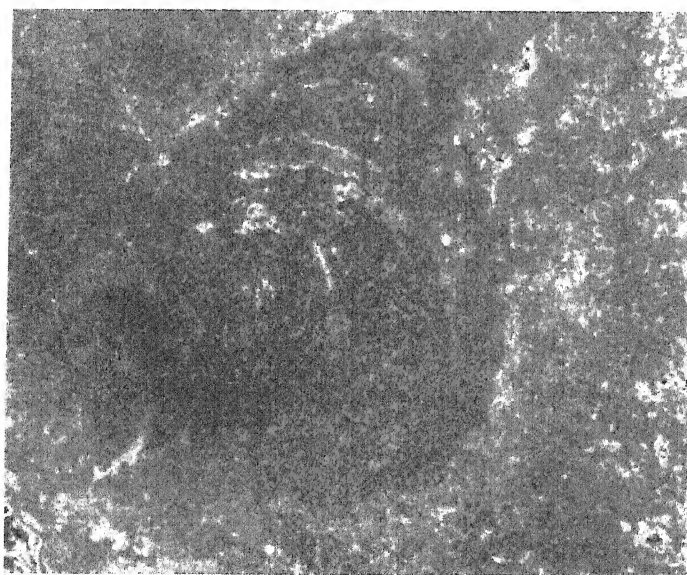
Band 1 after merging using High Pass Filter (HPF) method



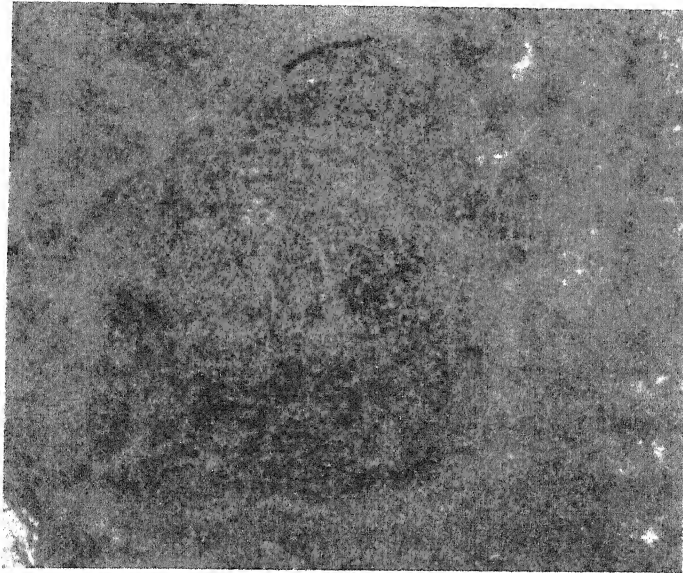
Band 2 after merging using (HPF) method



Band 3 after merging using (HPF) method



Band 1 after merging using Price method



Band 2 after merging using Price method



Band 3 after merging using Price method

4.4 Geophysical Data Analysis

4.4.1 Resistivity method

The electrical resistivity of rock formation limits the amount of current passing through the formation. It is the resistance in ohms between opposite faces of a unit cube of the material. The resistivity of rock formation varies over a wide range, depending on the material, its density, porosity, pore size and shape, water content and quality, and temperature. There are no fixed limits for resistivity of various rocks: igneous and metamorphic rocks vary in the range 10^2 to 10^8 ohm-m; sedimentary and unconsolidated rocks, 10^0 to 10^4 ohm-m. Figure 4.8 provides a representative guide to the electrical resistivity ranges of various sedimentary rocks (Todd, 1980). In relatively porous formations, the resistivity is controlled more by water content and quality within the formation compared to those by the rock matrix. The resistivity decreases with the degree of saturation and salinity of the ground water. The clay minerals conduct electric current through their matrix; therefore, clayey formations tend to display lower resistivity than compared to permeable alluvial aquifers.

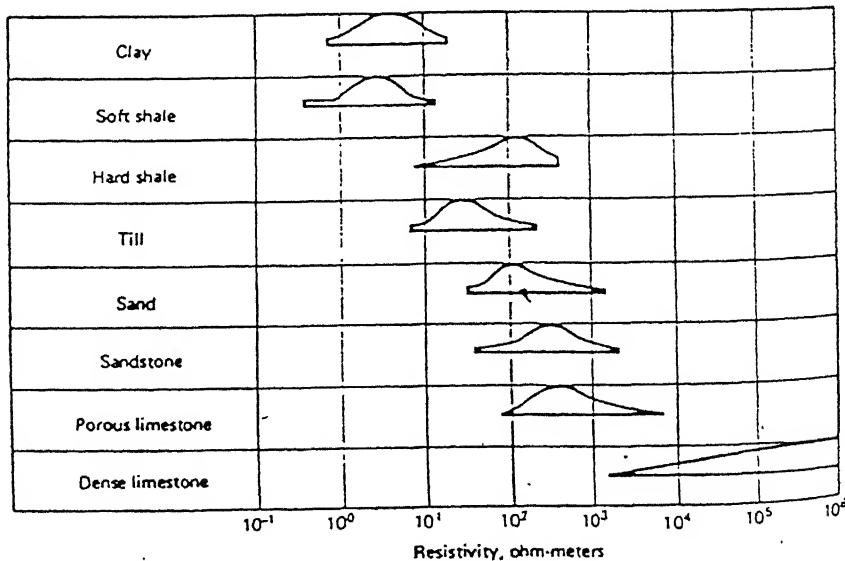


Figure 4.8 A representative guide to resistivity of various sedimentary rocks (after Todd, 1980).

4.4.1.2 Field work

Resistivity survey has been carried out in Kanpur-Unnao region near Bithoor at the left bank of Ganga river. Using OYO resistivity meter 14-resistivity soundings along the meander cutoff have been taken. These sounding points cover the entire area of channel migration pattern. The sounding locations are shown in Figure 4.9.



Figure 4.9 Location of resistivity soundings on FCC image.

The readings have been taken using Schlumberger configuration, which is described in chapter III. The field procedures (Figure 3.5) have been discussed in chapter III. At some locations (Dostinagar, Dullakhera, and Garha) it was difficult to have current electrode spacings more than 100 to 150 m due to the presence of vegetation cover. For most of locations current electrode spacings extended up to 600 m. In Figure 4.10 the OYO resistivity meter and its set up are shown.



Figure 4.10 Resistivity set up in the field.

4.4.1.3 Results and discussion

After field work, the detailed processing of data have been carried out. The apparent resistivity have been plotted with half current electrode spacings ($AB/2$) using semi-logarithmic sheet. Resix package has been used to interpret these curves. From Resix package, all the parameters including number of layers, true resistivity, and the thickness of each layers have been obtained. The variations of apparent resistivity along profiles I, II, III, IV and V are shown in Figures 4.11, 4.12, 4.13, 4.14 and 4.15. Profile (I) represents the aparent resistivity variations from south to north direction of study area along Dostinagar, Garha, Kirna, and Firouzpur (Figure 4.11). Profile (II) represents the aparent resistivity variations from south to north direction along Dullakhera, Parmani Diwankhera, and Isunyian (Figure 4.12). Profile (III) represents the aparent resistivity variations from south to north direction along Utaria, Mahipatikhera, and Powa (Figure 4.13). Profile (IV) represents the aparent resistivity variations from south to north direction along Pyarepure, Bhadeona, and Mubarkpur (Figure 4.14). Profile (V) represents 3-dimensional variations of aparent resistivity from east to west direction along Firuzpur, Isunyian, Mubarkpur and Mahipatikhera (Figure 4.15). The contour map has been generated from apparent resistivity values using 30 ohm-m contour intervals this map is shown in Figure 4.16. By studying the profiles I, II, III, IV, V, and contour

map, low apparent resistivity is clearly seen at locations Dostinagar, Dlluakhera, Garha, Pyarepure, Utaria, Parmani, Kirna, Powa, and Diwankhera. While at all the other points high apparent resistivity values are found. The highest resistivity values up to 500 ohm-m are found at locations Firuzpur, Isunyian, Mubarkpur and Mahipatikhera (Figure 4.16). Only at Dostinagar apparent resistivity shows gradually increase which may be related to the location of Dostinagar which is lying far away to the channel migration pattern (Figure 4.9). An interpretation of resistivity data using Resix package shows a very good contrast between the eastern and western parts of the meander cut-off. The layered model estimated from Resix package for each point and give very good fit with the field curves (Figures 4.17 to 4.30). The data estimated shows a large contrast in resistivity values between two sides, while they are varying between 2 – 60 ohm-m at locations Dostinagsr, Dullakhera, Garha, Pyarepure, Utaria, Kirna, Powa, and Diwankhera. The low resistivity values indicate the presence of clayey, shale and fined sand formations. The amount of sand and the presence of hard shale may give rise to the resistivity up to 60 ohm-m.

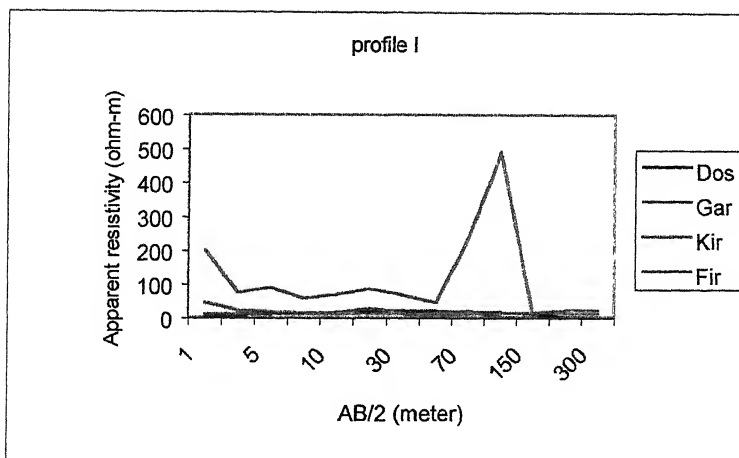


Figure 4.11 - Profile I (S-N): Apparent resistivity variations along Dostinagar, Garha, Kirna, Firouzpur.

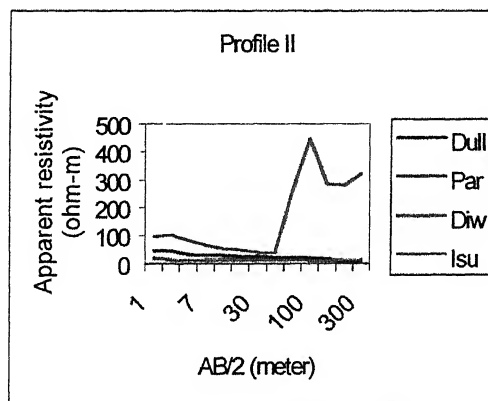


Figure 4.12 - Profile II Apparent resistivity variations along Dullakhera, Parmani, Diwankhera, Isunyan.

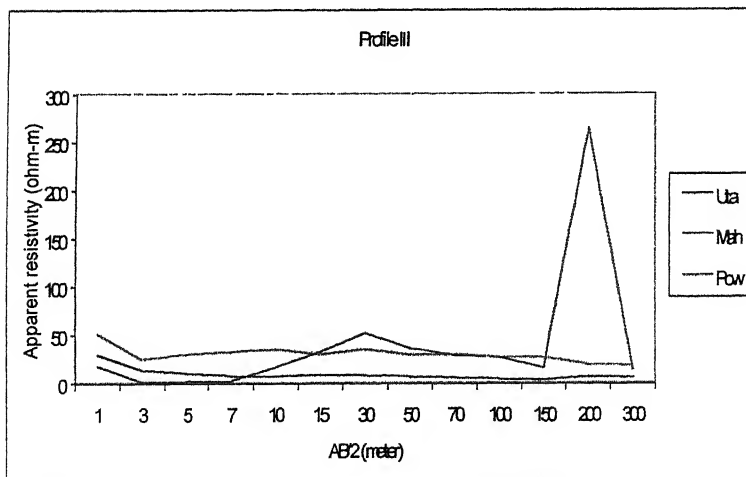


Figure 4.13 - Profile III (S-N): Apparent resistivity variations along Utaria, Mahipatikhera, Powa

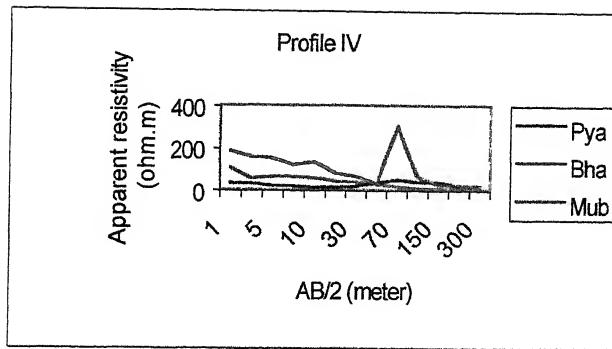


Figure 4.14 Profile IV (S-N): Apparent resistivity variations along Pyrepure, Bhadeona, Mubarkpur.

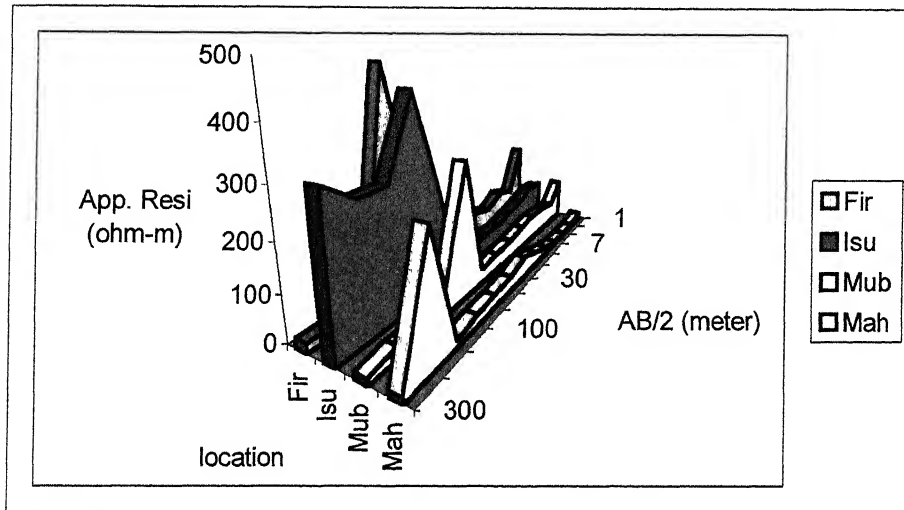


Figure 4.15 - 3-dimension Apparent Resistivity variations along Profile V Firuzpur, Isunyan, Mubarkpur and Mahaptikhera.

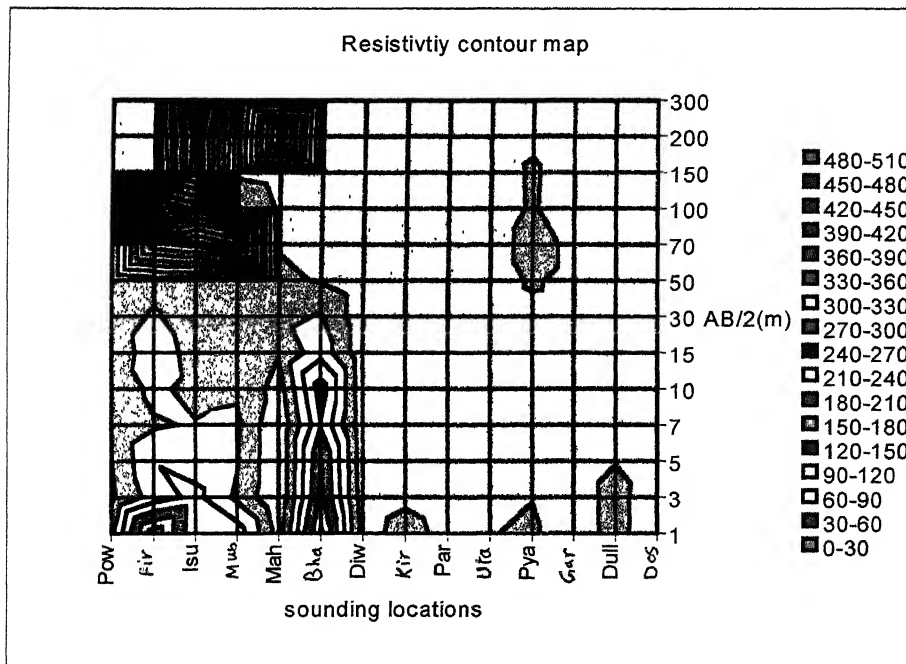


Figure 4.16 shows Apparent Resistivity contours in the study area.

The data collected from the eastern part was easy to interpret since the fitting errors between master and field curves was very small compared to locations Firuzpur, Isunyan, Mubarkpur, and Mhaptkhera in the western part. In the eastern part the resistivity change gradually with the depth, which indicates that the entire part contains fresh alluvial deposits. In this part the ground water quality has played a significant role in resistivity data. Based on the vertical resistivity profiles it can be concluded that no significant contrast in the eastern side is seen in sedimentation pattern. From layered models a very low resistivity layer is seen which may contain salt water. This layer may be located near Kirna at depth of 104 m, Utaria at depth 38 m with resistivity equal to 0.5 ohm-m, Pyarepure at depth 40.5 m with resistivity 1.63 ohm-m, Bahadeona at depth 26.28 m with resistivity 2.24 ohm-m, and also in Diwankhera located at depth 48.16 m. The presence of saline soil in U.P. and its relation has been recently discussed by Srivastava and Singh (1998, 1999). The good fit has not been found at the locations high resistivity layer is present, so the thickness of layers estimated is not very accurate. The layered models also show that while moving from south to north along profiles I, II, III and IV the resistivity values increase rapidly this may be due to the presence of fine sand to coarse sand to sandstone sometimes. In the western part the analysis of resistivity variations show sudden change in layers characteristics and their physical properties, which is also reflected by resistivity values. The resistivity of this part is too high compared to other part, which gives an indication of the presence of the layers characterized by different sedimentation pattern and older layers compared to other part. The presence of sand, compact sand or sandstone, and gravel give rise to the resistivity variations. The water in this part is much cleaner, this is reflected from resistivity data. The depth of the water table changes from this part to other part due to change in topography. The results show the presence of very high resistivity layer more than 1000 ohm-m beneath Firuzpur, Isunyan, Mahiptkhera, and Mubarkpur (Figures 4.27 to 4.30). This high resistivity layer is located at the depth range 40 – 80 m. From the above discussion, we conclude that the entire western part is uplifted area may be caused by a fault in the basement. Along which subsurface deformation may be taken place giving rise to the uplift to the basement. Such deformations may have led to the migration of Ganga river towards west.

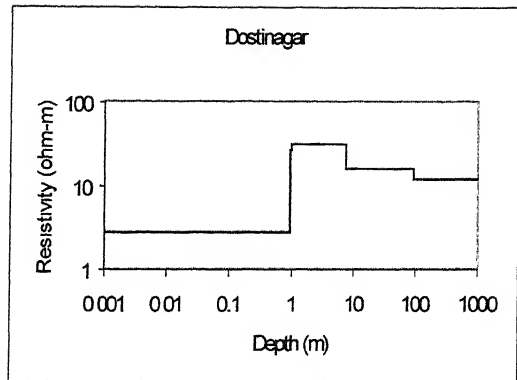
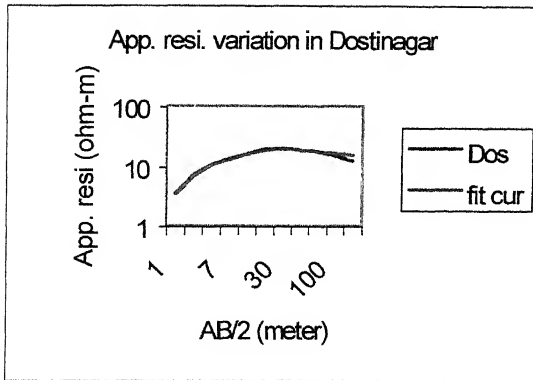


Figure 4.17 - App. Resi. variations (left) and Layered model estimated at Dostinagar

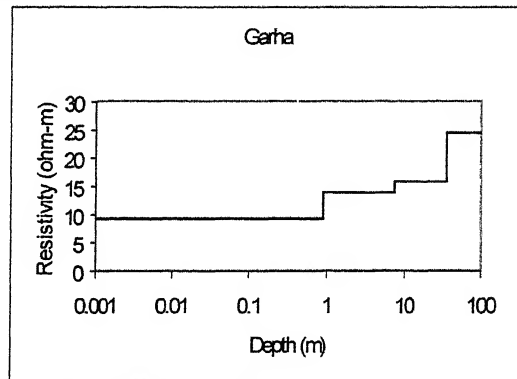
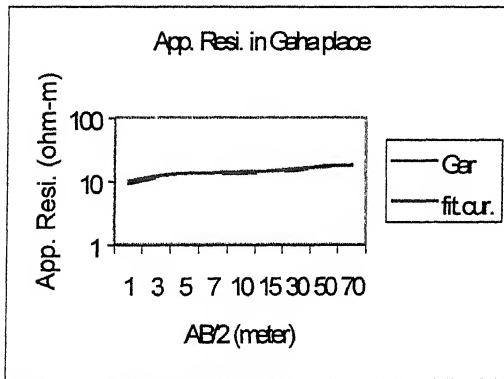


Figure 4.18 - App. Resi. variations (left) and Layered model estimated at Garah.

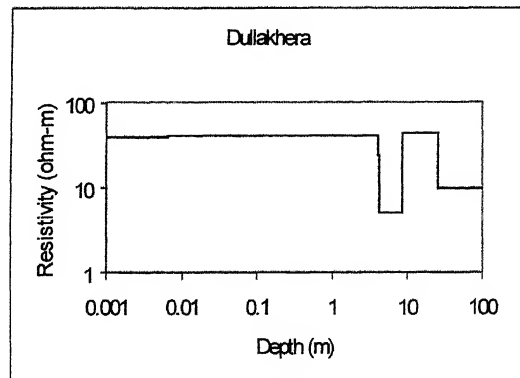
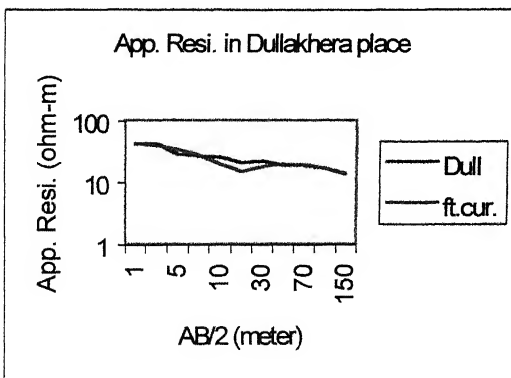


Figure 4.19 - App. Resi. variations (left) and Layered model estimated at Dullakhera.

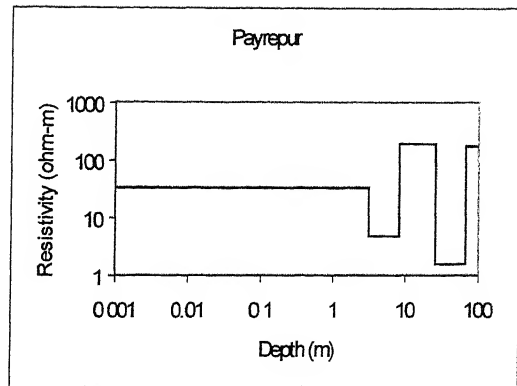
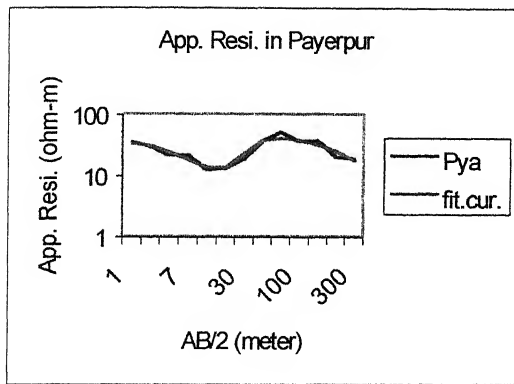


Figure 4.20 - App. Resi. variations and Layered model estimated at Payrepur.

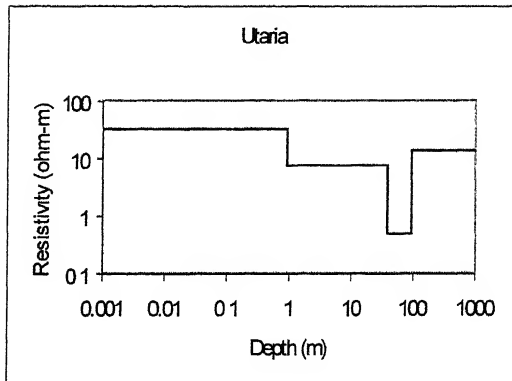
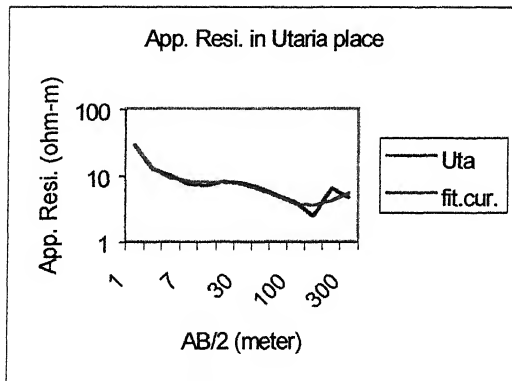


Figure 4.21 - App.Resi. variations and Layered model estimated at Utaria.

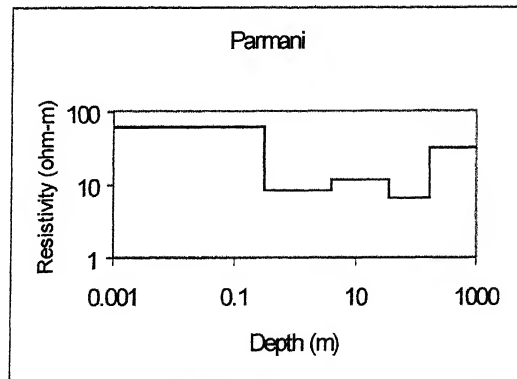
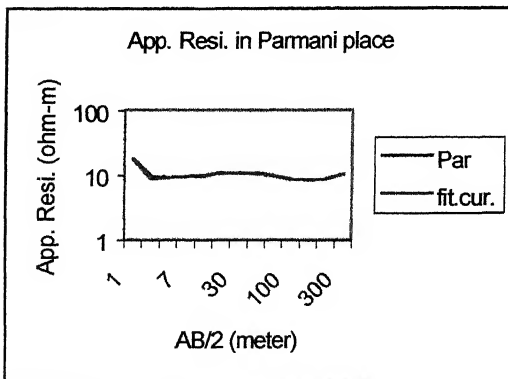


Figure 4.22 - App. Res. variations and Layered model estimated at Parmani

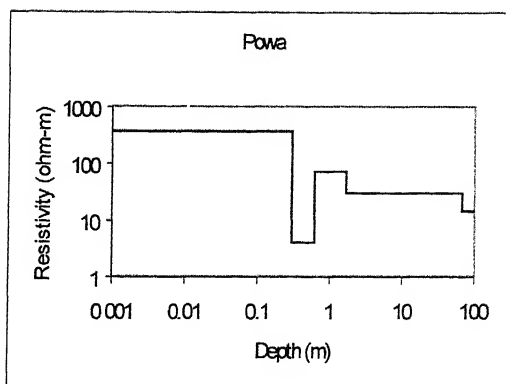
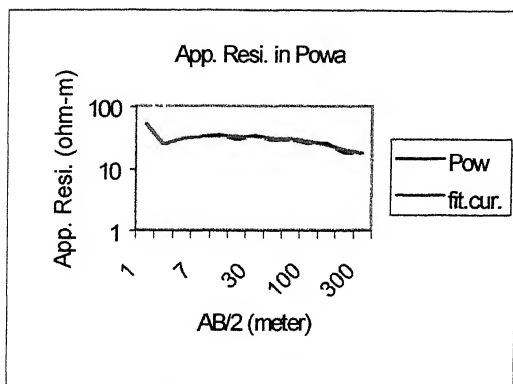


Figure 4.23 - App. Resi. variations (left) and Layered model estimated at Powa.

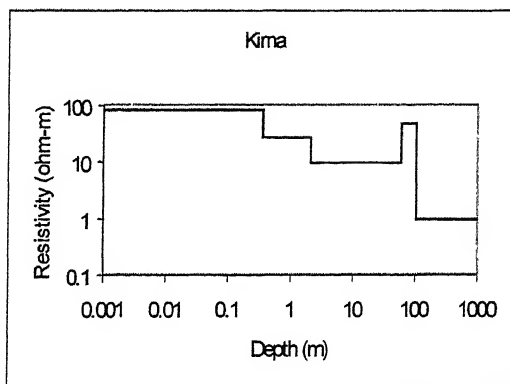
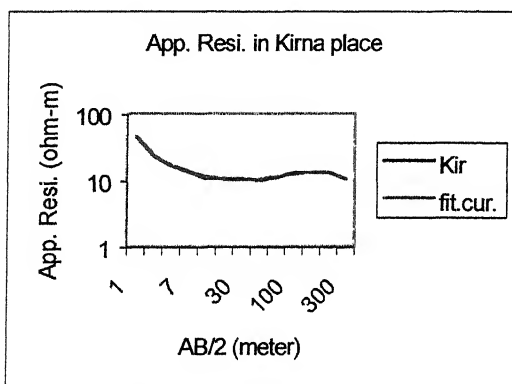


Figure 4.24 - App. Resi. variations (left) and Layered model estimated at Kirna.

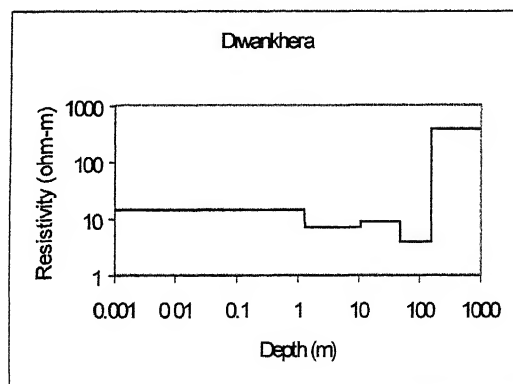
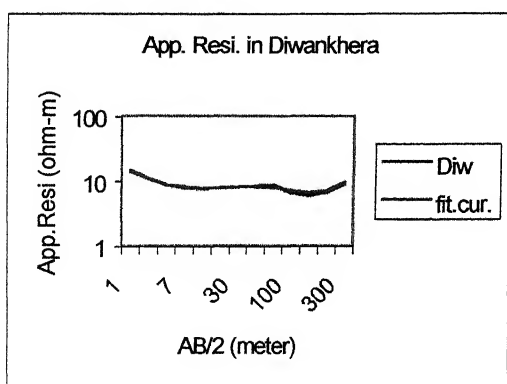


Figure 4.25 - App. Resi. variations (left) and Layered model estimated at Diwankhera.

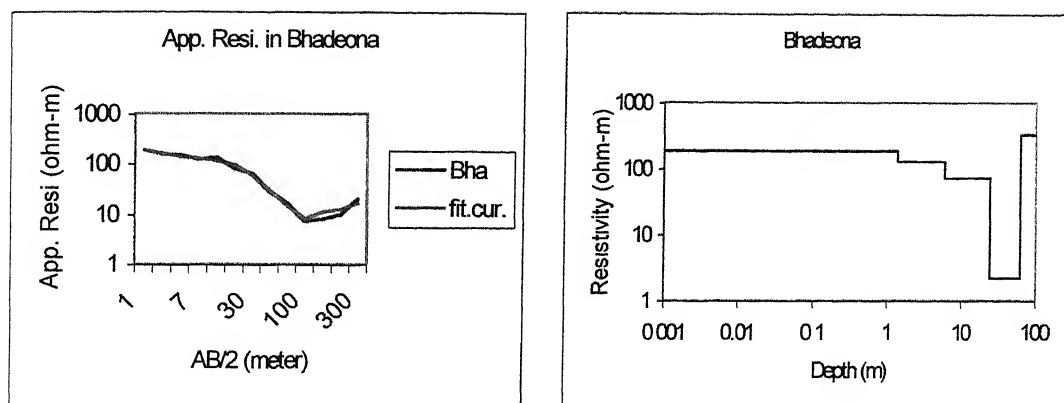


Figure 4.26 - App. Resi. variations (left) and layered model estimated at Bhadeona.

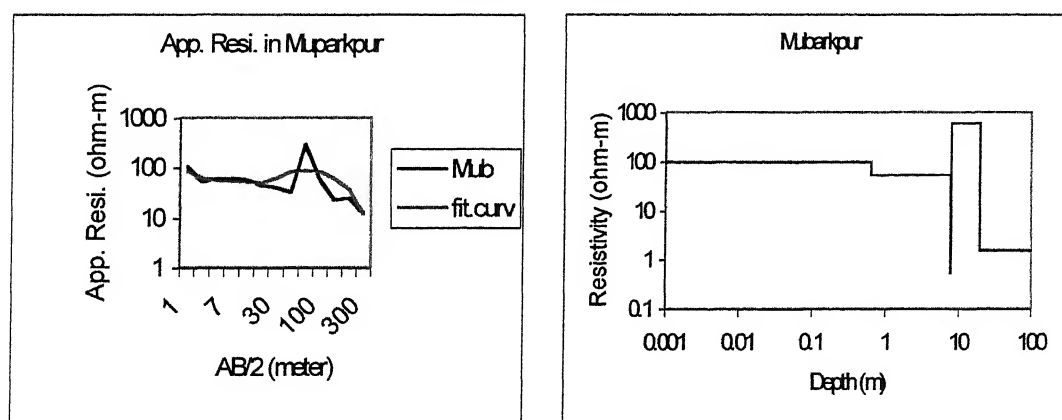


Figure 4.27 - App. Resi. variations (left) and layered model estimated at Mubarkpur.

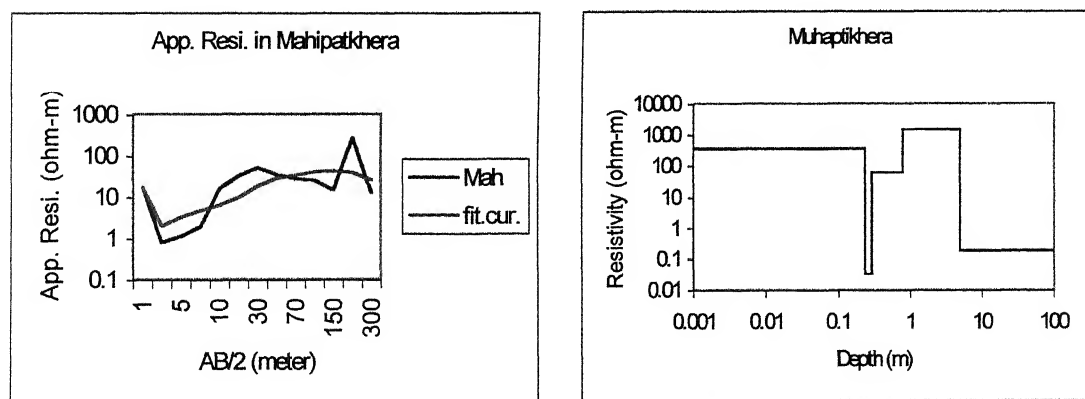


Figure 4.28 - App. Resi. variations (left) and Layered model estimated at Muhaptikhera.

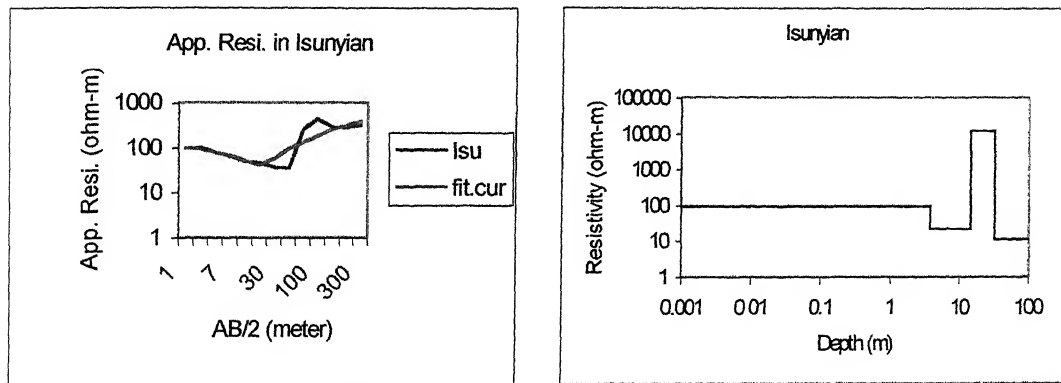


Figure 4.29 - App. Resi. variations (left) and Layered model estimated at Isunyan.

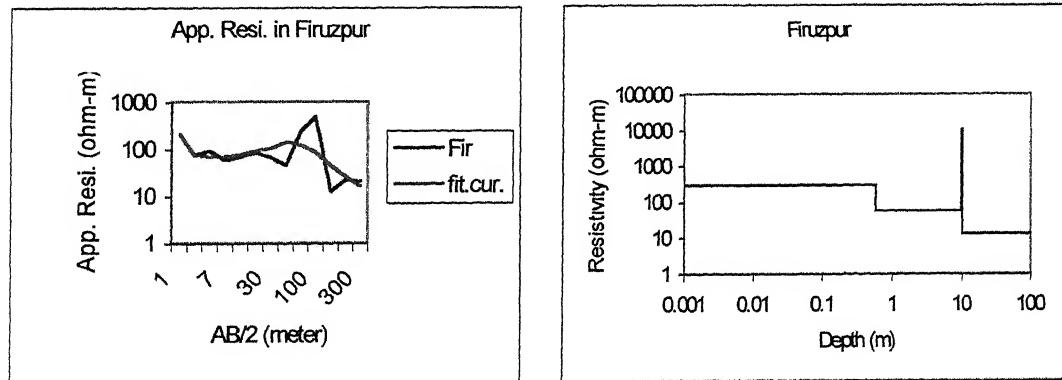


Figure 4.30 - App. Resi. variations (left) and Layered model estimated at Firuzpur.

4.5 Integration of Remote sensing and Resistivity Data

The resistivity data obtained from the resistivity soundings show one to one relation with the results obtained from the image processing (Figure 4.7). The results from the resistivity soundings show drastic change across a profile crossing the large meander cut off. Remote sensing analysis has provided a very good information about subsurface conditions especially when the subsurface structure cause a change to sedimentation pattern or any significant change to surface features like discontinuity of geomorphological features, anomalies in vegetation index, topography variations and change in surface layer properties.

Thresholding techniques especially Otsu thresholding technique, which is very useful in geological applications and the use of different optimal thresholding values, can give a good idea about the study area. Thresholding has also provided information about lithological edges apart from the conventional edges due to roads and urban areas. Remote sensing data used successfully to map the fault and high land area. From the present study we conclude that the integration of remote sensing data and resistivity data is very useful in deducing the subsurface information and its relation with the surface manifestations.

Chapter V

CONCLUSION

5.1 GENERAL

The main objective of the present study is to investigate the subsurface structure by using remote sensing data and to study the effect of merging and thresholding techniques on geological edge extraction. To achieve these objectives the following studies have been carried out:

- Study of the normalized difference vegetation index (NDVI) and classification of image from study area based on NDVI.
- Map of geomorphological features from stretching FCC.
- Various merging techniques (HPF, Price, HIS, P+XS) have been applied to improve the visual interpretation and to see the effect of merging on edge extraction.
- Sobel, Laplacian, High pass filters, and Otsu thresholding technique have been applied to enhance the geological edges before and after merging.
- Resistivity survey (field measurement) has been carried out from the study area. Resix package has been used for the analysis of resistivity soundings data.
- The remote sensing data has been integrated with the resistivity variations obtained from conventional resistivity method.

5.2 Results

From the study carried out in present thesis the conclusion can be summarized as:

- I. Both, resistivity and remote sensing data have shown the occurring of meander cutoff of Ganga river. The main reasons behind occurring of channel migration pattern of Ganga river may be due to:
 1. Geomorphological process.
 2. Occurring of cross faults in the basement.
 3. Uplift of basement rocks under the western side of meander cutoff.

- II. Resistivity measurements have indicated a uniform change in apparent resistivity values on the eastern side of meander cutoff. On the other hand anomalous apparent resistivity values have been found on the other side.
- III. Analysis of resistivity data has indicated that the presence of fault and high resistivity layer under the western side of meander cutoff.
- IV. Geological edges are very clear using Band 2 data compared to Band 3.
- V. Out of the four edge detection techniques used, Otsu thresholding technique has given the best edge enhancement.
- VI. NDVI contrast suggests two distinct areas which are characterized by two distinct subsurface settings.
- VII. The applied merging techniques have not given any improvement for geological edge extraction.
- VIII. Out of the four merging methods used in the present thesis the HPF and Price algorithm have given the best merged data. HPF is found to give much better results compared to Price technique.
- IX. HPF and Price algorithms have been used effectively to eliminate the cloud cover from merged data.
- X. Remote sensing data has proved to provide an efficient alternative to the conventional geological or geophysical surveys.

5.3 Future work

During the data collection periods, there have been a common feeling among the residence of that area near the fault location shows poor ground water quality and sharp variations in the water quality from well to well. Therefore, the study of the ground water quality and its relationship with surface and subsurface conditions may be taken in the future.

REFERENCES

- Aditya, S., Raju, A. T. R., and Shukla, S. N., (1979), "Assessment of hydrocarbon prospects of the Sub-Himalayan Punjab and Ganga basins", *Geological Survey of India*, 41 (5), pp. 127 - 129.
- Agocs, W. B., (1957), "Aeromagnetic survey of Indo-Gangetic plains and Rajasthan", *Oil and Natural Gas Commission*.
- Ansari, A. A., Singh, I. B., and Tobschall, H. J., (1999), "Status of anthropogenically induced metal pollution in the Kanpur – Unnao industrial region of the Ganga plain, India", *Environmental Geology*, 38 (1), pp. 25 – 28.
- Argyle, E., (1971), "Techniques for edge detection", *Proceedings of IEEE*, Vol.59, pp.285 - 287.
- Balakrishnan, T. S., and Choudhury, S. K., (1976), "Geophysical studies of the Himalayan foot hills of Punjab and Himachal Pradesh and their geological correlation with the adjoining Punjab plains", *Geological Survey of India*, 41 (5), pp. 175 - 180.
- Bisaria, B. K., Pandey, B. N., Khan, A. U., and Bhartiya, P. S., (1996), "Geomorphology and evaluation of Ganga plain in Uttar Pradesh", *Geological Survey of India*, Sp. Pub. 21 (2), pp. 209 – 214.
- Burns, J. B., Hanson, A. R., and Riseman, E. M., (1986), "Extracting straight lines", *IEEE Transactions, Pattern Analysis and Machine Intelligence*, vol. PAMI - 8, no. 4, pp. 425-455.
- Burrard, S. G., (1915), "Origin of the Indo-Gangetic trough, commonly called Himalayan fare deep", *Proc. Roy. Soc. London*, 91 A, pp. 220 - 222.
- Chavez, Pat S., (1986), "Digital merging of Landsat TM and digitized NHAP data for 1:24000 scale image mapping", *Photogrammetric Engineering and Remote Sensing*, vol. 52, No. 10, pp. 1937 -1646.
- Chavez, Pat S., and Bowell, J. A., (1988), "Comparison of the spectral information content of Landsat Thematic Mapper and SPOT for three different sites in the Phoenix, Arizona region", *Photogrammetric Engineering and Remote Sensing*, vol. 54, No. 12, pp. 1699-1708.
- Carper, J., Lillesand, T. M., and Kiefer, R. W., (1990), "The Use of Intensity – Hue – Saturation transformations for Merging SPOT Panchromatic and Multispectral Image Data" *Photogrammetric Engineering and Remote Sensing*, vol. 56, No. 4, pp. 459 – 467.
- Chavez, S. Pat, Sides, S. C., and Anderson, J. A., (1991) "Comparison of three different methods to merge multi-resolution and multi-spectral Data: Landsat TM and Spot

Panchromatic", *Photogrammetric Engineering and Remote Sensing*, vol. 57, No. 3, pp. 295 – 303.

Choudhury, S. K. (1975), "Gravity and crustal thickness in the Indo-Gangetic plains and Himalayan Region, India" *Geophys. J. R. astr. Soc.* vol. 40, pp. 441 – 452.

Crane randy, (1997), *A Simplified Approach to Image Processing*, Prentice Hall PTR, New Jersey.

Davis, L. S., (1975), "A survey of edge detection techniques", *Computer Graphics and Image Processing*, vol. 4, pp. 248-270.

Eremenko, N. A. and Negi, B. S. et al. (1968), "Tectonic Map of India", Oil and Natural Gas Commission, India.

Ghosh, D. K., and Singh, I. B., (1988), "Structural and geomorphic evolution of north western part of Indo-Gangetic plain", *Proc. National seminar and recent quaternary studies in India, Baroda*, pp. 164 -170.

Gupta, H. K. and Nyman, D. C., and Landisman, Mark (1976), "Shield like Upper Mantle velocity structure below the Indo-Gangatic Plains: Inferences drawn from period surface wave dispersion studies", *Earth and Planetary Science Letters*, pp. 51 – 52.

Hall, E. L., (1979), "Computer Image Processing and Recognition", Academic Press, Toronto. pp. 396 - 409.

Harris, R., and Murray, R., (1990), "IHS transform for the integration of radar imagery with other remotely sensed data", *Photogrammetric Engineering and Remote Sensing*, vol. 56, No. 12, pp. 1631-1641.

Hayden, R., Dalke, G. W., and Henkel, J., (1982), "Application of the IHS color transform to the processing of multi-sensor data and image enhancement", *Proceedings, International symposium on Remote sensing of Arid and semi-Arid lands*, Cario, Egypt, pp. 599-616.

Khan, A. U., Bhartiya, S. P., and Kumar, G., (1996), "Cross faults in the Ganga Basin and their surface manifestations" *Geological Survey of India*, Sp., Pub 21 (2). pp. 215 – 220.

Khan, A.U., and Joshi, D. D., (1989), "Quaternary geology and geomorphology of a part of Ganga basin Aligarh, Budaun, Bulandshahar and Muradabad district U.P.", Rep. *Geological Survey of India*.

Krishnan, P. V., (1990), "Exploration in Himalayan foothills and Punjab Ganga plains", Proc. Of the conference on integrated exploration Res., Achievements and perspectives KDMIPE Dehradun, pp. 27-30.

- Levialdi, S., (1983), "Edge extraction techniques", In Faugeras, O. D., *Fundamentals in computer vision: An advanced course*, pp. 117 - 144, Cambridge University Press, Cambridge.
- Narain, H., and Kaila, K., (1975), *Inferences about the Vindhyan Basin From Geophysical Data*, Hindustan Publishing Corporation, New Delhi.
- NRSA, (1995), *IRS-1C Data User Handbook*, Hyderabad.
- Oldham, R. D., (1917), "The structure of the Himalayas the Gangetic plains", *Geological Survey of India*, 42 (2), pp. 1-5.
- Otsu Nobuyuki, (1979), "A Threshold selection method from Gray- Level Histograms" *IEE*, vol. Smc-9, No. 1, pp. 62 – 66.
- Pellemans, A. H. J. M., Jordans, R. W. L., and Allewijn, R., (1993), "Merging multi-spectral and panchromatic SPOT images with respect to the radiometric properties of the sensors" *Photogrammetric Engineering and Remote Sensing*, vol. 59, No. 1, pp. 81 – 87.
- Pratt, W. K. (1977), "Digital Image Processing", J. Wiley and Sons, New York.
- Price, J. C., (1987), "Combining panchromatic and multi-spectral imagery from dual resolution satellite instruments", *Remote Sensing of Environment*, No. 21, pp. 119 – 128.
- Rao, M. B. R., (1973), "The subsurface geology of the indo Gangetic plains", *Journal of Geological Society of India*, 14 (3), pp. 213 - 220.
- Reddy, V. D., (1995), *Engineering Geology for Civil Engineers*, Oxford & IBH Publishing Co., New Delhi.
- Richards, John. A, (1993), *Remote sensing Digital Image Analysis*, Springer – Verlag, Berlin.
- Rosenfeld, A., and Kak, A. c., (1982), "Digital picture processing", second Edition, vol. 2, Academic Press, New York.
- Sahoo, P. K., Soltani, S., and Wong A. K. C., (1988), "A survey on thresholding techniques", *Computer Vision, Graphics and Image Processing*, vol. 41, pp. 233-260.
- Sastri, V. V., Bhandari, L. L. Raju, A. T. R., and Datta, A. K., (1971), "Tectonic Framework and Subsurface Stratigraphy of the Ganga Basin", *Journal of the Geological Society of India*, vol. 12, No. 3, pp. 222 - 233.
- Shaban, M. A., (1999), *Digital classification of urban environments using satellite imagery*, Phd. Thesis, IIT. Kanpur.

- Singh, I. B., and Bajpai, V. N., (1989), "Significance of Syndepositional Tectonics in Facies Development, Gangatic alluvium near Kanpur, Uttar Pradesh", *Journal of the Geological Society of India*, vol. 34, pp. 61 - 66.
- Singh, I. B., and Rastogi, S. P., (1973), "Tectonic framework of Gangetic alluvium with special reference to Ganga river in Uttar Pradesh", *Current Science*, (9), pp. 305-307
- Srivastava, A., and Singh, R. P., (1999), "Surface manifestation due to subsurface ridge", *International J. Remote Sensing*, vol. 20, pp. 3461-3466.
- Srivastava, A. and Singh, R. P., (1998), "Subsurface control on salt-affected regions of Indo-Gangetic basin", *J. Geological Soc.*, v. 52, pp. 473-476.
- Susmitha, D., (1999), Merging of multi-sensor and multi-resolution satellite data for the extraction of linear features, M.Tech Thesis, IIT. Kanpur.
- Teillet, P., and Bonn, F., (1985), "Integration of the Spot Panchromatic Channel into its multi-spectral mode for image sharpness enhancement" *Photogrammetric Engineering and Remote Sensing*, vol. 51, No. 3, pp. 311 – 316.
- Thormodsgard, J.M., and Feuquay, J.W., (1987), "Large scale image mapping with SPOT", *Proceedings, SPOT-1 utilization and Assessment Results*, Paris, France.
- Tood, David K., (1980), *Ground Water Hydrology*, John Wiley & Sons, NewYork.
- Vrabel, J., (1996), "Multispectral imagery band sharpening study", *Photogrammetric Engineering and remote Sensing*, Vol. 62, No. 9, pp. 1075-1083.
- Verma, R. K., (1991), *Geodynamics of the Indian Peninsula and the Indian plate margin*, Oxford & IBH Publishing Co., New Delhi.
- Waida, D. N., (1931), "The syntaxis of the northwest Himalayan: its rocks, tectonics and orogeny", *Rec.Geological survey of India*, 65, pp. 189 – 220.
- Wald. L., Ranchin, T., and Mangolini, M., (1997), "Fusion of satellite images of different spatial resolutions, Assessing the quality of resulting images", *Photogrammetric Engineering and Remote Sensing*, Vol. 63, No. 6, pp. 691-699.
- Welch, R., and Ehlers, M., (1987), "Merging multi-resolution SPOT HRV and Landsat TM Data" *Photogrammetric Engineering and Remote Sensing*, vol. 53, No. 3, pp. 301 – 303.
- Yocky, D. A., (1996), "Multiresolution wavelet decomposition image merger of Landsat Thematic Mapper and SPOT Panchromatic data" *Photogrammetric Engineering and Remote Sensing*, vol. 62, No. 9, pp. 1067 – 1074.

Appendix I

List of tables showing the values of resistivity models for all point.

Dostingar

No. of layers	Resistivity (ohm.m)	Thickness (m)
1	2.8	0.935
2	27.18	0.0567
3	31.87	6.6
4	16.1	85.12
5	12.1	-

Mubarkpur

No. of layers	Resistivity (ohm.m)	Thickness (m)
1	97.7	0.628
2	55.83	7.18
3	0.563	0.2
4	616	12.04
5	1.58	-

Garaha

No. of layers	Resistivity (ohm.m)	Thickness (m)
1	9.33	0.888
2	14	6.53
3	15.93	28.98
4	24.55	-

Bhadeona

No. of layers	Resistivity (ohm.m)	Thickness (m)
1	187.8	1.36
2	132.3	4.51
3	73.97	18.64
4	2.24	38.13
5	334	-

Dullakhera

No. of layers	Resistivity (ohm.m)	Thickness (m)
1	39.32	0.0064
2	41.39	3.97
3	24.58	0.097
4	5.09	4.36
5	44.27	17.41
6	9.82	-

Payrepur

No. of layers	Resistivity (ohm.m)	Thickness (m)
1	33.58	3.10
2	4.93	4.93
3	198.5	18.22
4	1.63	40.55
5	177.8	-

Kirna

No. of layers	Resistivity (ohm.m)	Thickness (m)
1	83.33	0.358
2	27.66	1.74
3	9.82	58.12
4	48.32	43.94
5	0.959	-

Powa

No. of layers	Resistivity (ohm.m)	Thickness (m)
1	370.8	0.295
2	4.13	0.316
3	73.94	1.08
4	31.09	66.79
5	14.56	-

Firuzpur

No. of layers	Resistivity (ohm.m)	Thickness (m)
1	297.6	0.576
2	61.39	9.08
3	11053	0.591
4	13.72	-

Isunyan

No. of layers	Resistivity (ohm.m)	Thickness (m)
1	95.87	3.79
2	23.08	10.9
3	12684	17.84
4	11.35	-

Diwankhera

No. of layers	Resistivity (ohm.m)	Thickness (m)
1	14.52	1.28
2	7.19	9.35
3	9.11	37.51
4	4.03	108.8
5	399.8	-

Muhapitkhera

No. of layers	Resistivity (ohm.m)	Thickness (m)
1	385.6	0.237
2	0.0352	0.0526
3	65.6	0.475
4	1659	4.07
5	0.192	-

Utaria

No. of layers	Resistivity (ohm.m)	Thickness (m)
1	32.82	0.9
2	7.74	37.8
3	7.74	54.6
4	0.5	-

Parmani

No. of layers	Resistivity (ohm.m)	Thickness (m)
1	61.84	0.311
2	8.36	3.66
3	11.84	30.65
4	6.68	132.7
5	32	-

Appendix II Resistivity Observations

Name of the place : Dostinagr

Sr.No	P1P2/2 (m)	C1C2/2 (m)	Resistance (ohm.m)	G	App.Resi (ohm.m)
1	0.5	1	1.4126	2.66	3.4
2	0.5	3	0.254	0.22	7.25
3	0.5	5	0.13116	0.08	10.4
4	1.0	5	0.27595	0.16	10.8
5	1.0	7	0.174425	0.0816	13.4
6	1.0	10	0.100425	0.04	15.77
7	1.0	15	0.0519	0.0177	18.4
8	3.0	15	0.164	0.0533	19.3
9	3.0	30	0.041525	0.0133	19.6
10	5.0	30	0.07133	0.0222	20.2
11	5.0	50	0.0235	0.008	18.45
12	5.0	70	0.011525	0.0041	17.66
13	7.0	70	0.01683	0.0057	18.55
14	7.0	100	0.0091	0.0028	20.4
15	9.0	100	0.108	0.0036	18.85
16	11.0	150	0.00365	0.00195	11.76
17	15.0	150	0.005925	0.00266	13.97

Name of the place : Garha

Sr.No	P1P2/2 (m)	C1C2/2 (m)	Resistance (ohm.m)	G	App.Resi (ohm.m)
1	0.5	1	3.885	2.66	9.4
2	0.5	3	0.4359	0.22	12.45
3	0.5	5	0.168	0.08	12.42
4	1.0	5	0.3275	0.16	12.86
5	1.0	7	0.1734	0.0816	13.35
6	1.0	10	0.0805	0.04	12.6
7	3.0	10	0.255	0.12	13.35
8	3.0	15	0.2237	0.0533	26.37
9	3.0	30	0.0311	0.0133	14.8
10	5.0	30	0.0528	0.0222	14.9
11	9.0	50	0.04	0.0144	17.45
12	11.0	60	0.03475	0.0122	17.87

Name of the place : Kirna

Sr.No	P1P2/2 (m)	C1C2/2 (m)	Resistance (ohm.m)	G	App.Resi (ohm.m)
1	0.5	1	18.6215	2.66	45
2	0.5	3	0.8426	0.22	24.06
3	0.5	5	0.1756	0.08	16.5
4	1.0	5	0.4199	0.16	16.48
5	1.0	7	0.17355	0.0816	13.4
6	1.0	10	0.068	0.04	10.7
7	3.0	15	0.091	0.0533	10.73
8	7.0	30	0.05207	0.0311	10.52
9	7.0	50	0.0175	0.012	9.82
10	11.0	70	0.015625	0.00898	10.9
11	11.0	100	0.00913	0.0044	13.04
12	15.0	150	0.00545	0.00266	12.87
13	19.0	200	0.004	0.0019	13.3
14	19.0	300	0.0014	0.00084	10.42

Name of the place : Firozpur

Sr.No	P1P2/2 (m)	C1C2/2 (m)	Resistance (ohm.m)	G	App.Resi (ohm.m)
1	0.5	1	84.5	2.66	202.7
2	0.5	3	2.55	0.22	72.83
3	1.0	5	2.25	0.16	88.4
4	1.0	7	0.734	0.0816	56.5
5	1.0	10	0.436	0.04	68.2
6	1.0	15	0.2765	0.0177	92.7
7	3.0	50	0.0337	0.0048	44.1
8	7.0	70	0.211	0.0057	232.6
9	7.0	100	0.2291	0.0028	514
10	11.0	150	0.0039	0.00195	12.56
11	19.0	200	0.0066	0.0019	21.1
12	19.0	300	0.0028	0.00084	21

Name of the place : Dullakhera

Sr.No	P1P2/2 (m)	C1C2/2 (m)	Resistance (ohm.m)	G	App.Resi (ohm.m)
1	0.5	1	17.3534	2.66	41.9
2	0.5	3	1.506	0.22	43.011
3	0.5	5	0.3651	0.08	28.7
4	1.0	5	0.74165	0.16	29.12
5	1.0	7	0.33916	0.0816	26
6	3.0	10	0.4963	0.04	25.9
7	3.0	15	0.1733	0.0533	20.43
8	3.0	30	0.04675	0.0311	22.08
9	5.0	30	0.07653	0.012	21.66
10	9.0	50	0.0433	0.00898	18.9
11	9.0	70	0.02115	0.0044	18.08
12	13.0	70	0.0320	0.00266	18.9
13	13.0	100	0.0139	0.0019	16.8
14	17.0	150	0.0065	0.00084	13.6

Name of the place : Parmani

Sr.No	P1P2/2 (m)	C1C2/2 (m)	Resistance (ohm.m)	G	App.Resi (ohm.m)
1	0.5	1	7.403925	2.66	17.89
2	0.5	3	0.32035	0.22	9.29
3	0.5	5	0.11515	0.08	9.04
4	1.0	5	0.21063	0.16	8.3
5	1.0	7	0.1218	0.0816	9.3
6	1.0	10	0.06193	0.04	9.7
7	3.0	15	0.09255	0.0533	10.9
8	3.0	30	0.0225	0.0133	10.6
9	7.0	50	0.0195	0.0112	10.9
10	7.0	70	0.00876	0.0057	9.6
11	11.0	100	0.00606	0.0044	8.6
12	15.0	150	0.00363	0.00266	8.57
13	15.0	200	0.00206	0.0015	8.63
14	15.0	300	0.0011	0.00066	10.36

Name of the place : Diwankhera

Sr.No	PIP2/2 (m)	C1C2/2 (m)	Resistance (ohm.m)	G	App.Resi (ohm.m)
1	0.5	1	5.9755	2.66	14.4
2	0.5	3	0.3888	0.22	11.1
3	0.5	5	0.1023	0.08	8.03
4	1.0	5	0.220825	0.16	8.67
5	1.0	7	0.102525	0.0816	7.9
6	1.0	10	0.0469	0.04	7.4
7	3.0	15	0.0659	0.0533	7.78
8	3.0	30	0.017	0.0133	8
9	7.0	50	0.0145	0.0112	8.13
10	7.0	70	0.00775	0.0057	8.543
11	11.0	100	0.0046	0.0044	6.57
12	11.0	150	0.0018	0.00266	5.785
13	15.0	200	0.0016	0.0015	6.7
14	15.0	300	0.00095	0.00066	9.05

Name of the place : Isunyian

Sr.No	PIP2/2 (m)	C1C2/2 (m)	Resistance (ohm.m)	G	App.Resi (ohm.m)
1	0.5	1	38.43	2.66	92.7
2	0.5	3	3.582	0.22	102.3
3	0.5	5	0.9012	0.08	71
4	1.0	5	1.9664	0.16	77.22
5	1.0	7	0.8106	0.0816	62.42
6	1.0	10	0.30795	0.04	48.4
7	3.0	15	0.3803	0.0533	44.8
8	7.0	30	0.1785	0.0311	36.1
9	7.0	50	0.0607	0.0112	34.1
10	11.0	70	0.3657	0.00898	256
11	11.0	100	0.3105	0.0044	443.4
12	15.0	150	0.11896	0.00266	281
13	15.0	200	0.06596	0.0015	276.3
14	15.0	300	0.0334	0.00066	318

Name of the place : Utaria

Sr.No	PIP2/2 (m)	C1C2/2 (m)	Resistance (ohm.m)	G	App.Resi (ohm.m)
1	0.5	1	11.8826	2.66	28.7
2	0.5	3	0.45183	0.22	12.9
3	0.5	5	0.12445	0.08	9.77
4	1.0	5	0.2370	0.16	9.3
5	1.0	7	0.09515	0.0816	7.3
6	1.0	10	0.0440	0.04	6.9
7	3.0	15	0.0696	0.0533	8.2
8	3.0	30	0.01606	0.0133	7.58
9	7.0	50	0.01155	0.0112	6.4
10	7.0	70	0.0045	0.0057	4.9
11	11.0	100	0.0027	0.0044	3.86
12	15.0	150	0.001	0.00266	2.36
13	19.0	200	0.00193	0.0019	6.4
14	23.0	300	0.00074	0.00102	4.56

Name of the place : Mahipatkhera

Sr.No	PIP2/2 (m)	C1C2/2 (m)	Resistance (ohm.m)	G	App.Resi (ohm.m)
1	0.5	1	6.9071	2.66	16.7
2	0.5	3	0.02845	0.22	0.8
3	0.5	5	0.014225	0.08	1.117
4	1.0	5	0.013275	0.16	2.08
5	1.0	7	0.02524	0.0816	1.9
6	1.0	10	0.1	0.04	15.7
7	3.0	15	0.2701	0.0533	31.84
8	3.0	30	0.1082	0.0133	51.116
9	7.0	50	0.06285	0.0112	35.26
10	11.0	70	0.04015	0.0057	28
11	11.0	100	0.0179	0.0044	25.56
12	15.0	150	0.006416	0.00266	15.15
13	15.0	200	0.06308	0.0015	264.23
14	15.0	300	0.0013	0.00066	12.4

Name of the place : Powa

Sr.No	P1P2/2 (m)	C1C2/2 (m)	Resistance (ohm.m)	G	App.Resi (ohm.m)
1	0.5	1	21.02	2.66	50.8
2	0.5	3	0.8716	0.22	24.9
3	0.5	5	0.3755	0.08	29.5
4	1.0	5	0.7085	0.16	27.8
5	1.0	7	0.4123	0.0816	31.75
6	3.0	10	0.667	0.12	35
7	3.0	15	0.25	0.0533	29.5
8	7.0	30	0.1716	0.0311	34.7
9	7.0	50	0.0518	0.0112	29
10	11.0	70	0.042	0.00898	29.4
11	11.0	100	0.018	0.0044	25.7
12	15.0	150	0.0109	0.00266	25.75
13	15.0	200	0.0057	0.0015	18.6
14	19.0	290	0.0025	0.0009	17.4

Name of the place : Pyarepur

Sr.No	P1P2/2 (m)	C1C2/2 (m)	Resistance (ohm.m)	G	App.Resi (ohm.m)
1	0.5	1	14.174	2.66	34.3
2	0.5	3	1.0662	0.22	30.45
3	0.5	5	0.2688	0.08	21.1
4	1.0	5	0.53125	0.16	20.85
5	1.0	7	0.281	0.0816	21.6
6	3.0	10	0.23	0.12	12
7	3.0	15	0.11075	0.0533	13
8	3.0	30	0.0394	0.0133	18.6
9	11.0	70	0.09463	0.00898	50
10	11.0	100	0.0247	0.0044	35.3
11	15.0	150	0.01553	0.00266	36.7
12	19.0	200	0.0059	0.0019	19.5
13	19.0	300	0.0025	0.00084	18.6

Name of the place : Bhadeona

Sr.No	P1P2/2 (m)	C1C2/2 (m)	Resistance (ohm.m)	G	App.Resi (ohm.m)
1	0.5	1	76.584	2.66	185
2	0.5	3	5.76515	0.22	164.6
3	0.5	5	2.06925	0.08	162.43
4	1.0	5	3.8665	0.16	151.76
5	1.0	7	1.53883	0.0816	118.5
6	1.0	10	0.859	0.04	135
7	3.0	15	0.4195	0.0533	49.4
8	3.0	30	0.13263	0.0133	62.64
9	7.0	50	0.0495	0.0112	27.77
10	11.0	70	0.0238	0.00898	16.65
11	11.0	100	0.00365	0.0044	5.7
12	15.0	150	0.001	0.00266	2.4
13	19.0	200	0.00295	0.0019	9.75
14	19.0	300	0.00435	0.00084	32.5

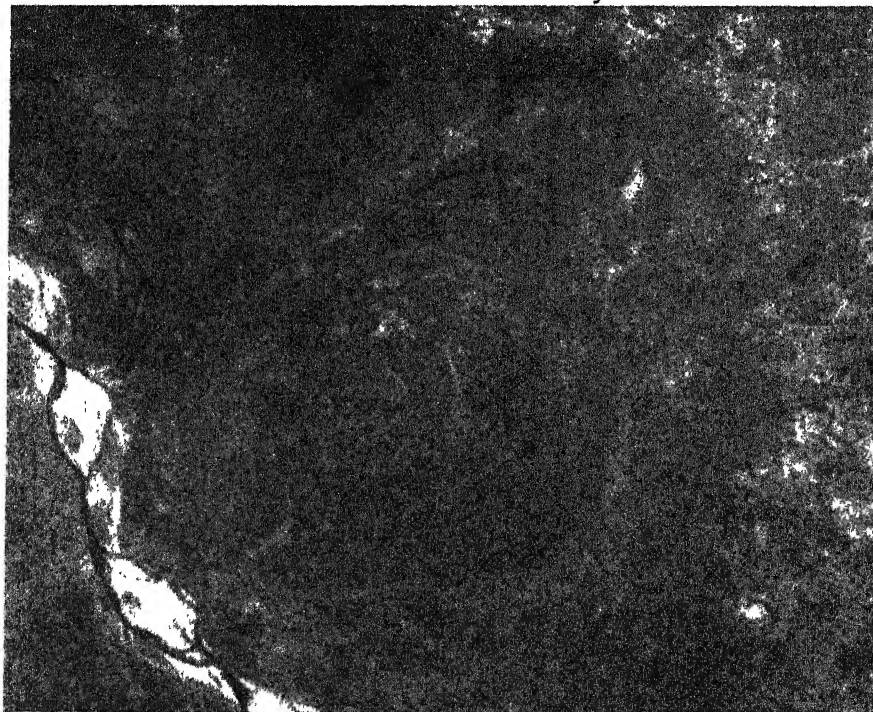
Name of the place : Mubarkpur

Sr.No	P1P2/2 (m)	C1C2/2 (m)	Resistance (ohm.m)	G	App.Resi (ohm.m)
1	0.5	1	44.73	2.66	108
2	0.5	3	1.9635	0.22	56
3	0.5	5	0.7936	0.08	62.3
4	1.0	5	1.7356	0.16	68.122
5	1.0	7	0.82975	0.0816	63.9
6	1.0	10	0.3628	0.04	57
7	1.0	15	0.127	0.0177	45
8	3.0	30	0.08485	0.0133	40
9	7.0	50	0.0249	0.0048	32.6
10	7.0	70	0.2745	0.0057	302
11	7.0	100	0.02675	0.0028	60
12	11.0	150	0.00715	0.001955	23
13	15.0	200	0.006	0.0015	25
14	19.0	300	0.00165	0.00084	12.3

APPENDIX III- Original data used in this present study
Pan, Band 1, Band 2, Band 3



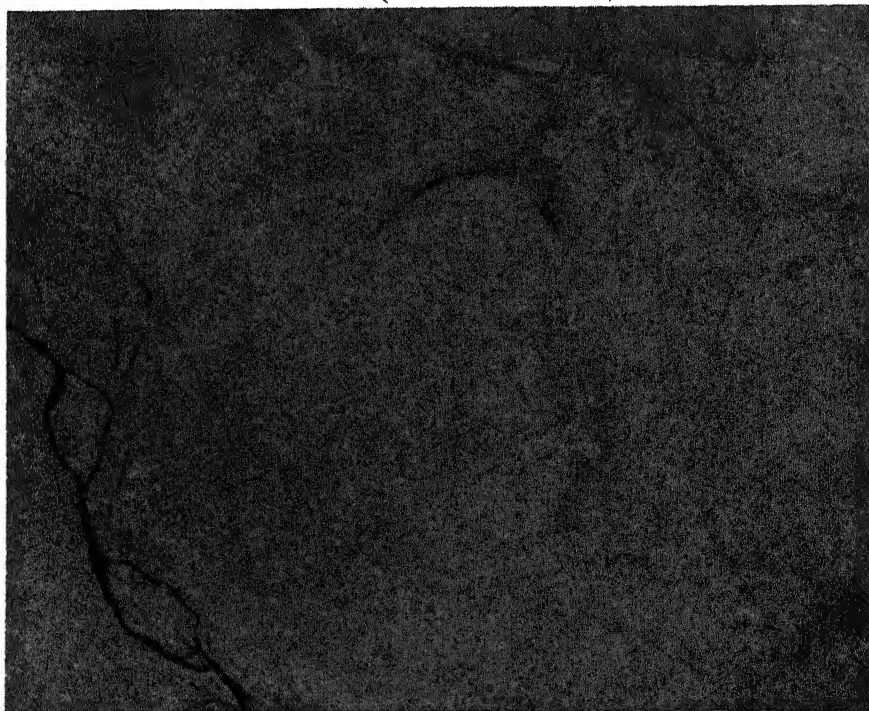
IRS-1C Panchromatic Band for study area



Band 1 (IRS-1C LISS III)



Band 2 (IRS-1C LISS III)



Band 3 (IRS-1C LISS III)